

Department of Physics and Astronomy

University of Heidelberg

Master thesis

in Physics

submitted by

Lukas Layer

born in Schwäbisch Hall

2017

**Beauty production in Pb–Pb
with the ALICE experiment
at $\sqrt{s_{NN}} = 5.02$ TeV**

This Master thesis has been carried out by Lukas Layer

at the

University of Heidelberg

under the supervision of

Frau Prof. Silvia Masciocchi

Abstract

The measurement of open heavy-flavour hadrons plays a key role in the physics program of the ALICE experiment. Heavy quarks are a unique probe of the properties of the quark-gluon plasma, a state of hot deconfined matter that is created in the collisions of ultra-relativistic heavy-ions. From a theoretical point of view, the large masses of the heavy quarks make the computation of the transport coefficients, that characterize transport properties of the medium, feasible directly from first principle QCD calculations. Measurements of the nuclear modification factor R_{AA} of heavy-flavour hadrons are an important observable to constrain phenomenological models that make a bridge between experiment and first principle QCD calculations. In this work the nuclear modification factor of non-prompt J/ψ coming from beauty hadron decays with low transverse momenta in Pb–Pb collisions at a collision energy of $\sqrt{s_{NN}} = 5.02$ TeV is presented. The measurement is based on a decomposition of the measured inclusive J/ψ yield in the dielectron channel in Pb–Pb at $\sqrt{s_{NN}} = 5.02$ TeV into its prompt and non-prompt components. This is achieved via a 2-dimensional log-likelihood fit to the invariant mass spectra and the pseudo-proper decay length distribution. In addition multivariate methods are tested and applied to increase the sensitivity of the measurement. Moreover, the feasibility of a measurement of beauty hadrons via displaced multitrack vertices in Pb–Pb collisions was investigated.

Zusammenfassung

Die Messung von Hadronen die schwere Quarks enthalten hat eine herausragende Bedeutung im physikalischen Programm von ALICE. Schwere Quarks sind eine einzigartige Probe der Eigenschaften des Quark-Gluon Plasmas, einem Zustand heißer Materie in dem sich Quarks und Gluonen in einem Zustand des "Deconfinement" befinden, der in ultra-relativistischen Schwer-Ionen Kollisionen erzeugt werden kann. Die hohe Masse der schweren Quarks erlaubt es die Transportkoeffizienten des QGP, die den Transport im heißen Medium charakterisieren, ausgehend von fundamentalen QCD Prinzipien zu berechnen. Messungen des nuklearen Modifikationsfaktor R_{AA} von schwere Quarks enthaltende Hadronen, stellen eine wichtige Observable dar um phenomenologische Modelle zu testen, die die Verbindung zwischen Experiment und fundamentalen QCD Prinzipien herstellen. In dieser Arbeit wurde der nukleare Modifikationsfaktor von J/ψ gemessen, die von Beauty Zerfällen mit niedrigen Impulsen stammen. Die Messung wurde bei einer Kollisionsenergie von $\sqrt{s_{NN}} = 5.02$ TeV in Pb-Pb durchgeführt. Die Messung nutzt einen 2-dimensionalen log-likelihood fit zum inklusiven J/ψ Spektrum der invarianten Masse und der Pseudo-Eigenzerfallslänge um die J/ψ Komponente zu erhalten, deren Ursprung Beauty Zerfälle sind. Multivariate Analysis Methoden wurden getestet und angewandt um die Sensitivität der Messung zu erhöhen. Darüber hinaus wurde eine Machbarkeitsstudie zur Messung von Hadronen, die Beauty Quarks enthalten, durch die topologische Rekonstruktion von Vertices durchgeführt.

Contents

1. Heavy-ion collisions and the quark-gluon plasma	11
1.1. Quantum chromodynamics	11
1.1.1. Introduction	11
1.1.2. The QCD phase diagram	12
1.1.3. Lattice QCD	13
1.2. Heavy-ion collisions	16
1.2.1. Space-time evolution	16
1.2.2. Collision geometry and Glauber model	17
1.2.3. Flow	18
1.2.4. Hadronization	20
2. Heavy quarks in nucleus-nucleus collisions	21
2.1. Theoretical description of heavy-flavour in medium	22
2.1.1. Energy loss	22
2.1.2. Initial heavy-flavour spectra	23
2.1.3. Hadronization	25
2.1.4. Bulk medium evolution	26
2.1.5. Models	26
2.2. Open heavy-flavour production measurements	28
2.2.1. Measurement techniques	28
2.2.2. Nuclear modification factor measurements at the LHC	29
2.2.3. Azimuthal anisotropy measurements at the LHC	32
2.2.4. Conclusions and motivation of the thesis	33
3. ALICE	35
3.1. The Detector	35
3.2. The V0 detectors	36
3.3. The Inner Tracking System	36
3.4. The Time Projection Chamber	37
4. Non-prompt J/ψ production	39
4.1. Selection criteria and inclusive J/ψ production	39
4.1.1. Data sample and event selection	39
4.1.2. Track selection	40
4.1.3. J/ψ raw yield extraction	41
4.1.4. Inclusive R_{AA}	43
4.2. Study of MVA methods	45
4.2.1. Introduction to TMVA and Boosted Decision Trees	45
4.2.2. Choice of the input variables	48
4.2.3. Performance of the BDT	49
4.2.4. Systematic uncertainties	53
4.2.5. Conclusions and outlook	54
4.3. Extraction of the non-prompt J/ψ fraction	56
4.3.1. Analysis method	56
4.3.2. Templates for the fit	59
4.3.3. Fit results	63

4.3.4.	Acceptance and efficiency corrections	67
4.3.5.	Systematic uncertainties	69
4.3.6.	f_B reference fraction in pp at $\sqrt{s} = 5.02$ TeV	72
4.3.7.	Results for the R_{AA} of non-prompt J/ψ	74
5.	Topological vertexing approach at low transverse momentum in Pb–Pb	77
5.1.	Basic idea	77
5.2.	Data sample and algorithm	77
5.3.	Results and conclusions	78
6.	Conclusions and outlook	81
A.	Additional figures for the TMVA studies	83
B.	Additional figures for the simultaneous log-likelihood fit	86

1. Heavy-ion collisions and the quark-gluon plasma

1.1. Quantum chromodynamics

1.1.1. Introduction

The gauge field theory of the strong interaction is called quantum chromodynamics (QCD). It describes the interaction of quarks and gluons. It is a non-abelian gauge theory with a Lagrangian that is invariant under local SU(3) symmetry transformations that can be written as [1]:

$$\mathcal{L} = F_{\mu\nu}^a F^{a\mu\nu} + \sum_{j=1}^f \bar{q}_j (i\gamma^\mu D_\mu - m_j) q_j \quad (1)$$

where j goes over the f flavors. D_μ denotes the covariant derivative: $D_\mu = \partial_\mu + ig_s A_\mu$. The quark field q_j is in the fundamental representation of SU(3). The gauge fields $A_\mu = A_\mu^a T^a$, where T^a ($a = 1, \dots, 8$) are traceless hermitean 3 by 3 matrices, the generators of SU(3), and correspond to the gluon fields. Gluons are the gauge bosons of the strong interaction. The single charge known from (quantum) electrodynamics is replaced by three conserved colour charges, r, b and g (where colour is simply a label for the orthogonal states in the SU(3) colour space). Only particles that have non-zero colour charge couple to gluons. To conserve colour in QCD interactions, the gluons itself must carry colour charge. The field tensor can be written as

$$F_{\mu\nu}^a = \partial_\mu A_\nu^a - \partial_\nu A_\mu^a + g_s f_{abc} A_\mu^b A_\nu^c \quad (2)$$

where f_{abc} are the so-called structure constants of the group SU(3). Since the gen-

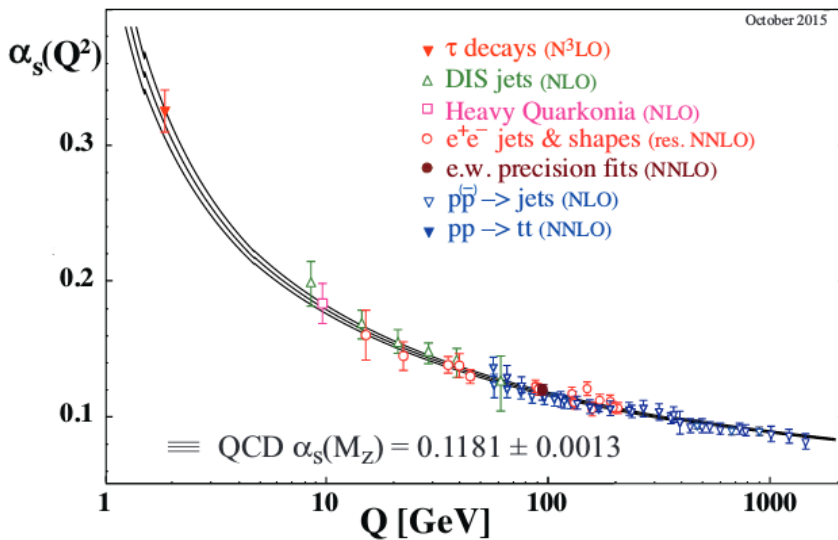


Figure 1: Running coupling of QCD [2].

erators of SU(3) do not commute, the last term gives rise to gluon self-interactions. There is experimental evidence for the existence of quarks [3]. However, so far free quarks, which would be observed as fractionally charged particles, have never been

seen directly. The non-observation of free quarks is explained by the hypothesis of colour confinement, which states that coloured objects are always confined to colour singlet states. Solving the renormalization group equation of QCD leads at 1-loop to the result [4]:

$$\alpha_s(\mu) = \frac{g_s^2}{4\pi} = \frac{2\pi}{11 - \frac{2}{3}N_f} \frac{1}{\ln \frac{\mu}{\Lambda_{QCD}}} \quad (3)$$

with the energy scale μ . N_f is the number of quark flavors and Λ_{QCD} the location of the QCD Landau pole. A comparison to measurements is shown in Fig. 1. The running coupling decreases with increasing Q^2 [5, 6]. The small coupling at large momentum transfer, or equivalently, small distances, is referred to as asymptotic freedom. At the low momentum scale, characteristic of the quarks bound inside hadrons, the coupling becomes very strong and perturbative calculations are not adequate any more. In this case, lattice-QCD calculations are needed, which is a non perturbative treatment of QCD, formulated on a discrete space-time lattice [7]. Considering the Lagrangian defined in equation 1 for two flavour u and d , denoted as $q = \begin{pmatrix} u \\ d \end{pmatrix}$, in the limit of vanishing quark masses, the Lagrangian is invariant under a SU(2) symmetry transformation, called chiral SU(2) symmetry because the right handed quarks q_R and the left handed quarks q_L are decoupled and transform differently. Given that m_u and m_d are both much smaller than the energy scale of the strong interaction Λ_{QCD} , the chiral SU(2) symmetry is an approximate symmetry. However, experimentally it was found that the mass of bound states of hadrons is not only determined by valence quarks, but also by virtual seaquarks and gluons [8]. This results in a constituent quark mass $M_{u,d} \sim 300$ MeV of up and down quarks which is significantly higher than the bare mass m_q associated with the Higgs mechanism. The constituent quark mass $M_{u,d}$ implies a breaking of the chiral symmetry.

1.1.2. The QCD phase diagram

The asymptotic freedom of quarks and gluons at high temperatures or high pressure results in a new state of strongly interacting matter. This can be understood from simple considerations [9]: it is known that hadrons have an intrinsic size of ~ 1 fm and therefore need a certain volume to exist. This suggests that by increasing the pressure on nucleons they will overlap and the definition of a hadron will lose its meaning, since the original quark cannot identify the quarks with which it originally formed the hadron. Therefore, beyond a certain point nuclear matter reaches a new phase, where the basic constituents are unbound quarks. According to Hagedorn [10] there exists a limiting temperature for hadronic systems in the range of 140 – 180 MeV. The new state of deconfined matter is called the quark-gluon plasma (QGP) [11]. The chiral symmetry of the QCD Lagrangian is predicted to be restored again in the QGP, because an increase of the temperature results in a melting of the gluon cloud surrounding the quark. It can be shown that deconfinement and chiral symmetry restoration either appear at the same critical point, or if this is not the case deconfinement precedes chiral symmetry restoration. [9]

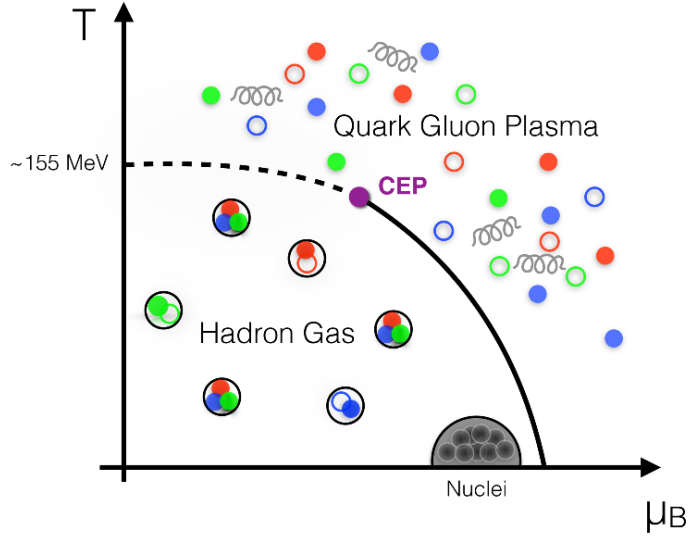


Figure 2: Sketch of the phase diagram of QCD [12].

The QCD phase diagram is shown in figure 2. The critical temperature depends on the net baryon density. At low temperatures for $\mu_B \sim 1$ GeV, corresponding to nuclear density, there is the ordinary hadronic matter. For sufficiently high values of the baryo-chemical potential, the system exhibits a first order transition between hadronic matter and the QGP. Lattice QCD calculations at non-zero chemical potential suggest the existence of a critical point, such that the transition is no longer first-order. Recent calculations, suggest that the transition at low values of the baryo-chemical potential is not a phase transition, but rather a rapid crossover that occurs in a small, well defined, temperature interval. With energies of the heavy-ion collisions at the LHC, the region with zero baryo-chemical potential is probed. In the future there will be another experiment, FAIR, probing the QGP at higher baryo-chemical potential. The region of zero baryo-chemical potential is of special interest, since it is believed that after the electroweak phase transition of the big bang a phase of Quark-Gluon Plasma followed. Understanding the phase structure of QCD as part of the standard model based on the many-body physics of quarks and gluons is one of the the outstanding challenges in modern nuclear research.

1.1.3. Lattice QCD

The thermodynamics to the dynamics defined by the Lagrangian in equation 1 is obtained from the partition function, expressed as a functional path integral [8]:

$$Z(T, V) = \int dA dq d\bar{q} \exp \left(\int_V d^3x \int_0^{1/T} d\tau \mathcal{L} \right) \quad (4)$$

The spatial integration in the exponent is performed over the entire spatial volume V of the system, which in the thermodynamic limit becomes infinite. The time component x_0 is imaginary, $\tau = ix_0$, thus turning the Minkowski space into an Euclidean space. From $Z(T, V)$, all thermodynamical observables can be calculated,

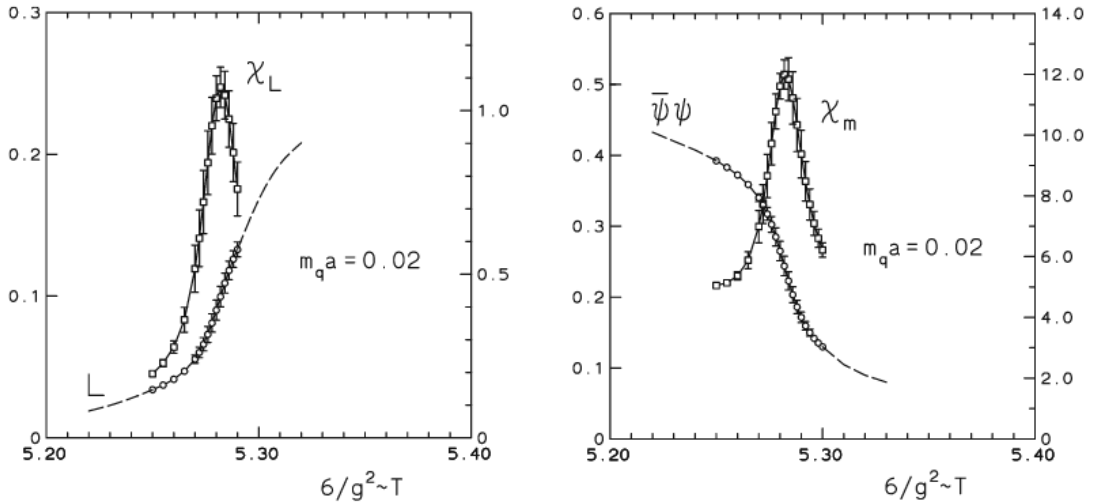


Figure 3: Polyakov loop and chiral condensate in a two-flavour QCD [13].

e.g.

$$\epsilon = (T^2/V) \left(\frac{\partial \ln Z}{\partial T} \right)_V \quad (5)$$

gives the energy density, and

$$P = T \left(\frac{\partial \ln Z}{\partial V} \right)_T \quad (6)$$

gives the pressure.

The lattice formulation of QCD provides a non-perturbative regularization scheme, leading to a form which can be evaluated numerically by computer simulations.

The deconfinement measure in lattice QCD is given by the Polyakov loop [8]:

$$L(T) \propto \lim_{r \rightarrow \infty} \exp(-V(r)/T) \quad (7)$$

where $V(r)$ is the potential between a static quark-antiquark pair.

In a pure gauge theory, without light quarks, $V(r)$ is proportional to σr , where σ is the string tension. Therefore L vanishes for infinite separation of the quarks. However, in a deconfined medium, colour screening among the gluons leads to a melting of the string. Therefore $V(r)$ becomes finite at large distances and L does not vanish any more. It thus is considered as an order parameter. If the temperature is smaller than the critical temperature T_c , the deconfinement measure L vanishes, hence the system is confined, while for a temperature larger than T_c , the measure L is finite, hence the system is deconfined. Thus deconfinement sets in at the critical temperature T_c at which L becomes finite.

The effective quark mass is measured by the expectation value of the corresponding term in the Lagrangian, $\langle q\bar{q} \rangle$. In the limit of vanishing current quark mass, the Lagrangian becomes chirally symmetric and $\langle q\bar{q} \rangle$ the corresponding order parameter.

Calculations of the chiral susceptibility at different temperatures suggest a rapid crossover from hadronic matter to matter where chiral symmetry and deconfinement is restored as shown in Fig. 3. The transition temperature for the chiral

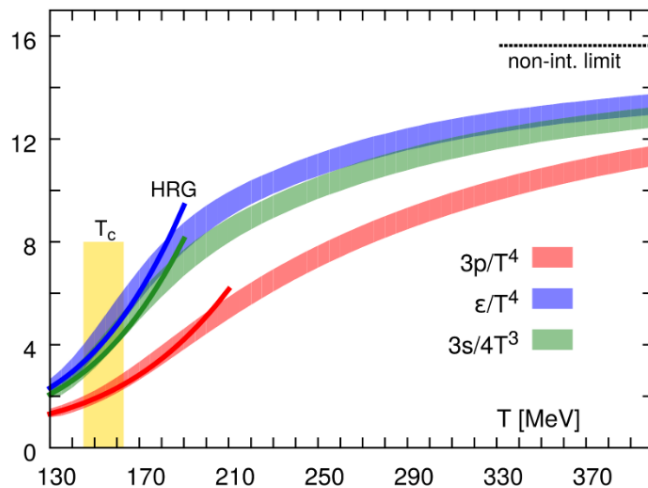


Figure 4: Lattice calculations for pressure, energy density and entropy density [16].

symmetry restoration was estimated as $T_c = 154 \pm 9$ MeV [14, 15]. Fig. 4 shows the results for pressure, energy density and entropy density obtained from lattice QCD calculations [16]. For the energy density ϵ it is seen that ϵ/T^4 changes suddenly at the critical temperature T_c . It increases from a low value to the one slightly below the one expected for an ideal gas of massless quarks and gluons. The results of lattice QCD can be used as input for the hydrodynamic calculations needed to describe heavy-ion collisions.

1.2. Heavy-ion collisions

To probe and characterize the QGP, it is necessary to produce it in the laboratory. Since collisions of single particles like protons or electrons produce too few particles to allow for a thermodynamical treatment, heavy ion collisions at high energies have to be used to create a fireball of interacting quarks and gluons above the temperature for the phase transition into deconfinement.

1.2.1. Space-time evolution

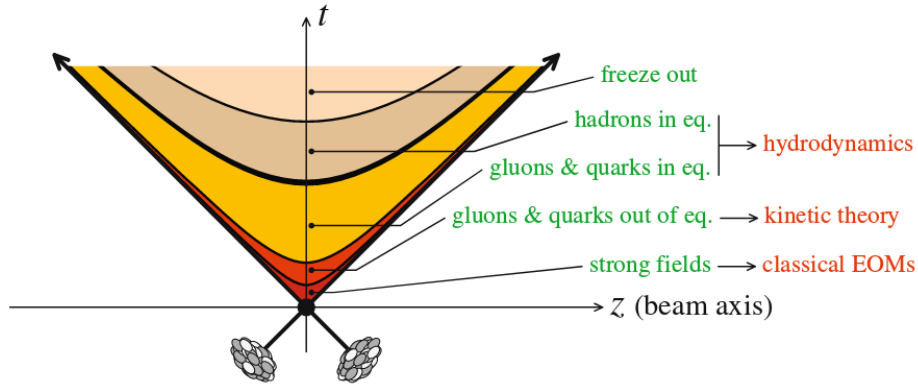


Figure 5: Space-time evolution of a heavy-ion collision [17].

A schematic space-time picture of the evolution of a heavy-ion collision is shown in Fig. 5. It illustrates the different stages of a heavy-ion collision. In the following a brief overview will be given [18, 19]:

1. Prior to the collision in the center-of-mass frame the two incoming nuclei are highly Lorentz-contracted. They are mostly composed of gluons which carry only small fractions $x \ll 1$ of the longitudinal momenta of their parent nucleons, but the density of the gluons is rapidly increasing with $1/x$. This gluonic form of matter, which is dense and weakly coupled, dominates the wave function of any hadron at sufficiently high energy and is called colour glass condensate.
2. At time $\tau = 0$, the two nuclei collide and the interactions start developing. Hard processes with large momentum transfer $Q \gtrsim 10$ GeV occur, producing particles that carry transverse energies and momenta of the order of Q , such as (hadronic) jets, direct photons, dilepton pairs, heavy quarks, or vector bosons.
3. At a time $\tau \sim 0.2$ fm/c the bulk of the partonic constituents of the colliding nuclei are liberated by the collision. They form a non-equilibrium state of partonic matter, which has a relatively high density and is known as the glasma.
4. The partonic matter rapidly approaches thermal equilibrium. The thermalization time is of the order $\tau \sim 1$ fm/c. Strong interactions among the

partons are required to compete with the medium expansion. The observed rapid thermalization indicates that the dense partonic matter produced in the intermediate stages of a heavy-ion collision may be a strongly coupled fluid.

5. The result of the thermalization process is the high-temperature phase of QCD, the quark-gluon plasma. The partonic matter keeps expanding and cooling down. Hadronization occurs when the temperature becomes of the order of the critical temperature T_c for deconfinement. In Pb–Pb collisions at the LHC, this is estimated to happen around a time $\tau \sim 10 fm/c$ [19].
6. For larger times $10 < \tau < 20 fm/c$, the hadronic system is still relatively dense, so it preserves local thermal equilibrium while expanding. This stage is referred to as a hot hadron gas, whose temperature and density is decreasing with time.
7. At a time $\tau \sim 20 fm/c$, the density becomes so low that the hadrons stop interacting with each other. This transition between a fluid state (where the hadrons undergo many collisions) and a system of free particles is referred to as the freeze-out.

1.2.2. Collision geometry and Glauber model

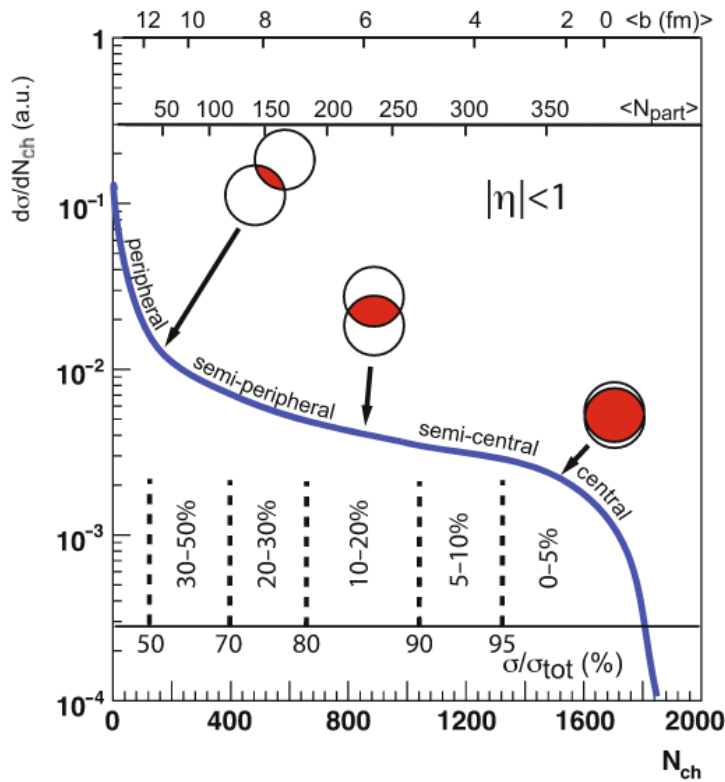


Figure 6: Scheme showing the centrality definition from the final-state particle multiplicity and its correlation with the impact parameter and the number of participating nucleons (N_{part}) [20].

a Fourier expansion yields:

$$E \frac{d^3 N}{d^3 p} = \frac{1}{2\pi} \frac{d^2 N}{p_T dp_T dy} \left[1 + \sum_{n=0}^{\infty} 2 v_n(p_T, y) \cos(n(\Phi - \Psi_n)) \right] \quad (9)$$

The azimuthal distribution of the particles is obtained relative to the symmetry plane angles Ψ_n . The pressure gradient between the hot center and the surface of the fireball gives rise to the first harmonic v_1 , the so-called directed or radial flow. The second harmonic v_2 is called elliptic flow, and originates from the asymmetry of the collisions. The two centers of the nuclei define the so-called reaction plane, shown in Fig. 7. The overlap region of the two nuclei has an almond like shape. This results in a pressure gradient that is larger along the direction of the event plane, that for v_2 is Ψ_2 . The effect is reflected in the azimuthal distribution of the particles. The initial spatial anisotropy is converted into a momentum anisotropy of the final state particles. Triangular flow v_3 results from fluctuations of the initial nucleon density profiles in the nuclei.

The harmonics can be obtained by averaging all particles with angle Φ_i in a given rapidity and transverse momentum interval in a fixed centrality class in all events [23]:

$$v_n(p_T, y) = \langle \cos[n(\Phi_i - \Psi_i)] \rangle \quad (10)$$

In Fig. 8 measurements of different harmonics as a function of centrality by ALICE [24, 25] are compared to the viscous hydrodynamic model MUSIC [26] for a shear viscosity to entropy density ratio of 0.095. The interaction strength of the medium reflects in the time scale of converting the pressure to a momentum distribution in the hydrodynamic evolution. This is connected to the equation of state and the shear viscosity to entropy density ratio η/s . The data is in good agreement with the model calculations, which indicates that the medium thermalizes rapidly and the small value of η/s indicates that the QGP evolves almost as a perfect fluid.

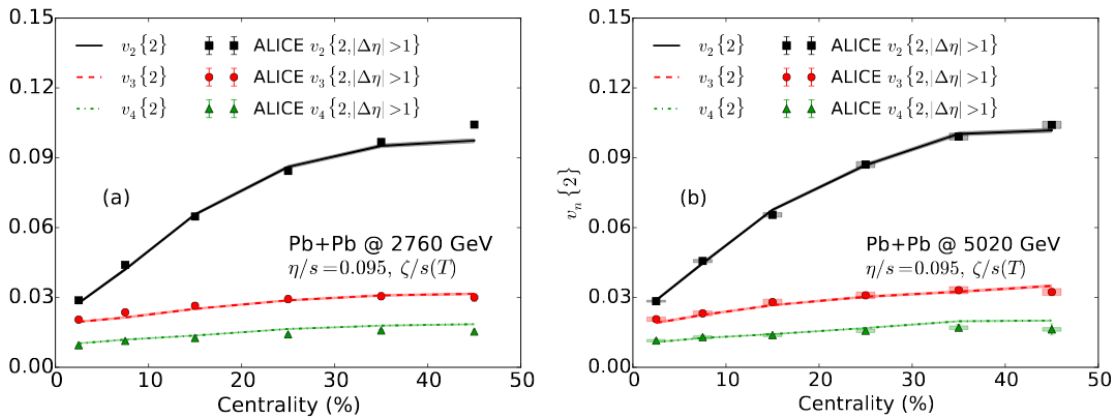


Figure 8: The centrality dependence of charged hadron anisotropic flow coefficients in Pb–Pb collisions at 2.76 TeV (a) and 5.02 TeV (b). Theoretical results are compared with the recent ALICE measurements at both collision energies [24, 25] [26].

1.2.4. Hadronization

As discussed above, the transition between a fluid state and a system of free particles is called freezeout. This freeze-out process is defined by two relevant scales: the chemical freeze-out after which the particle composition of the matter does not change and the kinetic freeze-out, after which the particles do not interact any more.

The measurement of identified hadron yields can be used to estimate the chemical freeze-out temperature, the baryon-chemical potential and the volume of the deconfined matter by comparing the measured abundances with the predictions of the statistical hadronization model [27]. This model assumes that the system is in the thermal and chemical equilibrium at the chemical freeze-out, based on a grand-canonical formalism.

For central Pb-Pb collisions at LHC energies this yields a temperature of 156 MeV with vanishing baryon chemical potential as shown in Fig. 9.

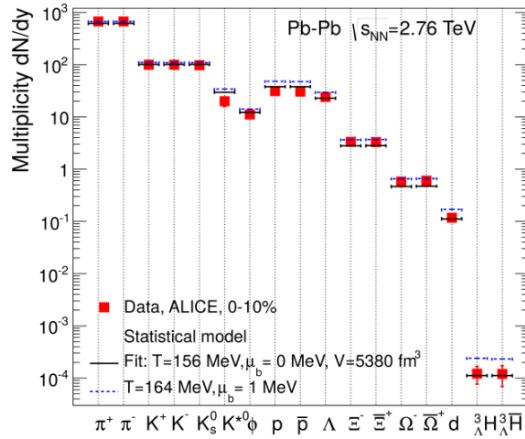


Figure 9: Comparison of the statistical hadronization model with measurements by ALICE [28].

2. Heavy quarks in nucleus-nucleus collisions

Charm and beauty hadrons are unique probes of the properties of the medium formed in heavy-ion collisions [29]. In contrast to light quarks and gluons, which can be produced or annihilated during the entire evolution of the medium, essentially all heavy quarks are produced in initial hard-scatterings. The time scale of their production is in general shorter than the formation time of the QGP ($\approx 0.1 - 1 \text{ fm}/c$). Since the production threshold is much higher than the typical medium temperatures, charm production from processes like $gg \rightarrow cc$ in the QGP is expected to be very small [29]. Therefore, heavy quarks preserve their flavour and mass identity while traversing the medium. In particular for beauty quarks the thermalization time is likely to be larger than the lifetime of the plasma, thus they can carry information starting from the earliest moments after the creation [30]. During their propagation through the medium, heavy quarks interact with the partons of the medium and lose a part of their energy, therefore they are sensitive to the medium properties. In a perturbative treatment, QCD energy loss is expected to occur via both inelastic (radiative energy loss) and elastic (collisional energy loss) processes. Heavy quarks can be investigated via the measurement of heavy-flavour hadrons. The interaction of heavy quarks with the QGP can be quantified by comparing the transverse momentum spectrum between nucleus-nucleus collisions and a scaled superposition of nucleon-nucleon collisions at similar energies, where the average number of binary collisions $\langle N_{coll} \rangle$ is used. The ratio is called the nuclear modification factor R_{AA} [29], defined as

$$R_{AA} = \frac{1}{\langle N_{coll} \rangle} \frac{dN_{AA}/dp_T}{dN_{pp}/dp_T} \quad (11)$$

The R_{AA} is expected to be equal to unity, if no nuclear or QGP-induced effects are present. At large transverse momenta, the R_{AA} is expected to be mostly sensitive to the average energy loss of heavy quarks in the hot medium. For sufficiently high momenta, heavy quarks will behave as light particles, for which the energy loss is dominated by gluon radiation. It currently remains an open question at which momenta this occurs and whether it coincides with a transition from non-perturbative to perturbatively calculable mechanisms [31]. Open questions for low momentum heavy quarks are whether they can reach thermal equilibrium with the medium constituents and participate in the collective expansion of the system and which role recombination effects have for the hadronization of the heavy quarks. This can be studied via the R_{AA} at low and intermediate transverse momentum and with measurements of the elliptic flow defined in the previous chapter. The goal of the measurement of heavy-flavour is the characterization of the properties of the QGP, in particular extracting the transport coefficients of the QGP [29]. Since they are sensitive to the coupling strength, they are considered as an important window on the non-perturbative many-body physics of the strongly coupled QGP. The way to access the transport coefficients is comparing theoretical models for different values of the transport coefficients with the experimental data to put constraints on the numerical values of the coefficients. From the theoretical side the outstanding challenge is to derive the heavy-flavour transport coefficients from first principle QCD calculations, include them in models that describe the medium evolution and confront them with data [29].

2.1. Theoretical description of heavy-flavour in medium

Models for the energy loss for heavy-flavours (HF) in heavy-ion collisions need to include several ingredients. These are: the initial production of heavy-flavour, a space-time description of the QGP evolution, mechanisms for hadronization and heavy-flavour interactions in the hadronic matter.

2.1.1. Energy loss

The motion of HF particles at temperatures of the QGP is similar to a Brownian motion, where a heavy probe is injected into a background medium of light particles.

The diffusion process of the probe particle is characterized by its coupling to the medium. It is schematically given by an average displacement squared [31]

$$\langle \vec{r}^2 \rangle = (2d)D_s t \quad (12)$$

where t denotes the time and $2d$ a conventional prefactor. The spatial diffusion coefficient D_s characterizes the transport properties of the medium. It can depend modestly on the quark mass but in the diffusion process is independent of the momentum [32]. It has been suggested that D_s can be scaled, such that it is proportional to the ratio of viscosity to entropy density of the medium

$$D_s(2\pi T) \propto \frac{\eta}{s}(4\pi) \quad (13)$$

This ratio is considered to be the smallest of any known substance. For ultra-relativistic heavy quarks, the dominant source of the energy loss is considered to be the radiation of gluons resulting from the scattering of the heavy quark on the constituents of the medium. For merely relativistic heavy quarks, collisional energy loss is believed to become important. In QCD quarks have a smaller colour coupling factor with respect to gluons. Thus the energy loss for quarks is expected to be smaller than for gluons. In addition, the suppression of forward-angle gluon emission with increasing mass of the incoming particle, called the dead-cone effect [33], is believed to further attenuate the effect of the medium. This leads to an expectation for the hierarchy of energy loss for partons: $\Delta E_g > \Delta E_{u,d,s} > \Delta E_c > \Delta E_b$.

There are two common approaches to implement the transport of HF in the medium, namely relativistic Langevin processes and Boltzmann simulations. The Boltzmann equation describes the evolution of the phase-space distribution of a heavy quark f_Q with a known collision integral $C[f_Q]$ and an external force F [31]:

$$\left[\frac{\partial}{\partial t} + \frac{\vec{p}}{E_p} \frac{\partial}{\partial \vec{x}} + \frac{\vec{F}}{E_p} \frac{\partial}{\partial \vec{p}} \right] f_Q(t, \vec{x}, \vec{p}) = C[f_Q] \quad (14)$$

where $E_p = \sqrt{m_Q^2 + \vec{p}^2}$ denotes the energy of the HF.

Since the momentum exchange per collision is small compared to the heavy quark momentum, this equation can be simplified, yielding the Fokker-Planck equation:

$$\frac{\partial}{\partial t} f_Q(t, \vec{p}) = \frac{\partial}{\partial p_i} \left(A_i(\vec{p}) f_Q(t, \vec{p}) + \frac{\partial}{\partial p_j} [B_{ij}(\vec{p}) f_Q(t, \vec{p})] \right) \quad (15)$$

The transport parameters A and B , characterize momentum friction and diffusion of the propagating heavy quark. Via a Langevin process, the Fokker-Planck equation can be implemented to simulate the HF motion in the medium. It consists of a drag and a diffusion part, defined by momentum and position updates as

$$dp_j = -\Gamma(p, T)p_j dt + \sqrt{dt}C_{jk}\rho_k \quad (16)$$

$$dx_j = \frac{p_j}{E} dt \quad (17)$$

The coefficients C_{jk} are related to the diffusion coefficients, while Γ is related to the friction coefficient. The diffusion coefficients encode the interactions with the medium. The friction coefficient represents the fractional momentum loss. For small momentum, the drift and diffusion coefficients are linked through the Einstein relation $B = m_Q \eta_D(p)T$ and are also uniquely related to the spatial diffusion coefficient D_s [29]. Various approaches to compute HF diffusion coefficients exist. Perturbatively inspired approaches include corrections to perturbative Born diagrams for HF scattering of light quarks from the medium, while non-perturbative approaches usually involve a ladder resummation of the interaction kernel. First principle non-perturbative results for the transport coefficients can be obtained from lattice QCD calculations [34]. However, the calculations only cover a limited kinematic domain and have still large systematic uncertainties. Due to the high masses of the HF, effective-theory calculations can be used to build a bridge between models to results from lattice QCD, thus relating phenomenology and QCD theory.

2.1.2. Initial heavy-flavour spectra

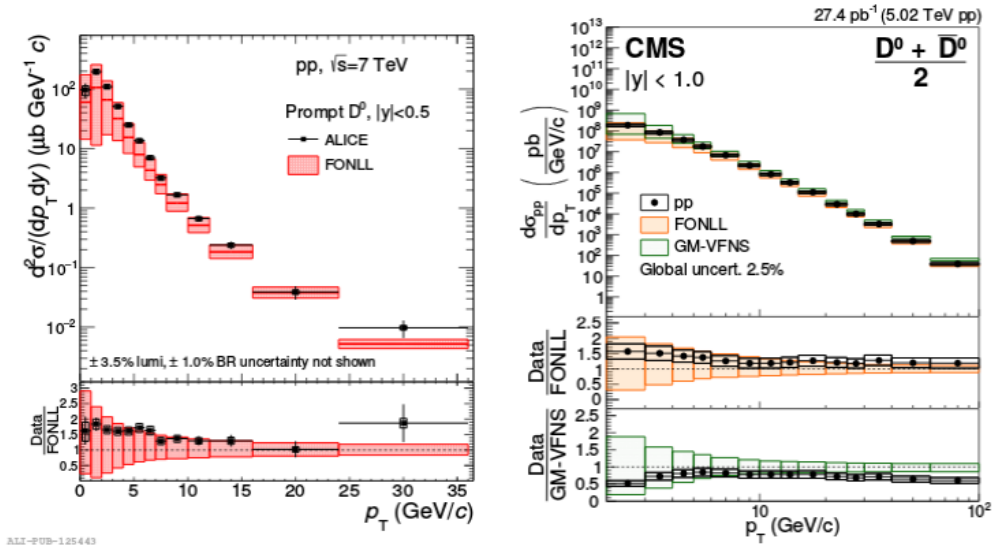


Figure 10: Comparison of the prediction of FONLL [33] with results from ALICE [35] and CMS [36] for the D^0 cross section in pp collisions.

Models of the interaction of heavy quarks with the medium need accurate p_T -distributions as input for the transport and energy loss, since different shapes of

the initial p_T distribution can lead to different values of R_{AA} and v_2 for the same model.

Often used to obtain the initial heavy-quark p_T -differential cross sections are Fixed-Order Next-to-Leading-Log (FONLL) calculations [33, 37]. This is a perturbative QCD (pQCD) calculation in which the HF production cross section is obtained through an expansion in powers of the coupling constant α_s . In particular, in FONLL the cross section is calculated to next-to-leading order (NLO) in α_s and some of the appearing logarithmic terms are resummed. The HF hadron cross section is factorized as a convolution of the parton distribution functions (PDFs) of the incoming partons, of the partonic cross sections and of a nonperturbative fragmentation function that gives the probability for a heavy quark with momentum p to fragment into a HF hadron with momentum $z \cdot p$, with $0 < z < 1$. The uncertainties of the cross section are estimated varying the mass, the perturbative scale-factors used by the calculation and the input PDFs. The FONLL calculation provides a good description of the production cross sections of D and B-mesons in pp collisions. It is observed that the central values of the FONLL calculation for D-meson spectra lie below the experimental values and the uncertainties of the theoretical calculation are larger than the experimental ones.

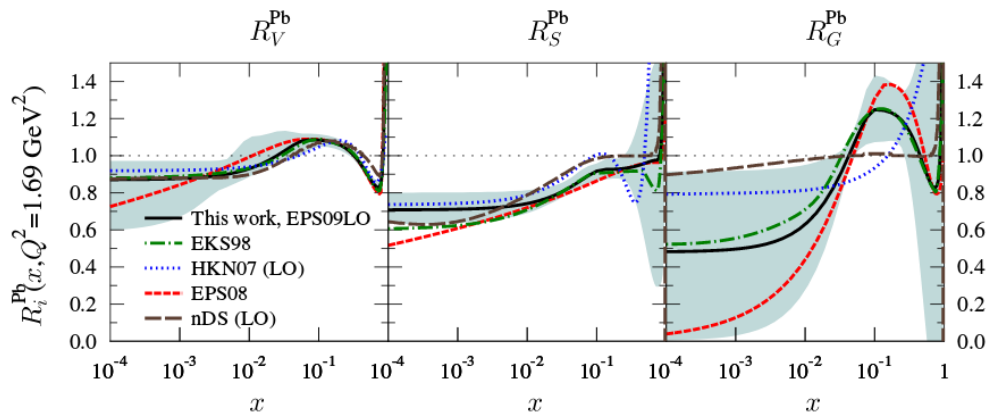


Figure 11: Ratio of PDFs for nucleons in Pb and protons from different calculations. Shown are the modifications for valence quarks (left), sea quarks (center) and gluons (right). The figure is taken from [38].

Cold-nuclear-matter (CNM) effects modify the yields and kinematic distributions of hadrons produced in hard scattering processes in pA and AA collisions and can be investigated in pA collisions [29]. The effect most relevant for HF production is the nuclear shadowing. It modifies the parton distribution functions, with the result that the PDFs of nucleons within nuclei differ from the PDFs of free protons. The effect is due to the different dynamics of partons within free protons with respect to those in nucleons and is mainly a consequence of the larger resulting density of partons. It depends on the Bjorken x and on the scale of the parton-parton interaction Q^2 . In pQCD calculations the nuclear effects are described in terms of nuclear-modified PDFs (nPDF). In general, three regimes can be identified for the nPDF to PDF ratio of a parton flavour i , $R_i(x, Q^2)$. At small x , a depletion is seen ($R_i < 1$) which is called shadowing. At intermediate values of x there is

an enhancement $R_i > 1$, called anti-shadowing. In addition a depletion occurs at large x , called the EMC effect. The $R_i(x, Q^2)$ parametrizations can be obtained by fitting lepton-nucleus and proton-nucleus data. A widely used nuclear PDF parametrization is the EPS09 set [38]. An example for the modifications to the PDFs of protons is shown in Fig. 11.

2.1.3. Hadronization

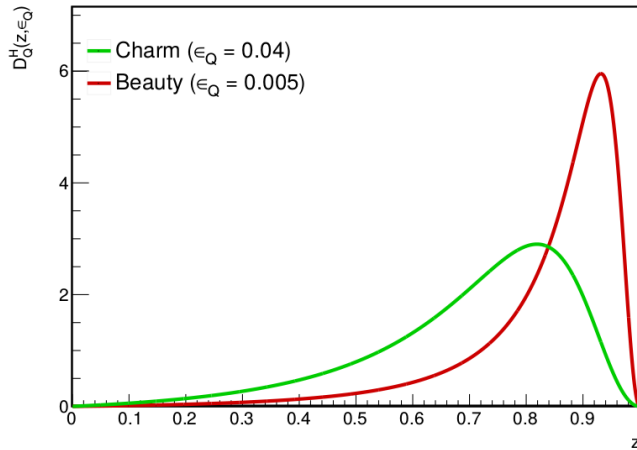


Figure 12: Petersen fragmentation functions for typical choices of $\epsilon_Q \propto 1/m_Q^2$. Figure taken from [31].

The diffusion of heavy flavour in the QGP needs to be interfaced by a transition of the degrees of freedom, from heavy quarks to HF hadrons [31]. In the vacuum empirical fragmentation functions are used to hadronize the quarks. They describe the probability distribution of producing a hadron of momentum p_h from a parent quark of momentum p_q , with the momentum fraction $z = p_h/p_q$. Different quark species and gluons are modeled with different distributions and are assumed to be universal for all collision systems. For HF fragmentation the Peterson fragmentation function [39] is often used, where an example is shown in Fig. 12. At low momentum this approach is not longer valid, since other effects, such as flow become important. A recombination of heavy quarks with surrounding light quarks has been suggested as an important effect in this regime. Several descriptions are used for this effect, giving different predictions, also for the relative yield of different charm and beauty hadron species [31]. Recombination processes for HF allow for the possibility of forming higher excited hadrons, in particular D^* mesons, Λ_c baryons and D_s mesons in the charm sector. They can have a significant impact on the D-meson abundance, since they deplete the charm quarks available for D-meson recombination. It has been suggested [40] that measurements of D_s can serve as a probe of coalescence effects. The suppression of strangeness in pp collisions is lifted in heavy-ion collisions compared to pp collisions. Consequently, it is expected to see an increase in the D_s/D ratio in Pb–Pb relative to pp collisions if recombination is a relevant mechanism.

2.1.4. Bulk medium evolution

The evolution of the bulk medium provides the link between the interactions of HF particles with the medium and the time evolution of their spectra. The Fokker-Planck/Langevin framework can be implemented into hydrodynamic models [31]. Ideal hydrodynamics is based on a set of conservation equations for the energy-momentum tensor and the baryon number and an equation of state. In viscous hydrodynamics, additional dissipative terms appear. It is possible to use lattice QCD calculations as input for the equation of state. A minimal requirement for evolution models for HF transport simulations is the description of light- hadron (π , K, p) multiplicities, p_T spectra and their elliptic-flow coefficient, v_2 , up to a typical transverse momentum of $p_T = 2$ GeV, in order to contain at least 90% of the produced bulk particles [31].

2.1.5. Models

In the following, three models that show an overall good agreement with the data and will be used at a later stage in the thesis are briefly introduced.

The pQCD energy loss model in a static fireball by **Djordjevic et al.** [41] takes into account both collisional energy loss and also radiative energy loss. It is applicable for both light and heavy partons and computes both radiative and collisional energy loss in the same theoretical framework. Within this model, radiative and collisional energy losses are calculated for an optically thin dilute QCD medium up to leading order [29].

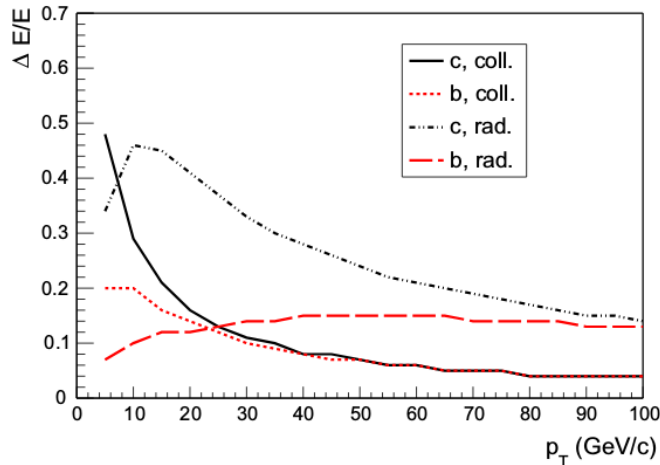


Figure 13: Fractional energy loss for collisional and radiative processes and for charm and beauty quarks. [41]

In Fig. 13, an example for the model calculation for the fractional energy loss is shown. For charm quarks, the radiative energy loss starts to dominate for $p_T > 10$ GeV/c, while this transition happens for $p_T > 25$ GeV/c for beauty quarks. The comparison of radiative energy loss for the charm and beauty calculation illustrates the dead cone effect, as well as its disappearance when the transverse momentum becomes much larger than the mass. However, no fluid dynamical

evolution is performed, thus the model cannot describe the v_2 and the R_{AA} for low momenta. For the heavy quark production FONLL is used, without the inclusion of shadowing. This model does not include hadronization via recombination. The R_{AA} predictions are provided for both RHIC and LHC energies, various light and heavy-flavour probes and different collision centralities.

In the pQCD-inspired running α_s energy-loss model **BAMPS** [42] (Boltzmann Approach to MultiParton Scatterings) the Boltzmann equation is used to both model the medium expansion via a 3+1 dimensional Monte-Carlo cascade evolution simulation and the propagation of the heavy quarks in the medium. The collisional energy loss is calculated from the pQCD Born approximation supplemented by a running coupling constant $\alpha_s(Q^2)$. Radiative corrections are absorbed by an additional factor K . The initial spectra are obtained from MC@NLO, which combines next-to-leading order pQCD cross sections with a parton shower evolution. No cold nuclear matter effects are taken into account. After the QGP evolution heavy quarks are fragmented via the Peterson fragmentation. In this model, recombination processes are not considered for the hadronization.

The non-perturbative T-matrix approach in a fluid-dynamic model **TAMU** [43] is a transport approach using non-perturbative interactions for heavy quarks, embedded into a hydrodynamic bulk evolution. The elastic heavy-quark scattering in the medium is evaluated within a thermodynamic T-matrix approach using lattice QCD calculations as input. The space-time evolution of the heavy-quark phase-space distribution in the hadronic matter is computed using the Fokker-Planck equation. The resonance recombination model is used to hadronize the quarks. The hadronization contains recombination effects. The initial heavy quark production is realized with FONLL and shadowing of the nuclear PDFs using the EPS09 (NLO) set is included. Radiative processes, which should improve the description at high p_T , are not included in this approach.

2.2. Open heavy-flavour production measurements

In this section, the most important measurement techniques are explained and some of the recent measurements at the LHC, particularly interesting in the context of this thesis, for the nuclear modification factor R_{AA} and the elliptic flow v_2 are shown.

2.2.1. Measurement techniques

Different methods exist to measure charm and beauty hadrons [31]. They make use of the distinctive features of charm and beauty hadron decays. The D^0 , D^+ and D_s^+ mesons have mean proper decay lengths $c\tau$ of approximately 120, 310 and 150 μm respectively, whereas beauty hadrons have longer lifetimes than charm hadrons with $c\tau \approx 500 \mu\text{m}$. Most of the beauty-hadron decay channels proceed via $b \rightarrow c$ hadron cascades, thus the topology contains both a secondary and a tertiary decay vertex. To exploit these features one must resolve the decay vertex of heavy-flavour from the primary vertex, which requires detectors with high spatial resolution. In addition, on average the beauty hadrons decay into more daughters than the charm hadrons. In the following, the most important measurement techniques are explained.

In **fully reconstructed decays of charm and beauty hadrons** HF hadrons are reconstructed via hadronic decays of D-mesons and B-mesons. The branching ratios are smaller than those in semi-leptonic channels, but this technique gives full access to the kinematics of the HF hadron. D-mesons are reconstructed from the decays $D^0 \rightarrow \pi^+ + K^-$, $D^+ \rightarrow \pi^+ + \pi^+ + K^-$ and $D^{*+}(2010) \rightarrow D^0 + \pi^+$, and their charge conjugates. B-mesons can for example be reconstructed in the channels $B^+ \rightarrow J/\psi K^+$ or $B^+ \rightarrow D\pi^+$.

In **inclusive measurements of heavy-flavour decay leptons** HF are measured via electrons and muons from semi-leptonic decays of charm and beauty hadrons. The branching ratios are of the order of 5-15 %. Crucial for the measurements are the lepton identification and the subtraction of the background due to leptons not coming from HF hadron decays. The beauty contribution can be obtained by separating charm and beauty through a fit of the impact-parameter distribution based on the longer lifetime of beauty hadrons, which results in a larger separation of the secondary vertex from the primary vertex. This approach requires tracks with very precise impact parameters. The main limitation of the beauty measurement via single leptons is that the correlation between the measured momentum of the lepton and the one of the parent B-meson is very broad, especially at low momentum.

The beauty contribution can also be measured via **non-prompt J/ψ** . The fraction of J/ψ coming from B decays can be measured by decomposing the J/ψ yield into its prompt and non-prompt components. This is achieved via template fits to the pseudo-proper decay length of the beauty hadron. This approach will be used in the analysis of this thesis and will be explained in more detail in chapter 4. Compared to the measurement of beauty-decay leptons, this channel provides a more direct measurement of the kinematics of the parent beauty hadron since the correlation between the momentum of the J/ψ and the beauty hadron is narrower.

Reconstructed jets associated with beauty hadrons can be identified using an algorithm that exploits the relatively long lifetime and large mass of beauty hadrons (b-tagging). Measurements of b-jets are complementary to those of beauty hadrons, since they are typically performed in a higher momentum range.

2.2.2. Nuclear modification factor measurements at the LHC

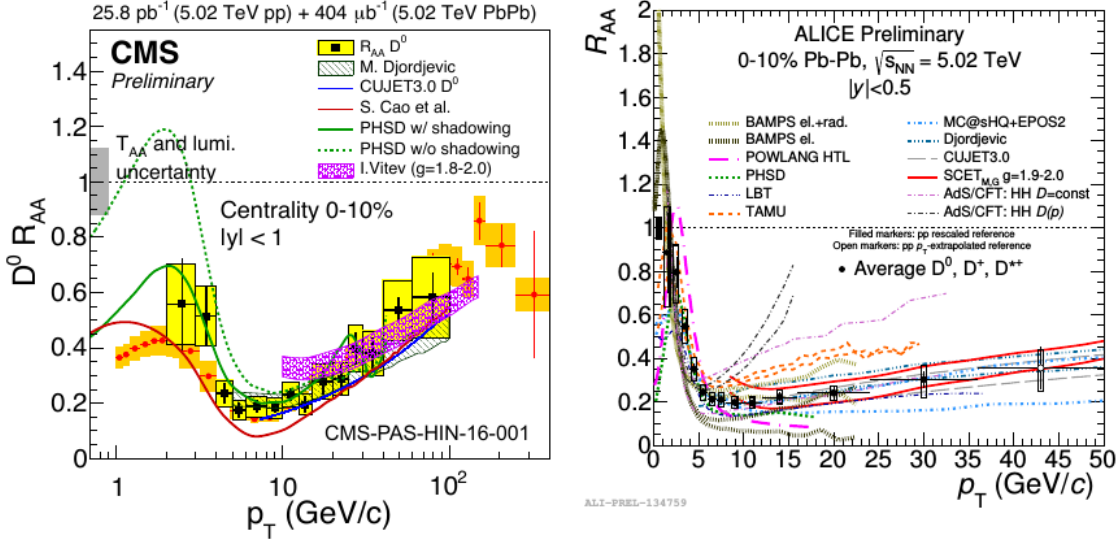
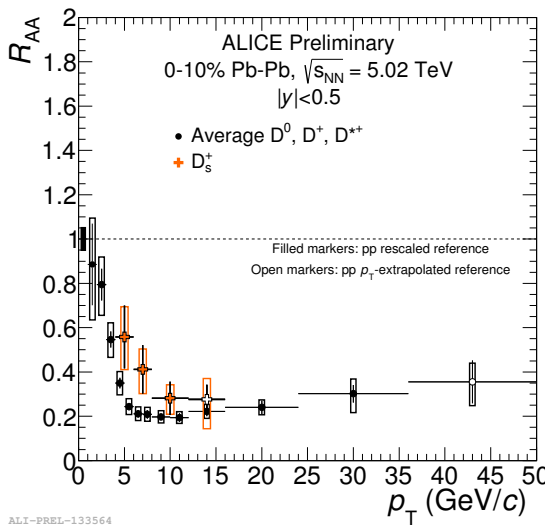
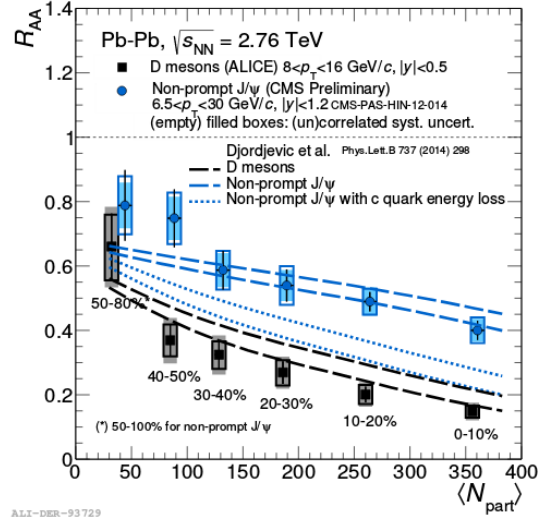


Figure 14: Left panel: comparison of the measured D -meson R_{AA} by CMS at $\sqrt{s_{NN}} = 5.02$ TeV for the 0–10% centrality class with various model predictions [36]. Right panel: D -meson R_{AA} for averaged D^0 , D^+ , D^{*+} mesons by ALICE at $\sqrt{s_{NN}} = 5.02$ TeV for the 0–10% centrality class compared to various models. The figure is taken from [44].

In Fig. 14 the R_{AA} in Pb–Pb is shown for D^0 mesons measured by the CMS experiment in the rapidity range $|y| < 1.0$ at $\sqrt{s_{NN}} = 5.02$ TeV for the 0–10% centrality class and the R_{AA} in Pb–Pb for averaged D^0 , D^+ , D^{*+} by ALICE in the rapidity range $|y| < 0.5$ at $\sqrt{s_{NN}} = 5.02$ TeV for the 0–10% centrality class [44]. A strong suppression is seen in both measurements. For high p_T the R_{AA} goes up to ≈ 0.6 . Overlaid are many different model predictions. Summarized one can say that in most of the cases the models need to contain radiative energy loss to describe the data at high p_T . There are some hints that collisional energy loss is not negligible at low p_T . The usage of shadowing for the nuclear PDFs improves the description of the data at low p_T . In Fig. 15a the R_{AA} measured by ALICE shown in the right panel of Fig. 14 is compared to the R_{AA} of the D_s^+ meson. A hint for an enhancement of the ratio D_s^+/D is seen. As discussed in chapter 2.1.3 this might indicate that coalescence is a relevant production mechanism for charm. In Fig. 15b the R_{AA} of non-prompt J/ψ in Pb–Pb collisions at $\sqrt{s_{NN}} = 2.76$ TeV in the p_T range $6.5 < p_T^{J/\psi} < 30$ GeV/c measured by CMS [45] is compared as a function of centrality to the D -meson R_{AA} measured by the ALICE Collaboration in the interval $8 < p_T < 16$ GeV/c [46]. Thus the p_T distributions of the B-mesons decaying to J/ψ particles overlap with the p_T distribution of the D -mesons. It is



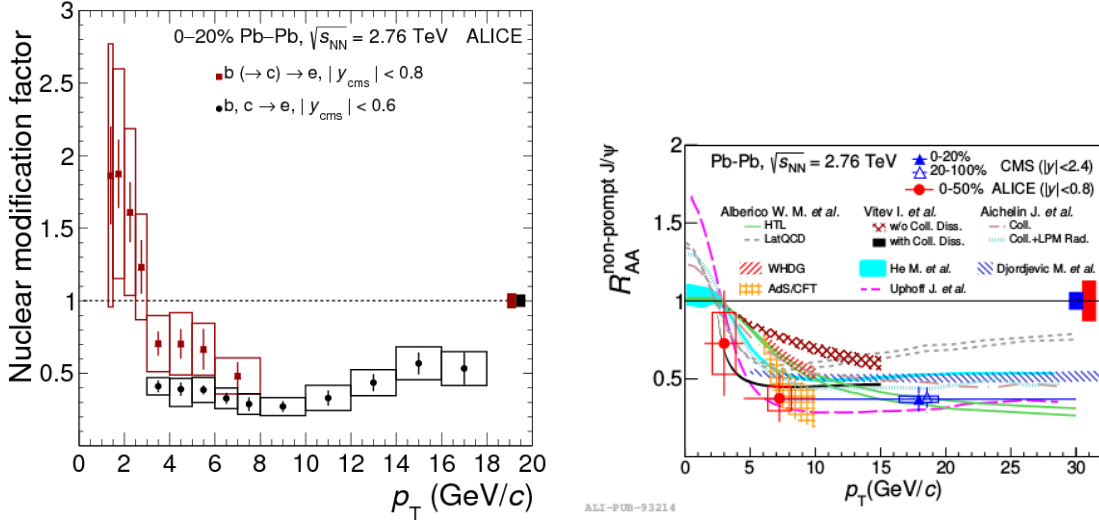
(a) Comparison of the R_{AA} in Pb–Pb for averaged D^0 , D^+ , D^{*+} mesons and D_s^+ by ALICE in the rapidity range $|y| < 0.5$ at $\sqrt{s_{NN}} = 5.02$ TeV for the 0 – 10% centrality class [44].



(b) Non-prompt J/ψ measured by CMS [45] and prompt D-meson R_{AA} measured by ALICE [46] as a function of centrality compared to the prediction of Djordjevic. For non-prompt J/ψ an additional calculation is shown in which the beauty-quark interactions are calculated using the charm-quark mass.

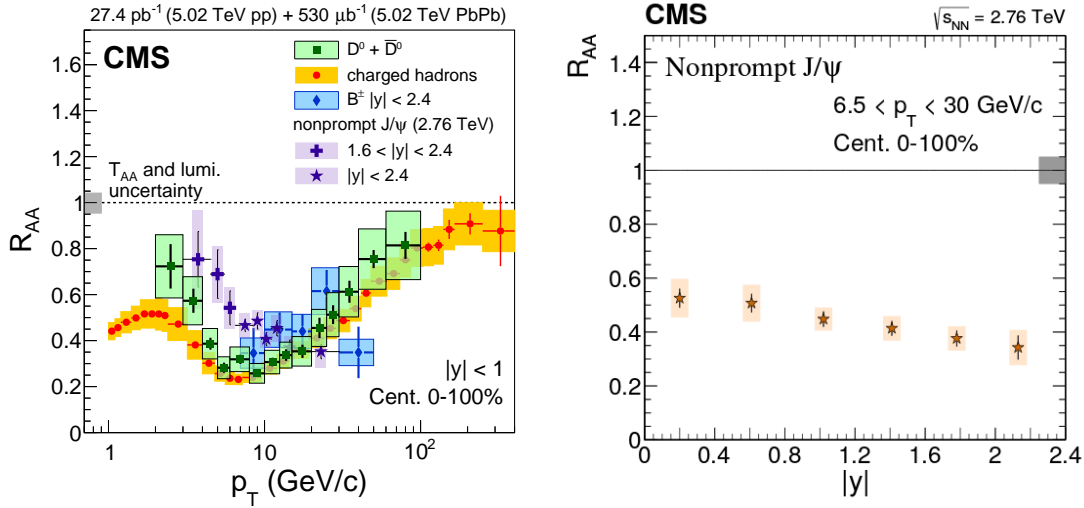
seen that the values for the D-meson R_{AA} are lower than that of non-prompt J/ψ mesons. This measurement is particularly interesting to investigate whether the expected hierarchy in the parton energy loss $\Delta E_g > \Delta E_u, d, s > \Delta E_c > \Delta E_b$ can be observed. However the experimental observation of $R_{AA}^D < R_{AA}^{J/\psi \leftarrow B}$ alone does not allow to draw conclusions for this, since effects, as e.g. different p_T distributions of the initially produced charm and beauty quarks could contribute to differences in the R_{AA} . The measurement is compared with the calculations by Djordjevic et al. [41], which, as discussed in chapter 2.1.5, include both radiative and collisional energy loss processes. In addition the R_{AA} of non-prompt J/ψ was computed assuming the charm-quark mass value in the calculation of the interactions of beauty quarks. This leads to a substantially lower R_{AA} of non-prompt J/ψ , close to that of D-mesons, as compared to the case in which the beauty-quark mass is used in the calculation. This indicates that in this model the difference in the R_{AA} of D-mesons and non-prompt J/ψ is mainly due to the mass dependence of quark-medium interaction [31].

In Fig. 16a a measurement of the beauty contribution from the semi-electronic decays of heavy-flavours through a fit of the impact parameter distribution by ALICE at $\sqrt{s_{NN}} = 2.76$ TeV is shown for the 0-20% most central collisions [47]. It gives a hint of less suppression for electrons coming from B decays than for electrons coming from inclusive decays. In Fig. 16b a measurement of the non-prompt J/ψ R_{AA} at mid-rapidity by ALICE at $\sqrt{s_{NN}} = 2.76$ TeV in the centrality class 0 - 50% [49] is shown together with results from CMS at $\sqrt{s_{NN}} = 2.76$ TeV in the centrality class 0 - 100% [45]. A suppression is observed for intermediate



- (a) R_{AA} of electrons from beauty-hadron decays [47] together with the corresponding result for beauty- and charm-hadron decays [48] for the 20% most central Pb-Pb collisions measured by ALICE.
- (b) The non-prompt J/ψ R_{AA} as a function of p_T at mid-rapidity in Pb-Pb collisions at $\sqrt{s_{NN}} = 2.76$ TeV [49] and CMS [45] for the 0-20% and 20-100% centrality class are shown together with various models.

Figure 16



- (a) Comparison of the R_{AA} of charged hadrons [50], D^0 mesons [36], exclusively reconstructed B^+ mesons [51] and non-prompt J/ψ [52] for the 0-100 % centrality class measured by CMS. The figure is taken from [53].
- (b) Nuclear modification factor as a function of rapidity for non-prompt J/ψ in Pb-Pb collisions at $\sqrt{s_{NN}} = 2.76$ TeV measured by CMS [52].

Figure 17

and high p_T . It is important to note that in both measurements by ALICE the uncertainties at low transverse momentum are very large and do not allow to draw conclusions whether a suppression (or an enhancement) of the R_{AA} is observed for low momentum.

The most recent measurement by CMS at $\sqrt{s_{NN}} = 2.76$ TeV in the centrality class 0-100% for non-prompt J/ψ can be seen in the left panel of Fig. 17a [52]. The measurements are done in the rapidity range $1.6 < |y| < 2.4$ in the p_T range $3 < p_T < 6.5$ GeV/c and in mid-rapidity for the p_T range $6.5 < p_T < 30$ GeV/c. Also shown is the exclusive B^+ measurement by CMS in the 0 - 100% centrality class at $\sqrt{s_{NN}} = 5.02$ TeV at mid-rapidity [51]. For the non-prompt J/ψ and the exclusive B measurements a strong suppression is seen. The measurements are compared to D^0 -mesons [36] and charged hadrons in the rapidity $|y| < 1$ [50]. No significant difference in the R_{AA} for light and heavy particles is seen. There is a hint of a less suppressed R_{AA} for non-prompt J/ψ compared to the R_{AA} of D-mesons for $p_T < 10$ GeV/c. In general the consistency of the R_{AA} for the different flavour in the p_T range of ~ 10 GeV/c is surprising, since basically all energy-loss models predict less B-meson suppression than for D-mesons and charged hadrons. However predictions for the suppression of the hadrons convolve the initial p_T spectra with energy loss and fragmentation functions. Therefore there can be a non-trivial momentum dependence to the flavour ordering predictions as a function of momentum [32]. In Fig. 17b it is shown that the R_{AA} as a function of rapidity for non-prompt J/ψ in Pb-Pb collisions at $\sqrt{s_{NN}} = 2.76$ TeV [52] measured by CMS shows a decrease of the R_{AA} with increasing rapidity. This cannot be explained by any model so far.

2.2.3. Azimuthal anisotropy measurements at the LHC

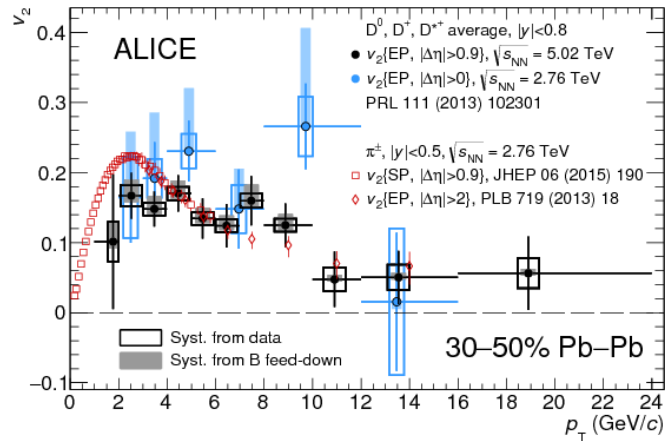
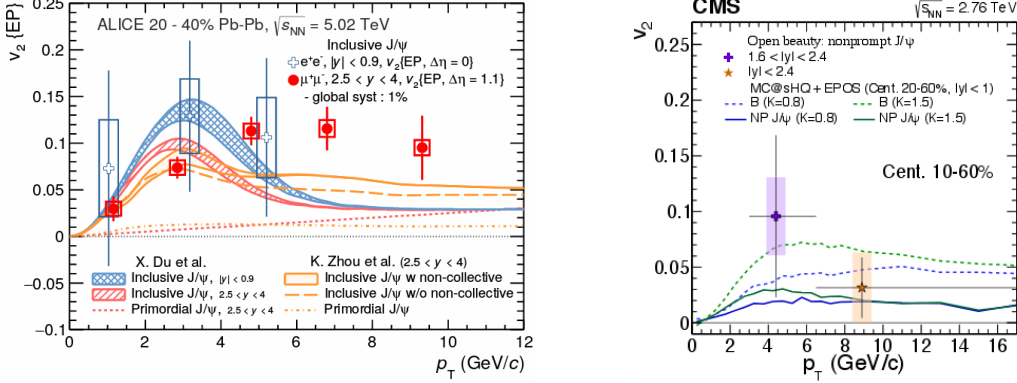


Figure 18: Average of D^0 , D^+ , D^{*+} v_2 as a function of p_T at $\sqrt{s_{NN}} = 5.02$ TeV, compared with the same measurement at $\sqrt{s_{NN}} = 2.76$ TeV, and to the π^\pm v_2 measured with the EP method and with the scalar production (SP) method [54].

The azimuthal anisotropy of particle production in heavy-ion collisions is measured using the Fourier expansion of the azimuthal angle (Φ) and the p_T -dependent particle distribution $d^2N/dp_T d\Phi$. The ALICE Collaboration measured the v_2 of average D^0 , D^+ , D^{*+} -mesons as a function of p_T at $\sqrt{s_{NN}} = 5.02$ TeV and at

$\sqrt{s_{NN}} = 2.76$ TeV. This is shown in Fig. 18. It is compared to the π^\pm v_2 . The measurements are done with the event plane (EP) method and with the scalar production (SP) method [54]. The results are in good agreement with CMS results at the same energy [55]. There is a strong indication of a non-zero D^0 -meson v_2 .



(a) Inclusive J/ψ v_2 at forward and mid-rapidity for semi-central Pb–Pb collisions at $\sqrt{s_{NN}} = 5.02$ TeV by ALICE [56]. (b) v_2 of non-prompt J/ψ in Pb–Pb collisions at $\sqrt{s_{NN}} = 2.76$ TeV measured by CMS [52].

Figure 19

In Fig. 19a the v_2 for inclusive J/ψ at forward and mid-rapidity for semi-central (20-40%) Pb–Pb collisions at $\sqrt{s_{NN}} = 5.02$ TeV measured by ALICE [56] is shown. The results show for the first time that J/ψ mesons exhibit collective flow. This measurement of the J/ψ elliptic flow (combined with the R_{AA}) provides substantial evidence that the charm quark is thermalized. CMS also measured the v_2 of non-prompt J/ψ , shown in Fig. 19b. The results are in agreement with the theoretical models, however within very large statistical uncertainties.

2.2.4. Conclusions and motivation of the thesis

In heavy-ion collisions the nuclear modification factor shows large deviations from unity and the measured elliptic flow large values for charm particles. The increasing precision of the HF measurements starts to put strong constraints on theoretical models that have to reproduce both the R_{AA} and the v_2 at the same time. Several approaches of the models show a qualitative or semi-quantitative agreement with existing data. The main components in modeling are the initial heavy-quark spectra and their modifications due to shadowing, the bulk evolution, the transport coefficients in the QGP, and hadronization. At the moment the existing models use different ingredients for the components. It has to be understood how the extraction of the transport coefficients is affected by the different components. The main challenges in the theory sector is to connect the data with the fundamental properties of the QGP and of the theory of QCD. Lattice results for the HF diffusion coefficient in full QCD can serve as a benchmark for effective-theory calculations that make a bridge between lattice-QCD and experiment. More precise data on the R_{AA} and v_2 of D and B-mesons, charm-strange mesons and charm baryons down to low p_T is needed to understand the different

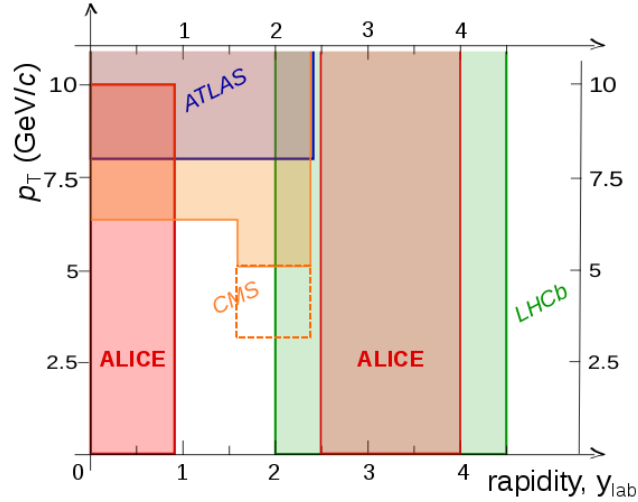


Figure 20: Acceptance in rapidity and transverse momentum of J/ψ measurements for ALICE, LHCb, ATLAS and CMS, taken from [57] and extended for the now larger range of CMS.

mechanisms and finally obtain precise results of the charm and beauty transport coefficients.

The low- p_T region is particularly interesting because of its sensitivity to the HF diffusion coefficient D_s . Moreover measurements of R_{AA} and v_2 of different HF hadron species at low p_T are expected to quantify the degree to which charm and beauty particles participate in the collective expansion of the system which reflects their coupling strength to the medium. The importance of low p_T measurements, the fact that beauty observables provide the cleanest probe of the QGP and the high uncertainties of existing beauty measurements at low transverse momentum motivates the measurement of this thesis of non-prompt J/ψ production at $\sqrt{s_{NN}} = 5.02$ TeV with the ALICE experiment, which, as indicated in Fig. 20, is the only experiment at the LHC that has access to a measurement at mid-rapidity up to zero transverse momentum.

3. ALICE

ALICE is an acronym for A Large Ion Collider Experiment and is one of the four main experiments at the Large Hadron Collider (LHC) at CERN, Geneva. ALICE is optimized for the extreme charged particle multiplicities arising from the collision of heavy nuclei and thus provides excellent conditions to study the behaviour of matter under extreme temperatures and densities. In the following an overview of the detector will be given with special emphasis on the issues related to the reconstruction of the charged particle tracks [58] [59] [60].

3.1. The Detector

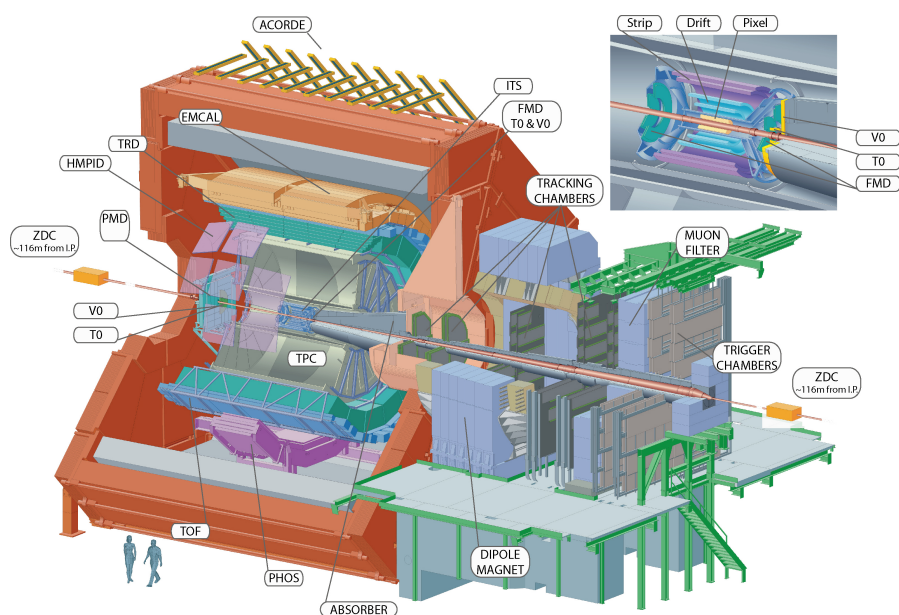


Figure 21: Overview over the ALICE detector [58]

The ALICE detector is presented in figure 21. Beginning from the collision point, the detector consists out of the following elements. The central barrel detectors: the Inner Tracking System (ITS) used for the high precision determination of vertices and tracking, the Time Projection Chamber (TPC) that serves as the main tracking element and provides particle identification (PID) via dE/dX measurements, the Transition Radiation Detector (TRD) used for the tracking and the identification of charged particles via transition radiation and dE/dX , the Time-Of-Flight (TOF) that provides PID via the measurement of the particle velocity at intermediate momenta, the Electromagnetic Calorimeter (EMCal), the Photon Calorimeter (PHOS) and the High Momentum Particle Identification Detector (HMPID). ITS, TPC, TRD and TOF cover the entire azimuthal range, and a pseudo-rapidity range of about $|\eta| < 0.9$ and are divided in 18 segments in azimuth. Sectors in azimuth for TRD, PHOS and EMCal have been added over the years. The central barrel detectors are surrounded by a solenoid magnet that provides a magnetic field of maximal 0.5 T.

In the forward rapidity region the Photon Multiplicity Detector (PMD) and the

Forward Multiplicity Detector (FMD) measure photons and charged particles. The T0 detector measures the time and the longitudinal position of the interaction, while the V0 detector measures charged particles and is used for triggering and the measurement of centrality and the angle of the event plane in Pb-Pb. To resolve the ambiguity between the most central and the most peripheral collisions, that both have few spectator nucleons, an electromagnetic calorimeter (ZEM) is used. The Zero Degree Calorimeter (ZDC) is used for measurements of the centrality. Light vector mesons and J/ψ in the dimuon channel are measured by the MUON spectrometer in forward rapidity, as well as high- p_T muons originating from charm and beauty decays.

In the following the detector parts, particularly relevant for the analysis presented in this thesis will be introduced in more detail.

3.2. The V0 detectors

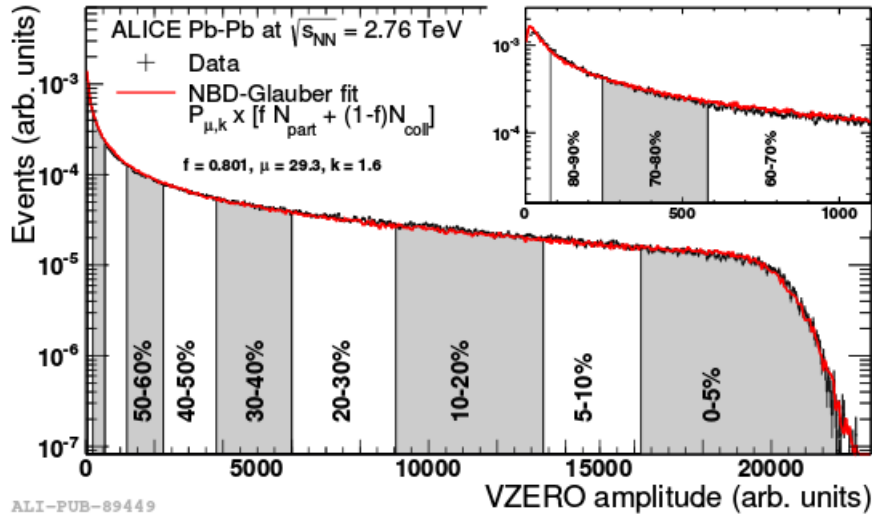


Figure 22: Centrality measurement of spectator nucleons by the V0 detector in ALICE [58].

The V0 detector consists of two subsystems called V0A and V0C. They are scintillator arrays on either side of the interaction point at the pseudo-rapidity intervals $-3.7 < \eta < -1.7$ and $2.8 < \eta < 5.1$.

The V0 detector was used as minimum-bias trigger detector in the data taking period analyzed in the scope of this thesis, based on a coincidence of signals in both scintillator arrays.

The distribution of the V0 amplitude (sum of V0A and V0C) that can be seen in Fig. 22. was fitted with the Glauber model [58]. The fit relates the number of participants and binary nucleon-nucleon collisions to the centrality.

3.3. The Inner Tracking System

The detector consists of six cylindrical layers of silicon-based detectors with a pseudo-rapidity coverage of $|\eta| < 0.9$ for the full detector [58]. The ITS is designed to determine the primary vertex and displaced secondary vertices coming from

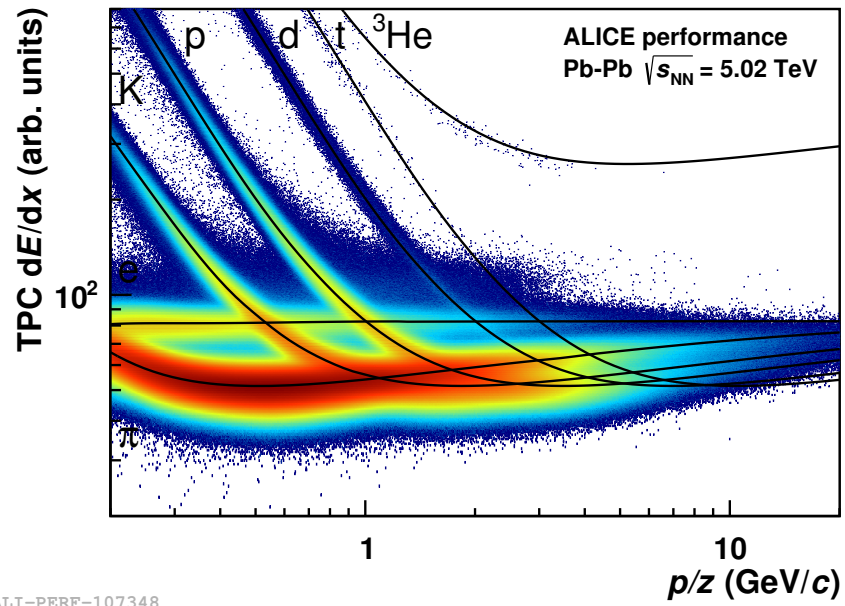
heavy-flavour decays with a precision in the order of a few tens of microns. The spatial resolution is presented in table 1. Moreover, the ITS provides PID for low momentum tracks and improves the momentum resolution compared to the TPC stand-alone tracking. It is also possible to reconstruct tracks at very low momenta or high momenta, that traverse the TPC in blind regions by a standalone tracking algorithm. Due to the high particle density in the first two layers, Silicon Pixel Detectors (SPD) have been chosen for the first two layers and Silicon Drift Detectors (SDD) for the following two layers. The high resolution of these silicon detectors also provide a precise measurement of the impact parameter. The outer two layers, where the hit density is lower, are equipped with Silicon Strip Detectors (SSD). The first two layers have an extended η range. Since the resolution of the momentum and the impact parameter is dominated by multiple scattering effects for low momenta, the material budget of the silicon detectors are kept to the minimum. The ITS is crucial for the global track fit and the track quality depends heavily on the hits in the ITS, in particular the first two layers are crucial for the resolution of the track.

Table 1: Resolution of the main tracking devices [60]

Detector	Radius R (cm)	η range	Res. $R\phi$ (μm)	Res. z (μm)
SPD	3.9 & 7.6	—1.98—	12	100
SDD	15.0 & 23.9	—0.9—	38	28
SSD	37.8 & 42.8	—0.9—	20	830
TPC	84.5 - 246.6	—0.9—	1100 - 800	1250 - 1100

3.4. The Time Projection Chamber

The TPC is the main tracking detector in ALICE. It provides robust and efficient tracking in a large momentum range, as well as a high momentum resolution and is optimized for very high particle densities [58]. The TPC is divided into two volumes, separated by an electrode that generates the drift field. The cylindrical field cage of the TPC is filled with a gas mixture. The primary electrons caused by the traversing of a charged particle drift to the end plates on either side. Here multi-wire proportional chambers with cathode pad readout divided in 18 trapezoidal sectors are installed. Via the readout plates a radial coordinate R and an azimuthal coordinate ϕ is obtained. The third coordinate in z direction is calculated from the drift time of the electrons. The maximal numbers of cluster that can be measured in the TPC is 159. An important issue for the TPC is the alignment with the other tracking detectors in order to perform the global track fit. The blind regions between the chambers have significant influence on the spatial resolution and the momentum resolution of tracks traversing these sectors. The PID signal of the TPC associated to a track is retrieved from a truncated mean of the distribution of the charge associated to the clusters of a given track. As the deposit charge is proportional to the energy lost per unit length dE/dx , a fit with the ALEPH TPC Bethe-Bloch parameterization [60] for each particle type is used to give a hypothesis on the true particle mass and species. The particle identification in PbPb collisions is shown in Fig. 23 as a function of rigidity, where



ALI-PERF-107348

Figure 23: Specific energy loss of negatively charged particles in Pb–Pb collisions as a function of rigidity.

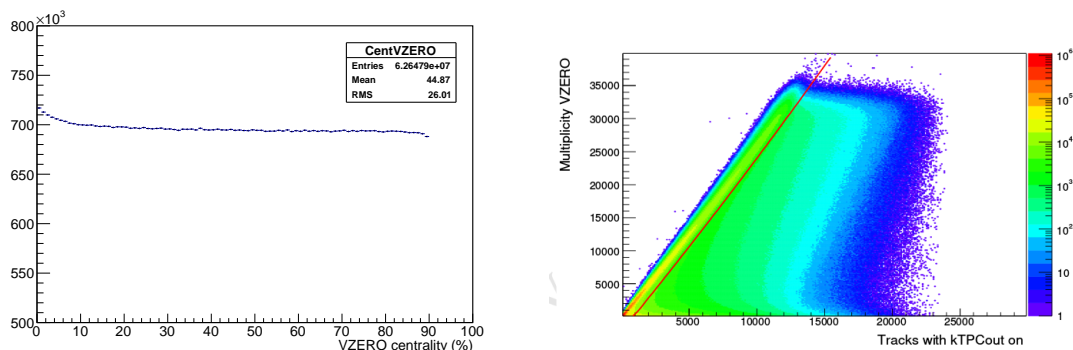
the lines indicate the fitted Bethe-Bloch parameterization. The TPC particle identification capabilities are complementary in terms of momentum coverage to the other central barrel detectors.

4. Non-prompt J/ψ production

4.1. Selection criteria and inclusive J/ψ production

The analysis of the non-prompt J/ψ production is naturally related to the analysis of the inclusive J/ψ production. Thus the same selection criteria for the events and tracks are applied. The J/ψ are reconstructed via their decay into two electrons. In the following an overview over the applied selections and the inclusive J/ψ R_{AA} analysis is given. For details of the (on-going) inclusive analysis it is referred to [61]. This section describes the current status of the analysis. It was carried out by the authors of [61] and is not part of the work done in the context of this thesis. Some figures were added relevant for the analysis of the non-prompt J/ψ production.

4.1.1. Data sample and event selection



- (a) Centrality distribution after the applied event selection. (b) Correlation between the multiplicity measured by the V0 detector and the total number of tracks in the TPC. The events to the right of the red line are rejected. The figure is taken from [61].

Figure 24

For this analysis the reconstruction pass 1 of runs from the Pb–Pb data taking in November and December of 2015, period LHC15o, has been used [61]. The data consist out of approximately 90 million minimum-bias triggered events from the LHC15o HIR pass1 and the LHC15o HIR pass1 pidfix, where HIR denotes high interaction rate (0.2 - 8 kHz). Minimum bias events are selected using the trigger mask kINT7, which is based on coincidence signals in the V0 detectors. In addition a physics selection is applied to ensure a good reconstruction and calibration quality while rejecting background pile-up events. The reconstructed primary vertex in each event was required to have at least one contributing track and a z -coordinate lying within $[-10, 10]$ cm from the nominal center of the experiment. The centrality is estimated using the V0 centrality estimator and is considered in the interval 0-90 %. It is shown in Fig. 24a. In order to remove events containing pile-up, a selection on the correlation between the multiplicity measured by the V0 detector and the total number of tracks that are occupying the TPC is applied

which is shown in Fig. 24b. The choice of the parameters for the selection is based on the low interaction rate runs, where no pileup is observed. The applied formula is:

$$y > 2 \times 10^{-5}x^2 + 2.5x - 2200 \quad (18)$$

For the Monte-Carlo (MC) simulation the production LHC16j1 is used [61]. It is anchored to the LHC150 pass1 period and reproduces the respective run conditions. It consists of 10^6 minimum-bias events using HIJING as generator with J/ψ injected signals. The prompt to non-prompt ratio of the injected J/ψ signals is 70:30. For the prompt J/ψ a realistic p_T spectra is used between 0 - 6 GeV/c, while between 0 - 0.5 GeV/c and 6 - 25 GeV/c a flat component is added. This can be seen in Fig. 25.

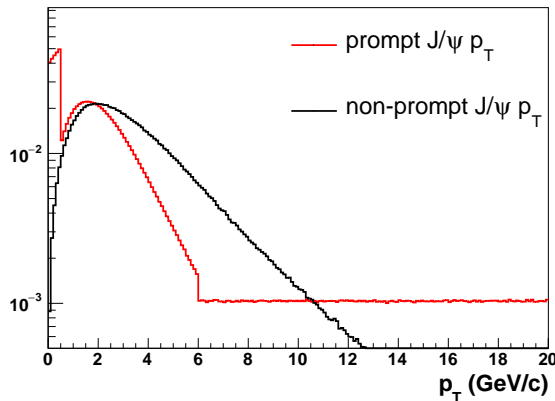


Figure 25: Generated p_T spectra for the prompt and non-prompt MC J/ψ components.

The propagation of the simulated particles is done by GEANT3 and a full simulation of the detector response is performed.

4.1.2. Track selection

On top of the event selections, track selections are applied [61] in order to select high-quality electron candidates. It is required that the selected tracks have at least one SPD hit. This reduces the contribution from secondary electrons from γ -conversions. Further it is required that the selected tracks are successfully refitted both in the ITS and TPC. This implies a minimum of two clusters out of the six possible clusters in the silicon layers of the ITS. For the TPC a χ^2 per number of clusters $\chi^2/n_{cls}^{TPC} < 2.5$ and a minimum of 70 clusters is required. For the ITS a χ^2 per number of clusters $\chi^2/n_{cls}^{ITS} < 10$ is required and the fraction of shared ITS clusters has to be smaller than 0.4. The latter two selections are applied in order to further reduce the contributions from γ -conversions. Loose requirements are applied to the impact parameter of the tracks in order to not reject non-prompt J/ψ . The distance of closest approach (DCA) in xy has to be smaller than 1 cm and smaller than 3 cm in z direction. As for the kinematic selections, the momentum of the electron is required to be larger than 1 GeV/c and the pseudo-rapidity η of the track has to be within the interval $[-0.9, 0.9]$. The particle identification (PID) is performed based on the specific energy loss (dE/dx) in the TPC. The electron

selection is based on the deviation of the TPC dE/dx from the parametrized value from the Bethe-Bloch formula. This is defined for a particle of type P as follows:

$$n\sigma_P = \frac{dE/dx_{meas} - dE/dx_{BBP}}{\sigma_P} \quad (19)$$

where dE/dx_{BBP} is the expected energy-loss from the Bethe-Bloch parametrization for the particle of species P and σ_P is the energy-loss resolution. Following the central limit theorem the $n\sigma_P$ distribution should follow a Gaussian distribution with center at 0 and width of 1. However deviations from this expectation were found depending on centrality, pseudo-rapidity and run-number. Thus the $n\sigma$ distributions for the electrons are post-calibrated in pseudo-rapidity and centrality for each run [61]. The final distribution of $n\sigma_e$ is shown as function of momentum in Fig. 26.

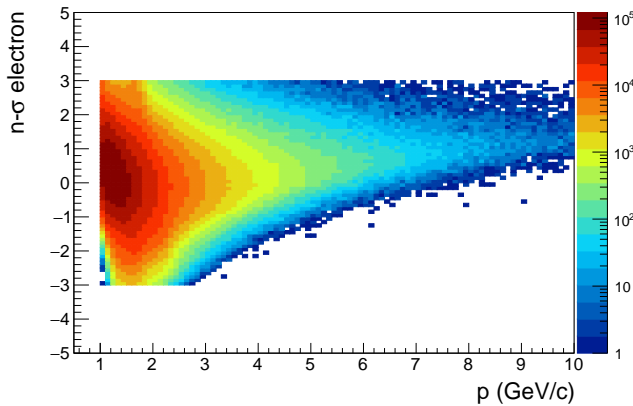


Figure 26: $n\sigma_e$ after calibration as a function of the momentum.

After the corrections, electron candidates are selected by requiring the dE/dx in the TPC to lie in the interval $-3 < n\sigma_e < 3$. To further suppress the hadron contamination, tracks that are compatible with the proton expectation $n\sigma_p < 3.5$ or the pion expectation $n\sigma_\pi < 3.5$ are excluded. It is known that the microscopic description of the energy loss in the MC simulation deviates from the data. Therefore the Monte-Carlo PID is tuned using the Bethe-Bloch parametrization of the data. This leads by construction to a properly calibrated electron PID response in the Monte-Carlo simulation. A similar rejection factor of electron candidates after the application of the same selections in data and MC was observed [61].

4.1.3. J/ψ raw yield extraction

The J/ψ production is measured in three centrality classes 0-20%, 20-40%, 40-90% in the p_T intervals [0.15, 1.3] GeV/c, [1.3, 3] GeV/c, [3, 5] GeV/c, [5, 10] GeV/c. It is also measured as a function of centrality in the centrality classes 0-10%, 10-20%, 20-40%, 40-60% and 60-90% [61].

The invariant mass distribution, constructed with opposite sign pairs of the electron candidates after the selections described in the previous sections is shown in Fig. 27. The combinatorial background is estimated by using three different

methods. The first method uses like-sign pairs that are constructed from the same electron sample and exploits the fact that all signal pairs are opposite sign pairs. The second method mixes electrons from different events with similar properties and thus produces by definition uncorrelated electron pairs. The third method fits the mass spectrum using templates for the signal and background. All three methods give results which are consistent within uncertainties [61]. Since in this thesis exclusively the event mixing is used, it will be described briefly: for the event mixing events with similar global properties are considered. Electrons are combined with positrons from different events. The mixing is performed in categories of the event centrality, the z coordinate of the interaction vertex and the event plane angle Ψ . The following binning is used:

- Centrality: $\{0, 5, 10, 20, 30, 40, 50, 60, 70, 80, 90\}$ %
- Vertex z coordinate: $\{-10, -7, -4, -2, 0, 2, 4, 7, 10\}$ cm
- Event plane angle Ψ (8 bins): $[-\pi/2, \pi/2]$

The invariant mass region selected to scale the background is $1.5 - 4.2 \text{ GeV}/c^2$, excluding the signal region $2.5 - 3.2 \text{ GeV}/c^2$. An example for the background estimation using the event mixing method is shown in Fig. 27. The bottom panel in Fig. 27 shows the signal after background subtraction. The J/ψ signals from Monte-Carlo and the data are in good agreement. The signal shape of the MC is taken from reconstructed J/ψ in the Monte-Carlo simulation after applying the same selections as in data. The raw yield is extracted in the signal window $2.92 \text{ GeV}/c < M_{ee} < 3.16 \text{ GeV}/c$ using bin counting.

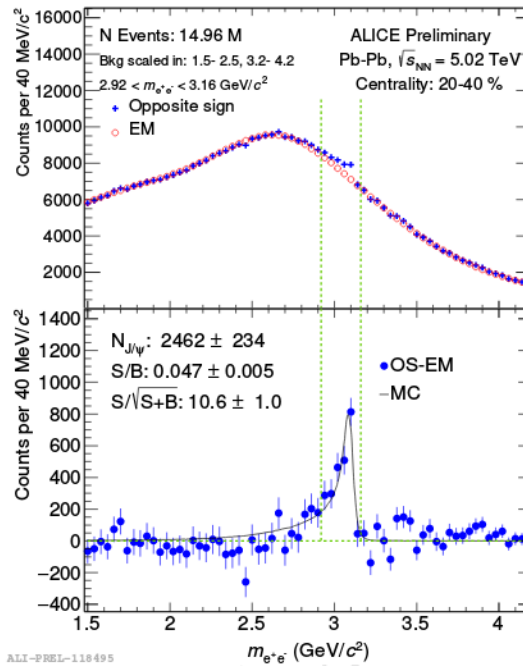


Figure 27: Example for the J/ψ raw yield extraction using the event mixing method [62].

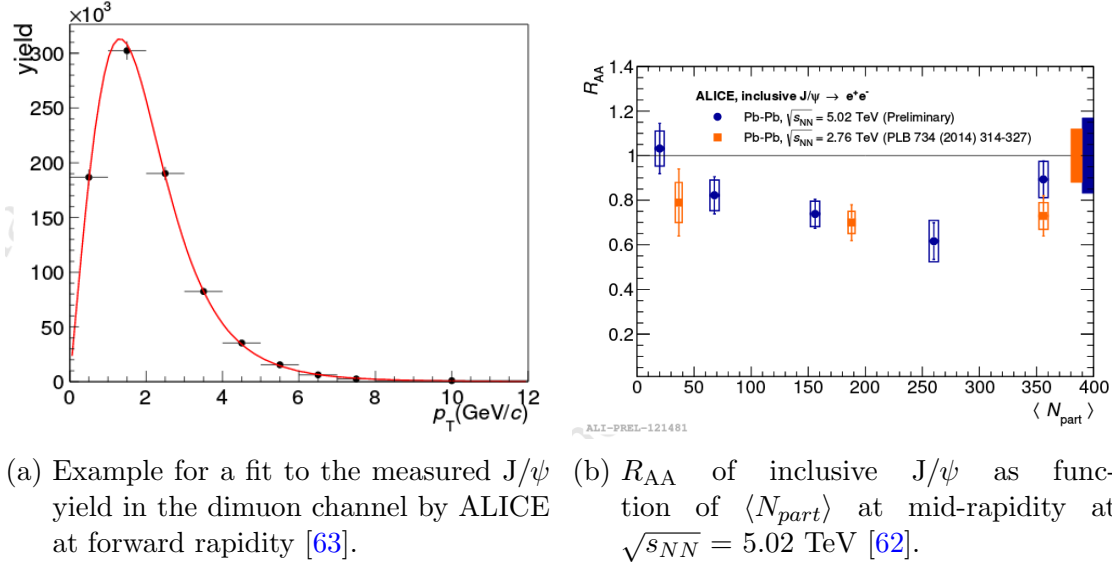


Figure 28

4.1.4. Inclusive R_{AA}

The nuclear modification factor as introduced in chapter 2 is calculated as:

$$R_{AA} = \frac{Y_{J/\psi}^{Pb-Pb}}{\langle T_{AA} \rangle \sigma_{J/\psi}^{pp}} \quad (20)$$

with

$$Y_{J/\psi}^{Pb-Pb} = \frac{N_{J/\psi}^{Pb-Pb}}{BR \times \langle \mathcal{A} \times \mathcal{E} \rangle \times \Delta Y \times N_{events}} \quad (21)$$

where $N_{J/\psi}^{Pb-Pb}$ is the raw yield in Pb–Pb, $\langle \mathcal{A} \times \mathcal{E} \rangle$ the reconstruction efficiency, BR is the branching ratio of the J/ψ decay in the dielectron channel, ΔY the rapidity range and N_{events} is the total number of analyzed minimum bias events. $\langle T_{AA} \rangle$ is the average of the nuclear overlap function for the centrality interval considered obtained using a Monte-Carlo Glauber simulation and $\sigma_{J/\psi}^{pp}$ is the J/ψ cross section from pp collisions at the same center-of-mass energy in the same rapidity window. The total efficiency $\langle \mathcal{A} \times \mathcal{E} \rangle$ to correct the raw yields has to be estimated from MC simulations. It is defined as

$$\langle \mathcal{A} \times \mathcal{E} \rangle = \frac{N_{J/\psi}^{rec,MC}}{N_{J/\psi}^{gen,MC}} \quad (22)$$

where $N_{J/\psi}^{rec,MC}$ is the number of MC J/ψ reconstructed after all track selections and $N_{J/\psi}^{gen,MC}$ is the number of generated MC J/ψ . Due to the unnatural p_T input shape of the MC distribution, a reweighting to the measured J/ψ yield in the dimuon channel by ALICE at forward rapidity [63] is applied. The cross sections for different centrality classes are fitted with the phenomenological function:

$$f(p_T) = C \times \frac{p_T}{(1 + (\frac{p_T}{p_0})^2)^n} \quad (23)$$

An example of the fitted spectra at forward rapidity is shown in Fig. 28a. The fits are used for the weighting of the efficiencies in the different p_T bins.

The systematic uncertainties due to the signal reconstruction and extraction are estimated by varying the selections of the electron candidates. Three groups of variations are considered: variations of the track selections, variations of the signal extraction parameters and variations of the PID selections. For each variation the Barlow criteria is applied [64], which is formulated as:

$$BL = \frac{R_{AA}^{Standard} - R_{AA}^{Varied}}{\sqrt{|\sigma^2(R_{AA}^{Standard}) - \sigma^2(R_{AA}^{Varied})|}} \quad (24)$$

if BL is < 1 the variation is considered to be only statistical, while for $BL > 1$ the variation is a systematic effect. For each of the three groups the RMS of the systematic variations is taken and added in quadrature, so the systematic uncertainty is calculated as:

$$\delta(R_{AA}) = \sqrt{\delta_{PID}^2 + \delta_{tracking}^2 + \delta_{signal\ extraction}^2} \quad (25)$$

Since no reference measurement in pp exists at $\sqrt{s} = 5.02$ TeV, the reference for the nuclear modification factor is constructed by an interpolation of published p_T spectra from pp collisions. A detailed description of the interpolation can be found in [65].

In Fig. 28b the inclusive J/ ψ R_{AA} is shown as a function of centrality [62]. The most recent values for the R_{AA} relevant for the following non-prompt analysis are reported in Tab. 2 [61]:

p_T (GeV/c)	0-20 %	20-40 %	40-90 %
1.3 - 3	$1.07 \pm 0.12 \pm 0.10$	$0.95 \pm 0.12 \pm 0.14$	$0.52 \pm 0.12 \pm 0.12$
3 - 5	$0.62 \pm 0.07 \pm 0.05$	$0.52 \pm 0.08 \pm 0.08$	$0.77 \pm 0.09 \pm 0.11$
5 - 10	$0.27 \pm 0.07 \pm 0.06$	$0.44 \pm 0.07 \pm 0.07$	$0.61 \pm 0.09 \pm 0.09$

Table 2: Inclusive J/ ψ R_{AA} results [61].

4.2. Study of MVA methods

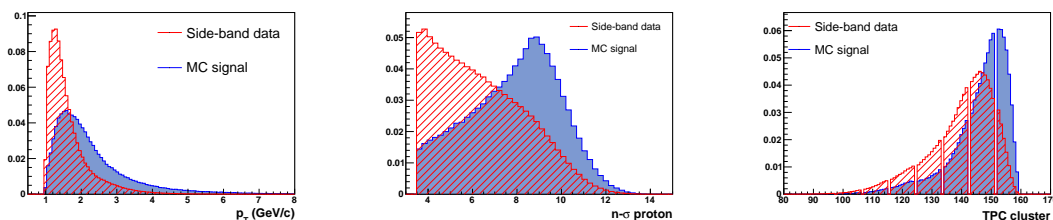


Figure 29: Distribution of the transverse momentum p_T , the proton expectation $n\sigma_p$ and the TPC clusters for the track variables of electrons from Monte-Carlo J/ψ and electrons from pairs in the side-band of the data.

Due to the challenging signal to background (S/B) conditions in the inclusive J/ψ analysis it is an important goal to improve this quantity. A possible improvement is the consideration of additional information to discriminate between signal and background. For this reason the track variables of electron and positron for MC J/ψ and for the side-band of the data are investigated. The side-bands are chosen from 1.5 to 2.3 GeV/c^2 and 3.6 to 5 GeV/c^2 . In Fig. 29 some of the variables that characterize the electron and positron tracks are shown. The left panel shows the transverse momentum, the central panel the proton expectation $n\sigma_p$ and the right panel the number of TPC clusters assigned to the track. The distributions of the variables show that they possess power to provide additional information to discriminate between signal and background. Multivariate analysis (MVA) methods provide the possibility to combine the separation power of single variables into one, more powerful classifier. In the following the possibility to combine several variables of the electron-positron track variables into one final classifier is explored. The goal is to make a selection on a final classifier in order to increase the S/B and significance ($S/\sqrt{S+B}$) of the invariant mass distribution of the inclusive J/ψ .

4.2.1. Introduction to TMVA and Boosted Decision Trees

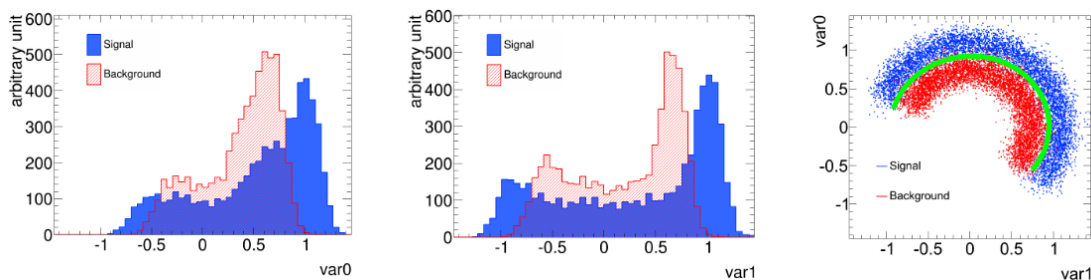
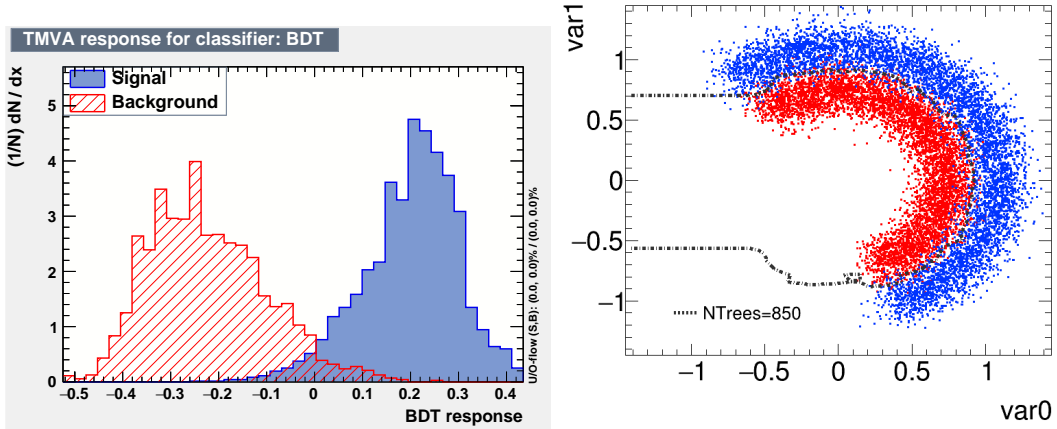


Figure 30: 2-d toy example [66]: In the left and central panel the distributions for the signal and background of two variables x_1 and x_2 is shown. In the right panel the 2-d plot of x_1 and x_2 is displayed, indicating that the optimal decision boundary to discriminate signal from background is circular (green curve).

The Toolkit for Multivariate Analysis (TMVA) [67] provides a ROOT-integrated environment for multivariate classification. The techniques used in the TMVA

are supervised learning algorithms. They make use of training events, for which the output is known, to determine the mapping function to describe the decision boundary. Classification is a prediction to a binary question based on different input variables. The multivariate classification allows to combine several discriminating variables into one, more powerful discriminator, thus creating a map from multiple dimension to only one: $R^d \rightarrow R$. The main advantage of a multivariate analysis is, that it exploits the correlations between variables. This is illustrated in a 2-d toy example in Fig. 30 [66]. It is shown that each of the two variables, x_1 and x_2 possess some power to discriminate signal and background. In the right panel the 2-d plot of both variables is shown. A (artificial) circular correlation between the two variables exists. Thus in this toy example the best decision boundary is a circular curve. Applying "classical" selections, based on cut optimization, to the single variables x_1 and x_2 to discriminate signal and background corresponds to selecting a rectangle in the 2-d plot as decision boundary. However it is obvious that a rectangular decision boundary cannot achieve the same performance in separating signal and background as a circular one does.



(a) Classifier after the training of a Boosted Decision Tree with TMVA for the variables x_1 and x_2 [66]. (b) Visualization of the decision boundary for a selection of values above 0 for the BDT classifier shown in a) [66].

Figure 31

The used sample for the toy model is split into a training and a test sample. In Fig. 31a the classifier of a Boosted Decision Tree (BDT), trained with the training sample, is shown, where the variables x_1 and x_2 were used as input variables. It illustrates the much stronger separation power of the BDT classifier compared the separation power of the single variables. In Fig. 31b the decision boundary is drawn for the test sample after applying a selection on the BDT classifier at 0. The decision boundary is non-linear and close to a circle, resulting in a strong separation between signal and background.

In the following analysis a Boosted Decision Tree (BDT) is used. A decision tree is a tree structured classifier, where repeated binary decisions are taken on one single variable at a time until a stop criterion is reached [67]. Each new decision depends on the decisions made before. Like this the phase space is split into

many hypercubes (while a "classical" analysis that is based on optimizing cuts on single variables selects only one hypercube). Each hypercube is either classified as signal or background, depending on the number of training events in the final node. The algorithm is shown schematically in Fig. 32. The training of a decision tree is the process that defines the splitting criteria for each node. At each node the split is determined by finding the variable and the corresponding selection value that provides the best separation between signal and background. Different separation criteria exist in the TMVA tool, however all are expected to reach a similar performance. Within the TMVA, the results of the training is stored in weight files. Based on the weights, the BDT response value is calculated in the interval $[-1, 1]$, where values close to 1 are considered signal-like, while values close to -1 are considered background-like. The boosting of a decision tree [67] extends the concept from one tree to several trees which form a forest. The trees are derived from the same training ensemble by reweighting events, and are finally combined into a single classifier. Boosting stabilizes the response of the decision trees with respect to fluctuations in the training sample and improves the overall performance. In this analysis the Gradient Boost algorithm is used [67].

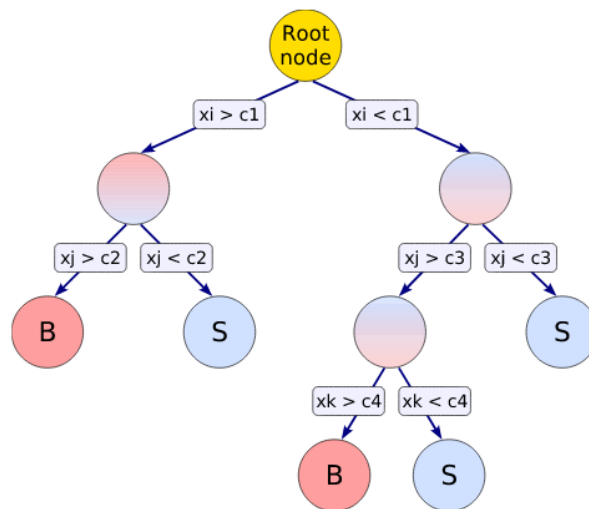


Figure 32: Scheme of a decision tree. Starting from the root node, the data is split using the discriminating variables x_i . Each split uses the variable that at this node gives the best separation between signal and background. Therefore some variable might be used at several nodes, while other variables might not be used at all. Depending on the majority of events that end up in the final leaf node, the nodes are considered signal-like ("S") or background-like ("B") [67].

The main advantages of the BDT are the simplicity of the method, the fast training compared to other methods and the little tuning of the parameters that is required in order to obtain reasonably good results [67]. The disadvantage is that BDTs can be easily overtrained, which means that they learn statistical fluctuations from the training sample. Thus it is mandatory to split the data sample in a training and test sample to ensure that the performance is similar for both samples.

4.2.2. Choice of the input variables

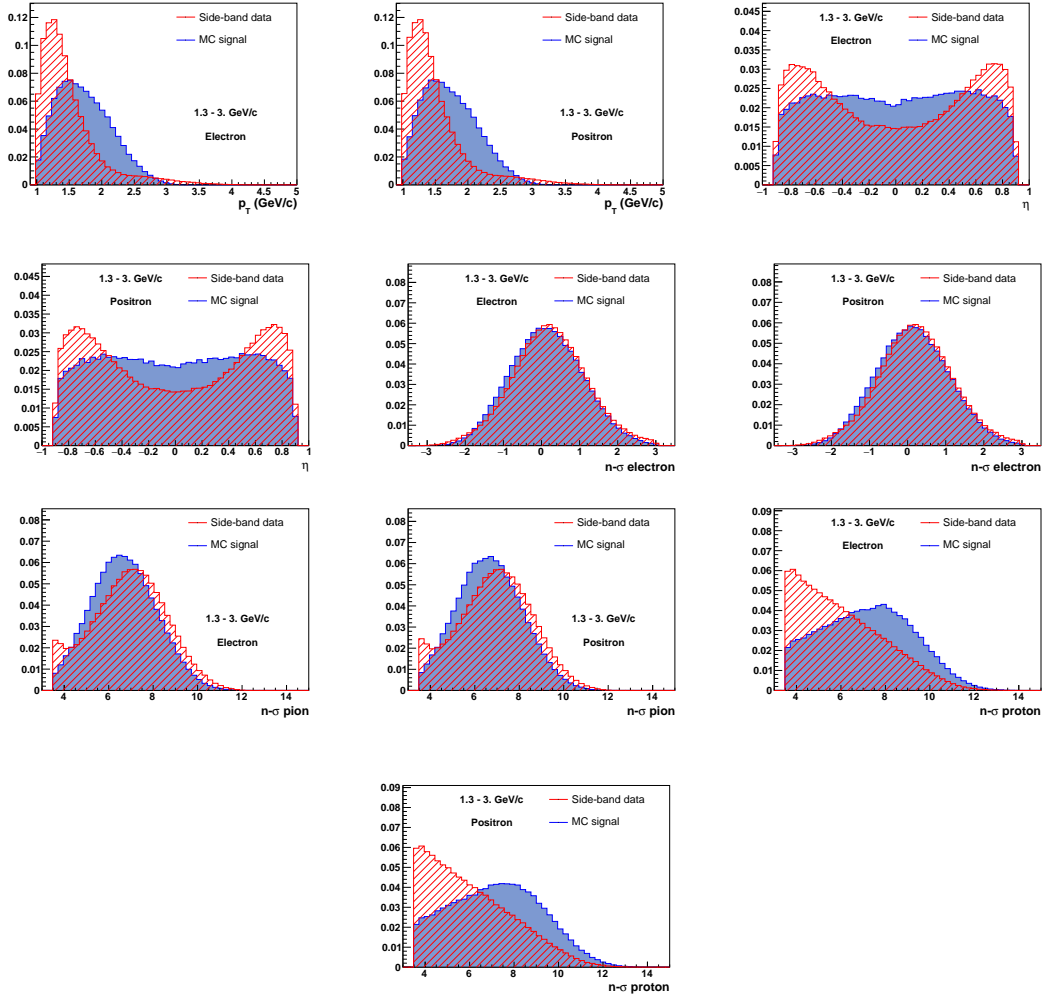


Figure 33: Input variables for the training of the Boosted Decision Tree in the $[1.3, 3]$ GeV/c p_T interval.

Previous attempts to improve the signal to background and the significance have shown that the critical issue is the correction of the measured J/ψ raw yield for the acceptance times efficiency using the Monte-Carlo simulation. Since the number of particles that are measured in the detector is only a fraction of the real number of particles that are produced, the raw yield needs to be corrected. To calculate the acceptance times efficiency, the same selections are applied to MC as are applied in data. A good agreement between MC and data is required. Differences between data and MC reflect in higher systematic uncertainties of the corrected yield. Thus applying methods to improve the signal to background, that cannot be described in MC, will increase the systematic uncertainties. From previous analysis it is known that variables of the tracks that are directly related to the TPC and ITS, as e.g. the number of assigned clusters, show differences in MC and data. Thus for the scope of this work these variables are not considered. Moreover variables that might change the fraction of prompt and non-prompt J/ψ , as e.g. the impact parameter of the tracks in xy and z to the primary vertex are excluded. As a

starting point variables related to the kinematics and PID of the electron and positron tracks are chosen:

- Electron expectation: $n\sigma_e$
- Proton expectation: $n\sigma_p$
- Pion expectation: $n\sigma_\pi$
- Transverse momentum p_T
- Pseudo-rapidity η

In total 2×5 variables are used as input for the training of the decision tree. Since the analysis of the inclusive J/ψ is performed in p_T bins and the same bins are used for the non-prompt J/ψ analysis, an independent BDT is trained in each of the intervals $[1.3, 3]$ GeV/c, $[3., 5.]$ GeV/c and $[5, 10]$ GeV/c. The distributions of the signal from MC J/ψ and the background from side-band data is shown for the input variables in the $[1.3, 3]$ GeV/c p_T bin in Fig. 33. The distributions for the other two bins are shown in Appendix A. The parameters used for the configuration of the BDT uses the standard values that are described in [67]. The obtained classifiers for each p_T bin can be seen in Fig. 34.

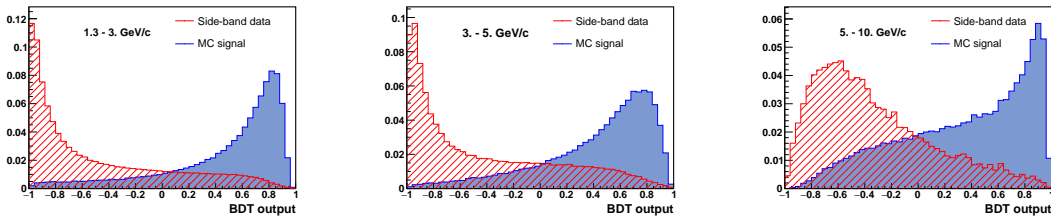
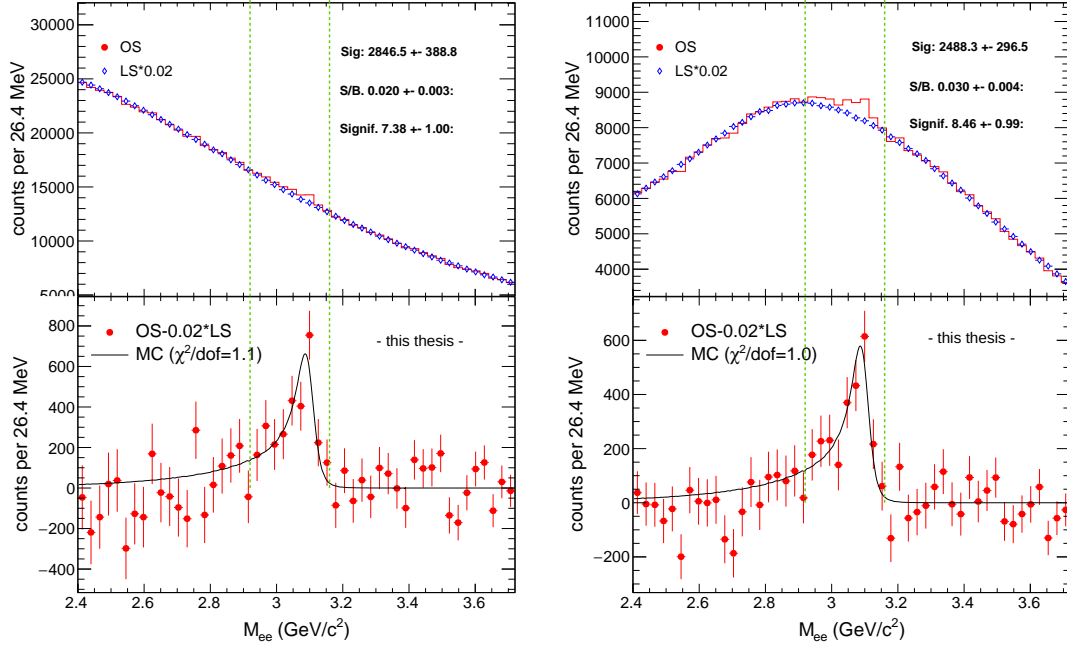


Figure 34: BDT output for the three p_T bins.

It can be seen that the discrimination of the final classifier is much stronger than for the single variables plotted in Fig. 29. No overtraining was observed in the test sample. Additional figures related to the training of the decision tree can be found in Appendix A. It is important to note that in the scope of this thesis the training of the BDT was done on top of the selections used for the inclusive J/ψ analysis. This means that making a selection on the obtained classifiers will reduce the J/ψ raw yield. In general the selections of the inclusive J/ψ analysis should be released, such that as few J/ψ as possible are rejected prior to a selection on the BDT classifier.

4.2.3. Performance of the BDT

In order to quantify the performance of the BDT, for each selected electron-positron pair in the data sample one BDT classifier value is calculated based on the training with the side-band pairs and the J/ψ from MC. Thus the BDT classifier is simply one additional variable for the electron-positron pair. The signal to background (S/B) and the significance ($S/\sqrt{S+B}$) after a selection on the



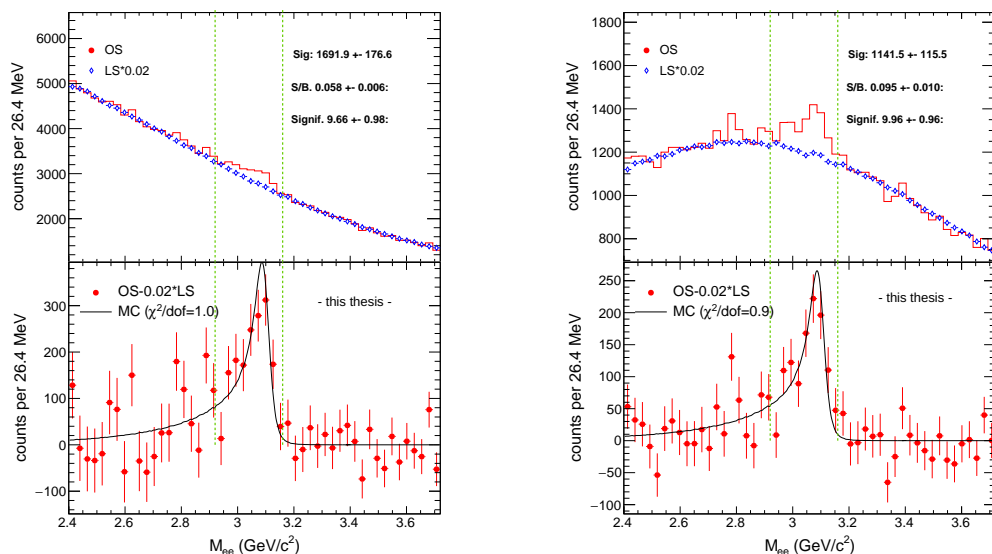
(a) Signal extraction using the event mixing method for the p_T bin [1.3, 3] GeV/c in the centrality class 0-20 %. Only the standard selections are applied. (b) Signal extraction using the event mixing method for the p_T bin [1.3, 3] GeV/c in the centrality class 0-20 %. In addition values of the BDT classifier above 0. is are selected.

Figure 35

classifier value is compared to the S/B and significance obtained with the standard selections used in the inclusive analysis. Thus at this level the evaluation of the performance is independent from the Monte-Carlo simulation. An example for the effect of the application of a selection on the BDT classifier is shown in Fig. 35a and Fig. 35b, where the signal extraction is shown for the p_T bin [1.3, 3] GeV/c in the centrality class 0-20 %. The signal window is always $2.92 \text{ GeV} < M_{ee} < 3.16 \text{ GeV}$ and event mixing, as described in chapter 4.1.3, is used for the background description. The signal shape is taken from reconstructed J/ψ in Monte-Carlo after applying the same selections as in data. In Fig. 35a the signal extraction is shown for the standard selections used in the inclusive J/ψ analysis. In Fig. 35b the signal extraction in the same centrality and p_T interval is shown with an additional selection on the BDT classifier of values above 0. The selection on the BDT classifier changes the shape of the invariant mass spectra. This is expected since electron and positron tracks with higher transverse momentum and proton expectation $n\sigma_p$ (which is correlated with the transverse momentum) have a higher probability to be signal-like, as shown in Fig. 33. The invariant mass is calculated as:

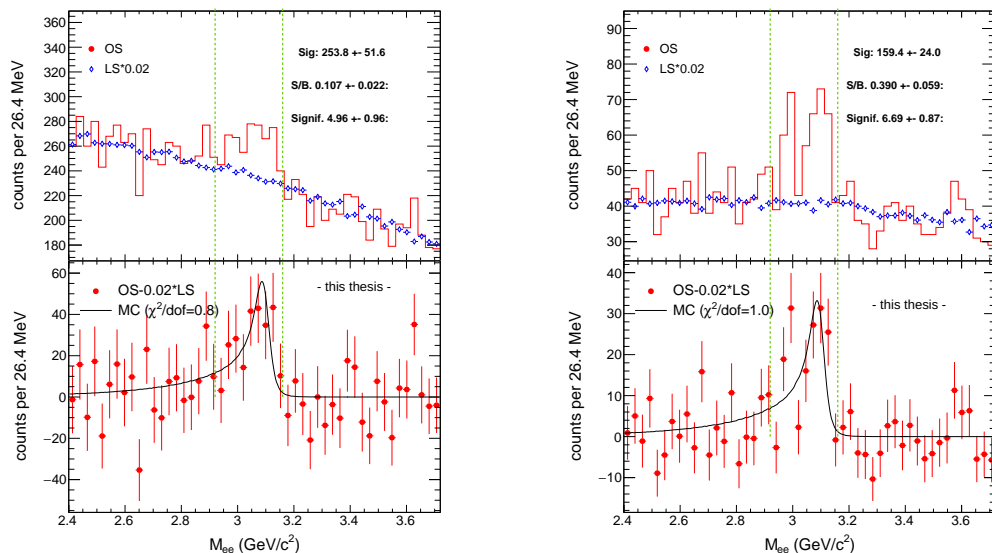
$$m_{e^+e^-} = \sqrt{2p_{T1}p_{T2}(\cosh(\eta_1 - \eta_2) - \cos(\phi_1 - \phi_2))} \quad (26)$$

This shows that for tracks with higher transverse momenta the calculation of the invariant mass results in larger values. Therefore in particular electron-positron pairs with small invariant mass values are rejected by the selection. In Fig. 36 and Fig. 37 the change of the invariant mass spectra after applying a selection on the



- (a) Signal extraction using the event mixing method for the p_T bin [3, 5] GeV/c in the centrality class 0-20 %. Only the standard selections are applied. (b) Signal extraction using the event mixing method for the p_T bin [3, 5] GeV/c in the centrality class 0-20 %. In addition values of the BDT classifier above 0. is are selected.

Figure 36



- (a) Signal extraction using the event mixing method for the p_T bin [5, 10] GeV/c in the centrality class 0-20 %. Only the standard selections are applied. (b) Signal extraction using the event mixing method for the p_T bin [5, 10] GeV/c in the class interval 0-20 %. In addition values of the BDT classifier above 0. is are selected.

Figure 37

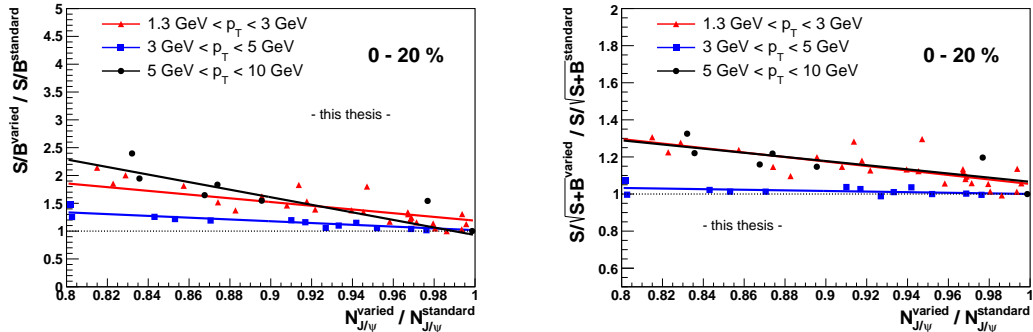
BDT classifier in addition to the standard selections is shown for the $[3, 5]$ GeV/c and $[5, 10]$ GeV/c p_T bin to illustrate the change of the invariant mass spectra.

To quantify the performance of the BDT, the selections on the BDT classifier are varied up to a reduction of the J/ψ raw yield of 20%. A reduction of the raw yield stronger than 20% should be avoided for the inclusive analysis in order to not increase the systematic uncertainties, as shown in the following section, whereas for the non-prompt J/ψ analysis also harder selections can be applied since the average acceptance times efficiencies of the prompt and non-prompt fractions of the inclusive J/ψ cancel in the final calculation of the beauty fraction. Since the classifiers differ in the three p_T bins, the reduction of the raw yield up to 20% corresponds to a variation of the classifier selection in the intervals shown in Tab. 3.

p_T (GeV/c)	BDT interval
1.3 - 3	[-1, 0.3]
3 - 5	[-1, -0.1]
5 - 10	[-1, -0.3]

Table 3: Intervals of the BDT classifier per p_T bin, where the reduction of the J/ψ raw yield is below 20 %.

The S/B and significance are evaluated for multiple selections on the BDT classifier in the intervals given in Tab. 3. Then the ratio between the values for the S/B and significance obtained with the standard selections used in the inclusive analysis, i.e. the values shown in the left panels of Fig. 35, Fig. 36 and Fig. 37, and the values for the S/B and significance after an additional selection on the BDT classifier is calculated. This is plotted as a function of the fraction of the raw yield $N_{J/\psi}$ in Fig. 38a for the S/B and the significance in Fig. 38b. The J/ψ raw yield decreases from right (1) to left (0.8). Also shown are linear regressions, illustrating the trend of the respective p_T bin. So far no uncertainties are calculated on the points, since the calculation is not straight forward due to correlations of the uncertainties in the shown ratios.



(a) Ratio of the S/B obtained with the standard selections and after an additional selection on the BDT classifier (b) Ratio of the significance obtained with the standard selection and after an additional selection on the BDT classifier

Figure 38

The plots show an improvement of up to a factor 2 for the S/B and up to 30 % improvement in significance for the [1.3, 3] GeV/c and the [5, 10] GeV/c p_T bin and the trends show that the improvements are not just statistical fluctuations in the signal extraction. The improvement of the significance also reflects in the relative uncertainties of the signal, displayed in Fig. 35, Fig. 36 and Fig. 37. However there is practically no improvement for the [3, 5] GeV/c p_T bin. It seems that the discriminating power of the classifier obtained from side-band pairs and the MC J/ψ is overestimated with respect to the true conditions in the analyzed data. The reasons for this were not understood in the scope of this thesis. Careful studies are necessary to better understand the differences between the data and the Monte-Carlo simulation.

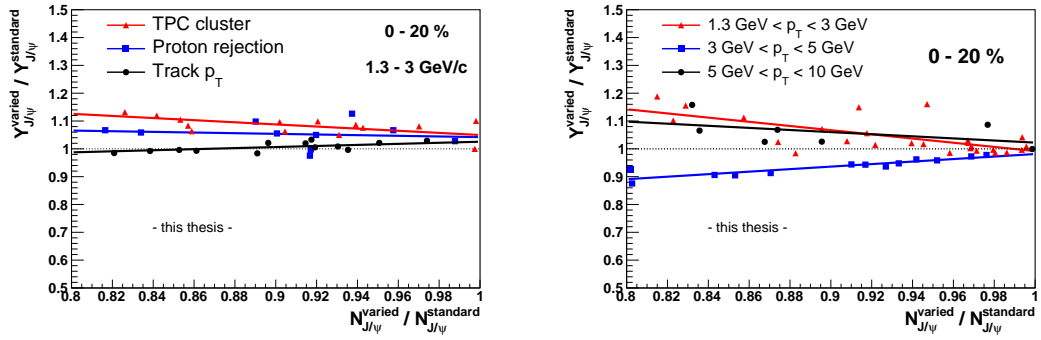
4.2.4. Systematic uncertainties

As mentioned in the previous sections, it is crucial to have a good agreement between MC and data in order to correct the J/ψ raw yield for the acceptance times efficiency with the MC simulation. Applying selections on variables that are not well described in the MC simulation increases the systematic uncertainties. In the inclusive J/ψ analysis the systematic uncertainty calculation is based on the variation of the applied selections. It is important to investigate whether a selection on the BDT classifier can be described in MC simulations, such that the systematic uncertainties do not increase by correcting the J/ψ raw yield for the efficiency times acceptance. Therefore also in the MC simulation a BDT classifier value was calculated for each electron-positron pair. To get an estimation of the systematic effect that a selection has on the corrected yield $Y_{J/\psi}$, the ratio between the corrected yield with a varied selection and the corrected yield with the standard selections of the inclusive J/ψ analysis is calculated:

$$\frac{Y_{J/\psi}^{varied}}{Y_{J/\psi}^{Standard}} = \frac{N_{J/\psi}^{Pb-Pb,varied}}{N_{J/\psi}^{Pb-Pb,standard}} \times \frac{\langle \mathcal{A} \times \mathcal{E} \rangle^{standard}}{\langle \mathcal{A} \times \mathcal{E} \rangle^{varied}} \quad (27)$$

In the ideal case this ratio gives unity. To get an impression of the magnitude of the deviations from unity, the ratio of the corrected yields for some variables used in the inclusive J/ψ analysis is shown. Here no selection on the BDT classifier is applied. For each selection the ratio of the corrected yields is plotted against the reduction of the J/ψ raw yield. The TPC clusters are varied up to 135 cluster, the $n\sigma_p$ is varied from 3.5 to 4.5 and the track p_T is varied from 1 GeV/c to 1.25 GeV/c. The ratio of the corrected yields is shown in Fig. 39a for the [1.3, 3] GeV/c p_T bin for harder selections on the TPC cluster, proton expectation $n\sigma_p$ and the track momentum as a function of the J/ψ raw yield up to a reduction of 20%. It can be seen that the deviation in the corrected yields can reach up to 10%. These variations are the base to calculate the systematic uncertainties on the signal reconstruction and extraction, as described in chapter 4.1.4, although it is not obvious how to estimate the systematic uncertainties from the variations.

To make a comparison, the selections on the BDT classifier are varied in the intervals given in Tab. 3, again reducing the J/ψ raw yield by up to 20 %. The results for the centrality class 0 - 20 % is shown in Fig. 39b. The comparison shows that the deviations from the corrected yield obtained with the standard selections



(a) Ratio of the corrected yield obtained with the standard selections for the inclusive analysis and after harder selections on the TPC cluster, $n\sigma_p$ and track momentum for the [1.3, 3] GeV/c p_T bin. (b) Ratio of the corrected yield obtained with the standard selections for the inclusive analysis and after harder selections on the BDT classifier for the analyzed p_T bins.

Figure 39

of the inclusive J/ψ analysis have a similar magnitude for variations of variables used in the inclusive analysis as for variations of the additional BDT classifier selection. This indicates that the systematic uncertainties will not increase much by applying selections on a BDT classifier. Again the [3, 5] GeV/c p_T bin behaves differently which is not fully understood yet. It is important to note that these considerations are a first study to investigate whether it is possible to describe the selection on a classifier in the MC simulation. Since the selection on the classifier is applied on top of the standard selections used in the inclusive analysis, it is only possible to make harder selections that reduce the J/ψ raw yield. For a more complete study the standard selections of the inclusive J/ψ analysis have to be released, such that also variations where the J/ψ raw yield is larger than the raw yield obtained with the standard selections of the inclusive J/ψ analysis can be considered.

4.2.5. Conclusions and outlook

The first studies of the use of TMVA methods have shown that it is possible to improve the significance and reduce the background for the low p_T bin [1.3, 3] GeV/c and the high p_T bin [5, 10] GeV/c. Considering that doubling the statistics and keeping the same S/B ratio per event, the significance improves with $\sqrt{2}$, an improvement of a factor of 1.3 for the significance is considered as a first success. A first study has indicated that it will be possible to describe the selection on a BDT classifier in Monte-Carlo simulations in order to correct the measured J/ψ raw yield without greatly increasing the systematic uncertainties. In the future the selection of the variables has to be revised, in order to find the optimal setup of variables to improve the significance, while not increasing the systematic uncertainties. In addition different methods, such as neural networks and support vector machines should be tried to optimize the performance, as well as a tuning of the parameters of the respective MVA method. The standard selections of

the inclusive J/ψ analysis have to be released in order to keep more J/ψ prior to applying selections on a MVA classifier. Studies are needed to better understand the differences between data and MC. To reduce the systematic uncertainties, a tuning of the MC to data should be considered. In addition a minimum-bias MC obtained from dedicated fast simulations could improve the performance. With respect to the following non-prompt J/ψ analysis it is concluded that the S/B of the invariant mass spectra can be improved, however the S/B conditions still are highly challenging, in particular at low transverse momentum.

4.3. Extraction of the non-prompt J/ψ fraction

4.3.1. Analysis method

To determine the fraction of J/ψ coming from beauty decays, a 2-dimensional fit to the invariant mass spectra and to a variable that discriminates prompt and non-prompt J/ψ is performed. In this analysis the pseudo-proper decay length, first employed by CDF [68] is used as discriminating variable. The pseudo-proper decay length is defined as:

$$x = \frac{L_{xy} \cdot M^{J/\psi} \cdot c}{p_T^{J/\psi}} \quad (28)$$

where L_{xy} is defined as:

$$L_{xy} = \frac{\vec{L} \cdot \vec{p}_T^{J/\psi}}{p_T^{J/\psi}} \quad (29)$$

where \vec{L} is the vector between the primary vertex and the decay vertex of the J/ψ, i.e. L_{xy} is the projection of the J/ψ flight distance onto its transverse momentum vector $\vec{p}_T^{J/\psi}$. $M^{J/\psi}$ is the world average J/ψ mass of 3.096 GeV/c² [2]. The decay vertex of the electron-positron pairs is obtained using the KF vertexing package [69]. The vertex is fitted taking into account the track parameters and their covariance matrices using an optimized Kalman filter algorithm. Since the prompt J/ψ decay almost immediately, the distribution of the pseudo-proper decay length depends on the resolutions of the primary vertex and the secondary vertex. The non-prompt J/ψ originate from a beauty hadron, therefore their pseudo-proper decay length distribution mimics the average proper decay length of the distribution of beauty hadrons.

The 2-dimensional fit is realized by an unbinned log-likelihood fit, maximizing the quantity:

$$\ln(\mathcal{L}) = \sum_{i=1}^N \ln L(m_{e^+e^-}^i; x^i) \quad (30)$$

where N is the total number of candidates in the invariant mass interval considered for the fit, x the pseudo-proper decay length and $m_{e^+e^-}$ the invariant mass of the electron-positron pairs. The likelihood function $L(m_{e^+e^-}^i; x^i)$ describes the probability of observing a J/ψ candidate with given values of $m_{e^+e^-}$ and x , and is defined as:

$$L = N_{Sig} \times ((1 - f_B)F_{Prompt}(x) + f_B F_B(x)) \times M_{Sig}(m_{e^+e^-}) + N_{Bkg} \times F_{Bkg}(x) \times M_{Bkg}(m_{e^+e^-}) \quad (31)$$

The free parameters of the fit are the number of signal events N_{Sig} , background events N_{Bkg} and the fraction of J/ψ's coming from B-decays f_B defined as:

$$f_B = \frac{N_{J/\psi \leftarrow B}}{N_{J/\psi \leftarrow B} + N_{prompt J/\psi}} \quad (32)$$

An extended fit is used, which means the sum of N_{Sig} and N_{Bkg} has to be equal to the total number of events in the respective data sample, which provides an

additional constraint. $F_{Prompt}(x)$ and $F_{Bkg}(x)$ are the Probability Density Functions (PDFs) for the prompt and non-prompt J/ψ pseudo-proper decay length distributions obtained from a Monte-Carlo simulation. $F_{Bkg}(x)$ is the template for the pseudo-proper decay length PDF of the background, which is obtained from the pseudo-proper decay length distribution of electron-positron pairs lying in the side-bands of the invariant mass spectra. $M_{Bkg}(m_{e^+e^-})$ and $M_{Sig}(m_{e^+e^-})$ are the PDFs of the background and the signal of the invariant mass spectra respectively, where $M_{Bkg}(m_{e^+e^-})$ is obtained from data using the event mixing method and $M_{Sig}(m_{e^+e^-})$ is obtained from MC.

The beauty fraction f_B is extracted in bins shown in Table 4. To improve the signal to background ratio, a selection on the BDT classifier explained in the previous chapter is applied. The values of the selections are summarized in section 4.3.3.

Table 4: Bins in centrality and transverse momentum used in the analysis.

Centrality (%)	p_T (GeV/c)
0-40	1.3 - 3
0-40	3 - 5
0-40	5 - 10
0-20	3 - 5
20-40	3 - 5
40-90	3 - 5

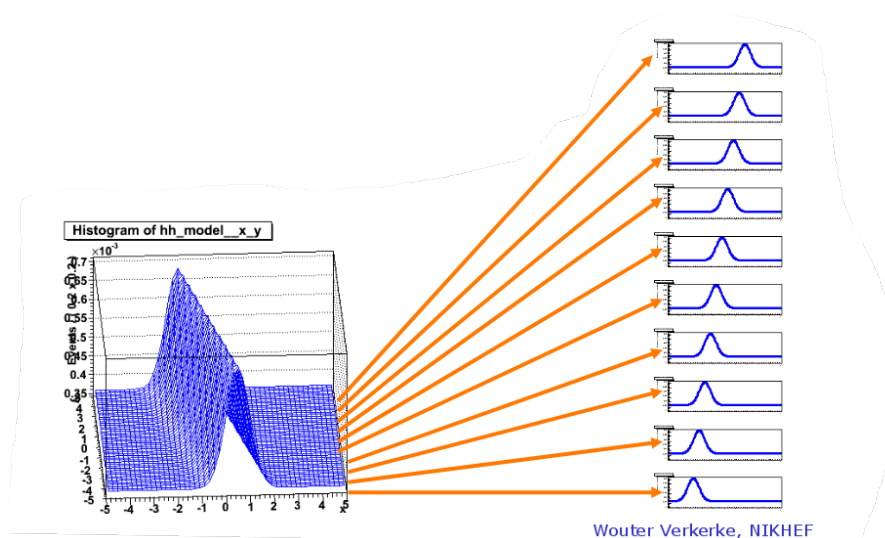


Figure 40: Toy model to illustrate the idea of a simultaneous fit. The distribution of x varies slightly with y . The datasample is split in 10 subsamples and a simultaneous Gaussian fit is performed requiring the same value for the Gaussian width in each subsample, whereas the mean value can be different. This increases the statistical sensitivity [70].

A method to stabilize the 2-d fit and gain statistical sensitivity is the use of simultaneous fits [71]. This method uses the splitting of a dataset D in subsets D_i , where (slightly) varying properties can be described by individually adjusted probability density functions which increases the statistical sensitivity. The general idea of a simultaneous fit is illustrated in a toy example [70] in Fig. 40. Given

a dataset $D(x, y)$ where the variable of interest is x and the Gaussian distribution of x varies slightly with y . Assuming that only the Gaussian width is of interest which is supposed to be invariant under y , one can slice the dataset in multiple bins of y , in this example 10, and simultaneously fit each bin with a PDF that has a different Gaussian mean parameter, but the same Gaussian width in all bins. Consequently the fit returns 10 different values for the different mean values, but only one value for the width, that is common for all 10 subsets.

In this analysis this technique is used, where the role of the width is taken by the beauty fraction f_B , while the signal and background events in each subset can be different, as was the mean in the preceding toy model. The electron-positron pairs are split up in two categories according to their hits in the first two layers of the ITS (SPD hits). The first category consists of pairs, where both, electron and positron tracks have 2 hits in the first two layers, whereas the second category consists of pairs where at least one of the tracks has only one hit in the SPD. The resolutions of the tracks that have two hits in the SPD are higher than the ones that only have one hit. Therefore it is expected that the vertex fitted from tracks in the first category has a higher resolution and consequently it is expected that also the resolution of the pseudo-proper decay length is higher. The first category is referred to as BB , while the second category is referred to as BS . Moreover the first three bins in Table 4 are further split in centrality into samples from 0 – 20% and 20 – 40%. This makes it possible to use individually adjusted PDFs for the description of the invariant mass background and the pseudo-proper decay length background depending on the centrality class. Using the technique of simultaneous fits, the log-likelihood function defined in equation 30 then becomes:

$$\ln(\mathcal{L}) = \sum_{i=1}^N \sum_{\text{subsample}=1}^M \ln L^{\text{sim}}(m_{e^+e^-}^{i,\text{subsample}}; x^{i,\text{subsample}}) \quad (33)$$

where M is the total number of subsamples for the simultaneous fit. In the scope of this thesis the log-likelihood function was implemented in the framework of RooFit [71].

The measured value for f_B has to be corrected for different acceptance and reconstruction efficiencies $\langle \mathcal{A} \times \mathcal{E} \rangle$ for prompt and non-prompt J/ ψ .

In particular $\langle \mathcal{A} \times \mathcal{E} \rangle$ depends on the p_T of the J/ ψ and the p_T distributions of prompt and non-prompt J/ ψ 's are different. The corrected fraction of non-prompt J/ ψ can be obtained as

$$f_B^{\text{corr}} = \left(1 + \frac{1 - f_B}{f_B} \frac{\langle \mathcal{A} \times \mathcal{E} \rangle_B}{\langle \mathcal{A} \times \mathcal{E} \rangle_{\text{prompt}}} \right)^{-1} \quad (34)$$

where $\langle \mathcal{A} \times \mathcal{E} \rangle_B$ and $\langle \mathcal{A} \times \mathcal{E} \rangle_{\text{prompt}}$ are the average acceptance times efficiencies in the respective p_T interval. Nevertheless, this correction is expected to be small, since the difference in the p_T spectra in the chosen p_T bins is small and the selection criteria are tuned to not treat prompt and non-prompt J/ ψ differently.

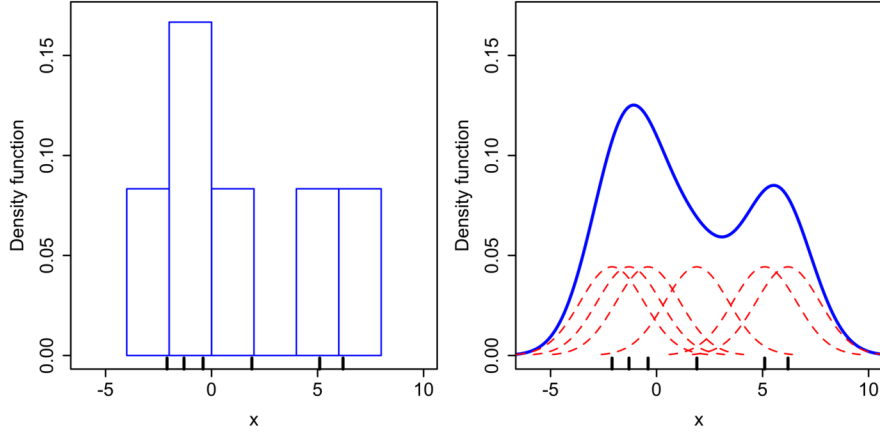


Figure 41: Example for a density estimation with a histogram and a Gaussian kernel density estimation using the same input data [72].

4.3.2. Templates for the fit

In this analysis the probability density functions (PDFs) for the background, prompt and non-prompt J/ψ pseudo-proper decay length are directly interpolated from unbinned distributions using a density estimation approach to obtain the shapes without explicit parametrization. This avoids the complications of obtaining the resolution function needed for the approach employed by CDF [68]. The most simple density estimations are histograms. However it was seen that the PDFs obtained with simple histograms are not suitable for the log-likelihood fit described in the previous section due to the dependence on the binning and the problem of having bins with zero entries. Thus a so-called kernel density estimation approach was used for the interpolation. Kernel density estimates are closely related to histograms, but in addition properties such as smoothness or continuity, can be controlled by using a suitable kernel [73]. Mathematically, a kernel is a positive function $K(x; h)$ which depends on the bandwidth parameter h . For a given kernel form, the density estimate at a point y within a group of points $x_i; i = 1 \cdots N$ is given by:

$$\rho_K(y) = \sum_{i=1}^N K((y - x_i)/h) \quad (35)$$

The bandwidth acts as a smoothing parameter. A large bandwidth leads to a very smooth density distribution, while a small bandwidth leads to a fluctuating density distribution. The bandwidth exhibits a strong influence on the resulting estimate. Often a Gaussian Kernel is used, where K has the form:

$$K(x; h) \propto \exp\left(-\frac{x^2}{2h^2}\right) \quad (36)$$

An example for a density estimation with a histogram and a Gaussian kernels is shown in Fig. 41. The Gaussian kernel density estimate, in which each point contributes a Gaussian curve to the total, results in a smooth density estimate modeling the distribution of data points.

Roofit provides the kernel estimation class `RooKeysPdf`, which gives a PDF that represents the shape of an external unbinned dataset as a superposition of Gaussians with equal surface, but with varying width, depending on the local event density [71]. The width of the Gaussian is adaptively calculated from the local density of events, i.e. narrow for regions with high event density to preserve details and wide for regions with low event density to promote smoothness. The details of the general algorithm are described elsewhere [74].

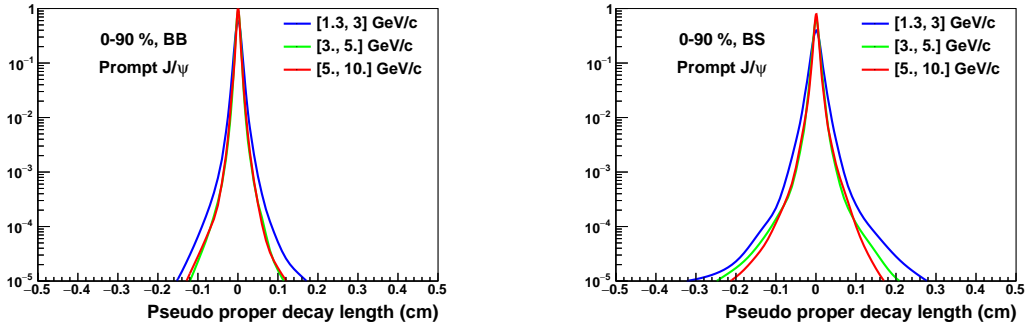


Figure 42: Templates for the prompt J/ψ PDFs in the three p_T bins for two categories BB (left panel) and BS (right panel) as explained in the text.

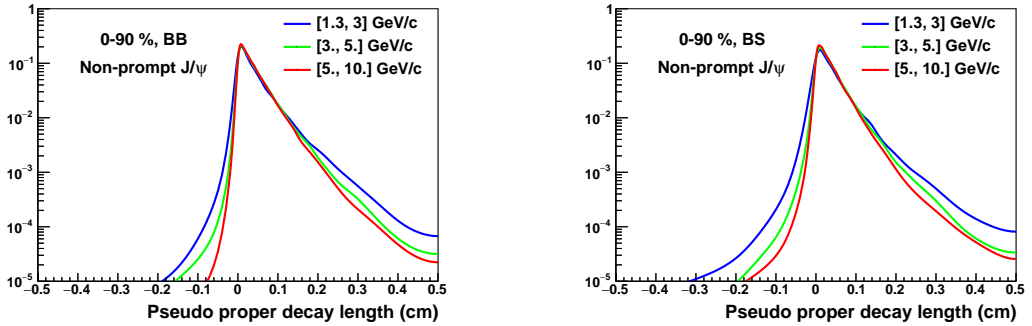


Figure 43: Templates for the non-prompt J/ψ PDFs in the three p_T bins for two categories BB (left panel) and BS (right panel) as explained in the text.

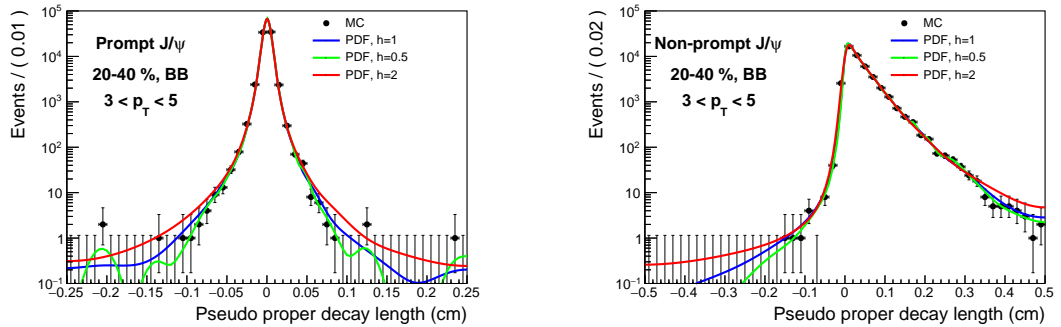


Figure 44: Example for the variation of the bandwidth parameter h for the density estimation for the prompt (left panel) and non-prompt (right panel) J/ψ for the $[3, 5]$ GeV/c p_T bin in the 20 – 40% centrality class.

For the templates of the prompt and non-prompt J/ψ , the PDFs are estimated from the (unbinned) reconstructed Monte-Carlo distributions after applying the selections described in chapter 4.1. Different templates are used for the three p_T bins in the two categories defined by the hits in the SPD, BB and BS as explained above. No centrality dependence is assumed. The distributions for the prompt templates is shown in Fig. 42 and for the non-prompt templates in Fig. 43. It can be seen that the pseudo-proper decay length templates are narrower for higher p_T bins, which is expected since the resolution of the tracks improves for higher momenta. The PDFs for the BS category are wider, due to inferior resolution compared to the BB category.

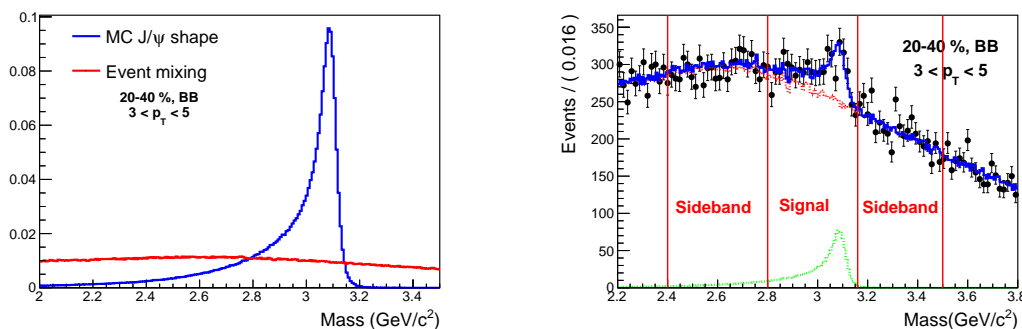


Figure 45: Left panel: PDF for the invariant mass shape and for the background from event mixing in the $[3, 5]$ GeV/c p_T bin in the 20 – 40% centrality class. Right panel: example for the definition of the side-bands in the $[3, 5]$ GeV/c p_T bin in the 20 – 40% centrality class. The side-bands are chosen from 2.4 - 2.8 GeV/c^2 and from 3.16 to 3.5 GeV/c^2 .

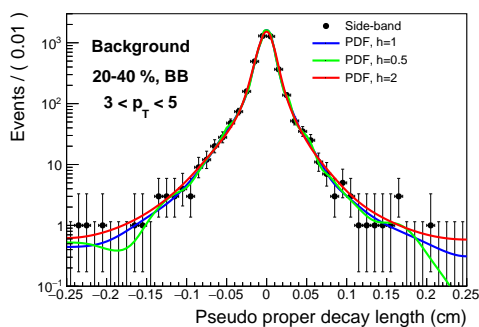


Figure 46: Example for the variation of the bandwidth parameter h for the PDF of the pseudo-proper decay length background template in the $[3, 5]$ GeV/c p_T bin. The side-bands are chosen from 2.4 - 2.8 GeV/c^2 and from 3.16 - 3.5 GeV/c^2 and are shown in Fig. 45.

As described above, the density estimation of the templates depends on the bandwidth parameter h . In Fig. 44 an example of the density estimation with different values of h is shown in the $[3, 5]$ GeV/c p_T bin for the BB category. The standard value of h is 1 (blue curves). Increasing the value of h (red curve) gives a smoother estimation, while decreasing h (green curve) leads to an estimation that depends stronger on the fluctuations. Since variations of h lead to different shapes they are

considered in the estimation of the systematic uncertainties. It is a clear drawback of the non-parametric estimation that the description of the tails depends strongly on h .

The template for the pseudo-proper decay length background is estimated from the pseudo-proper decay length of electron-positron pairs that lie in the side-bands of the J/ψ invariant mass spectra in the respective p_T , centrality and category bin. Thus it is assumed that the distribution of the pseudo-proper decay length for these pairs describes the pseudo-proper decay length of the background.

Table 5: Side-band limits for the pseudo-proper decay length background

p_T (GeV/c)	lower side-band limit (GeV/c ²)	upper side-band limit (GeV/c ²)
1.3 - 3	2.55 - 2.9	3.16 - 3.35
3 - 5	2.4 - 2.8	3.16 - 3.5
5 - 10	2.4 - 2.8	3.16 - 3.5

The side-band limits are shown in Table 5. An example for the definition of the side-bands for the [3, 5] GeV/c p_T is shown in Fig. 45 on the right. Due to the small S/B of the lowest p_T bin the side-bands are chosen narrower and closer to the signal peak. The resulting template for the pseudo-proper decay length background is shown in Fig. 46, again for different values of the bandwidth parameter h . The choice of the limits will be varied for the systematic uncertainties.

The J/ψ signal shape is taken from the reconstructed MC J/ψ and no dependencies on centrality or p_T is assumed. The background template for the invariant mass distributions is obtained using the event mixing technique, as described in chapter 4.1. The background of the invariant mass spectra depends on the centrality, p_T and the category defined by the hits in the SPD, BB and BS . The left panel of Fig. 45 shows the PDF for the J/ψ signal shape and the background from event mixing in the 20 – 40% centrality class for the BB category.

4.3.3. Fit results

Table 6: Standard parameters for the log-likelihood fit in the three p_T bins

Type	[1.3, 3] GeV/c	[3., 5.], [5., 10.] GeV/c
Mass window (GeV/c^2)	2.55 - 3.35	2.4 - 3.5
Side-band limits low (GeV/c^2)	2.55 - 2.9	2.4 - 2.8
Side-band limits high (GeV/c^2)	3.16 - 3.35	3.16 - 3.5
Decay length range (cm)	0.8	0.15
Bandwidth h	1.	1.
BDT classifier	> .3	> -0.1

In Table 6 the parameters used for the mass window, the side-bands for the background, the fit range of the pseudo-proper decay length, the value for the bandwidth h of the density estimation and the selection on the BDT classifier in the respective p_T bins are summarized. As discussed in the previous section, the small S/B in the lowest p_T bin makes it necessary to use different parameters, whereas for the remaining p_T bins the same parameters are used. The choice of these parameters will be referred to as "standard parameters".

Table 7: Results for f_B from the log-likelihood fit

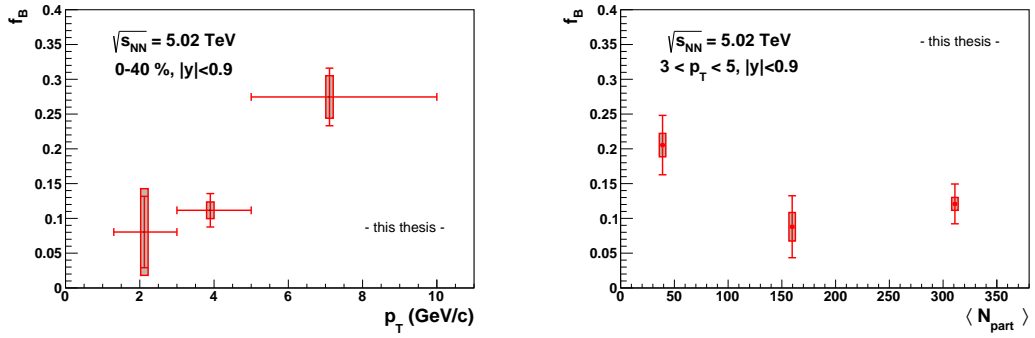
Centrality (%)	p_T (GeV/c)	f_B
0-40	1.3 - 3	$0.080 \pm 0.051(stat.) \pm 0.062(sys.)$ (Fig. 49)
0-40	3 - 5	$0.111 \pm 0.024(stat.) \pm 0.012(sys.)$ (Fig. 50)
0-40	5 - 10	$0.274 \pm 0.041(stat.) \pm 0.030(sys.)$ (Fig. 51)
0-20	3 - 5	$0.121 \pm 0.029(stat.) \pm 0.009(sys.)$ (Fig. 52)
20-40	3 - 5	$0.088 \pm 0.045(stat.) \pm 0.020(sys.)$ (Fig. 53)
40-90	3 - 5	$0.205 \pm 0.043(stat.) \pm 0.01(sys.)$ (Fig. 54)

The results of the fit are summarized in Table 7. Both the statistical and systematic uncertainties are quoted. The estimation of the systematic uncertainties is explained in section 4.3.5.

The final fits to the data in the respective p_T bins and centrality classes are shown in Fig. 49 - Fig. 54. The PDFs for the pseudo-proper decay length are projected on the mass window 2.92 - 3.16 GeV/c^2 . It should be noticed that the shown log-likelihoods are the sum of the PDFs of the simultaneous fit, described in the previous sections. The PDFs projected on the subsamples for the simultaneous fit are shown in Appendix B.

The final measured values are shown as a function of p_T in Fig. 47a for the 0-40% centrality class and as a function of centrality in Fig. 47b in the [3, 5] GeV/c p_T interval, where centrality is expressed as $\langle N_{part} \rangle$. Within uncertainties no centrality dependence is observed. The horizontal bars of the p_T values for the measured f_B values in Fig. 47a symbolize the width of the p_T bin. The mean p_T in each bin has been evaluated for the inclusive J/ψ from the MC simulation, in order to set the position of the measured point.

In Fig. 48 the measured f_B values are shown as a function of p_T compared to measurements by ALICE in Pb-Pb at $\sqrt{s_{NN}} = 2.76$ TeV [49], ATLAS in pp at



(a) Values of f_B determined in this analysis at $\sqrt{s_{NN}} = 5.02$ TeV in the 0-40% centrality class as a function of p_T . (b) Values of f_B determined in this analysis at $\sqrt{s_{NN}} = 5.02$ TeV in the 0-40% centrality class as a function of centrality.

Figure 47

$\sqrt{s} = 7$ TeV [75] and CMS in pp at $\sqrt{s} = 7$ TeV [76]. The statistical and systematic uncertainties are added in quadrature. A similar p_T dependence as in the previous measurements is observed, within uncertainties the values are in agreement. Compared to the previous measurement by ALICE at $\sqrt{s_{NN}} = 2.76$ TeV three bins are shown and the uncertainties are slightly decreased for the two higher p_T bins.

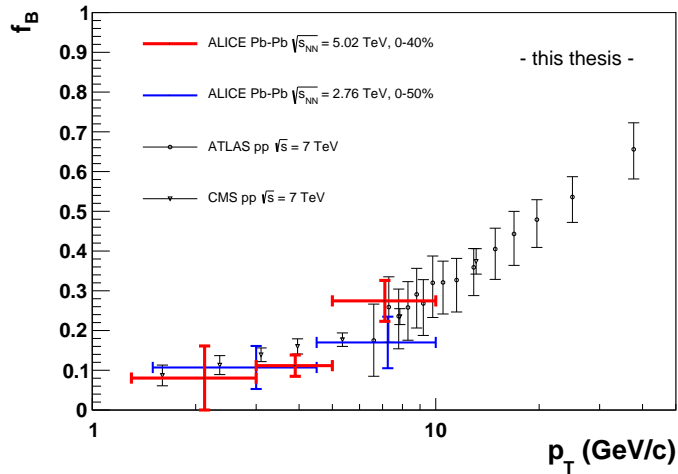


Figure 48: Comparison of f_B determined in this analysis with the measured non-prompt J/ ψ fraction in ALICE in Pb-Pb at $\sqrt{s_{NN}} = 2.76$ TeV [49], ATLAS in pp at $\sqrt{s} = 7$ TeV [75] and CMS in pp at $\sqrt{s} = 7$ TeV [76]. The systematic and statistic uncertainties are added in quadrature.

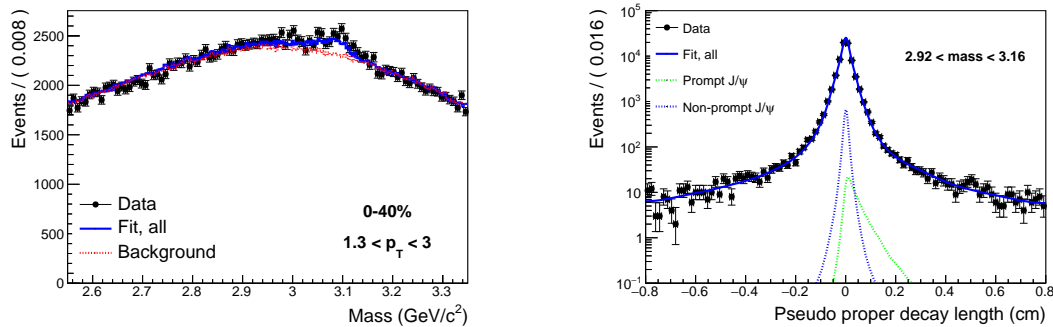


Figure 49: The invariant mass (left panel) and pseudo-proper decay length (right panel) distributions for e^+e^- pairs in the p_T bin $[1.3, 3]$ GeV/c in Pb-Pb collisions in the centrality class 0-40% at $\sqrt{s_{NN}} = 5.02$ TeV. The projections of the maximum likelihood fit used to extract f_B are superimposed to the data. The projections on the subsamples are shown in Appendix B in Fig. 75.

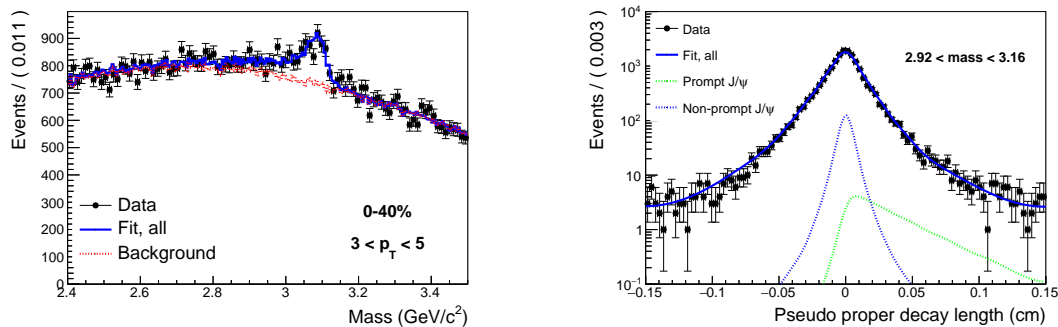


Figure 50: The invariant mass (left panel) and pseudo-proper decay length (right panel) distributions for e^+e^- pairs in the p_T bin $[3, 5]$ GeV/c in Pb-Pb collisions in the centrality class 0-40% at $\sqrt{s_{NN}} = 5.02$ TeV. The projections of the maximum likelihood fit used to extract f_B are superimposed to the data. The projections on the subsamples are shown in Appendix B in Fig. 76.

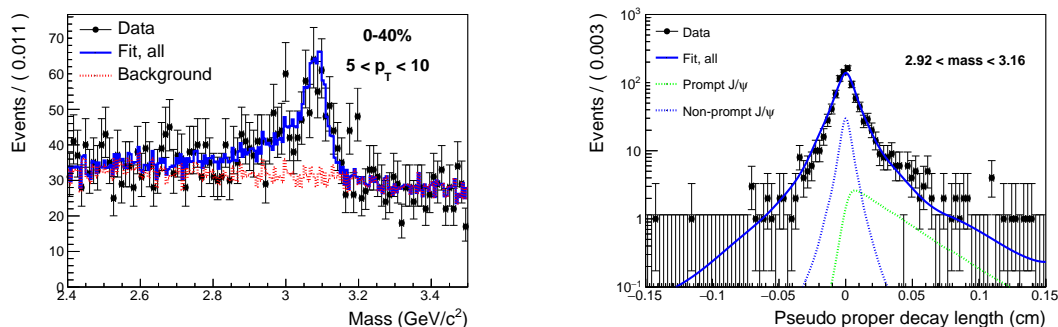


Figure 51: The invariant mass (left panel) and pseudo-proper decay length (right panel) distributions for e^+e^- pairs in the p_T bin $[5, 10]$ GeV/c in Pb-Pb collisions in the centrality class 0-40% at $\sqrt{s_{NN}} = 5.02$ TeV. The projections of the maximum likelihood fit used to extract f_B are superimposed to the data. The projections on the subsamples are shown in Appendix B in Fig. 77.

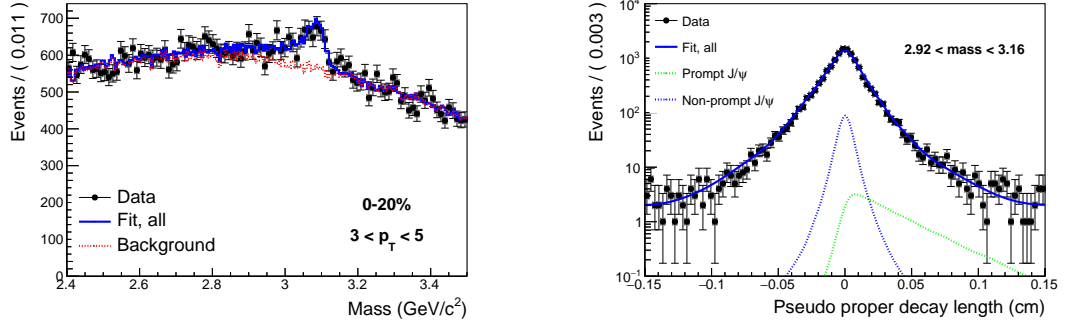


Figure 52: The invariant mass (left panel) and pseudo-proper decay length (right panel) distributions for e^+e^- pairs in the p_T bin $[3, 5]$ GeV/c in Pb-Pb collisions in the centrality class 0-20% at $\sqrt{s_{NN}} = 5.02$ TeV. The projections of the maximum likelihood fit used to extract f_B are superimposed to the data. The projections on the subsamples are shown in Appendix B in Fig. 72.

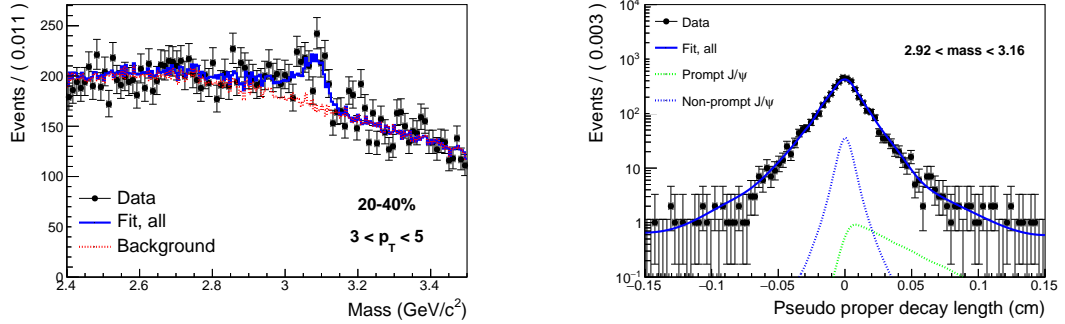


Figure 53: The invariant mass (left panel) and pseudo-proper decay length (right panel) distributions for e^+e^- pairs in the p_T bin $[3, 5]$ GeV/c in Pb-Pb collisions in the centrality class 20-40% at $\sqrt{s_{NN}} = 5.02$ TeV. The projections of the maximum likelihood fit used to extract f_B are superimposed to the data. The projections on the subsamples are shown in Appendix B in Fig. 73.

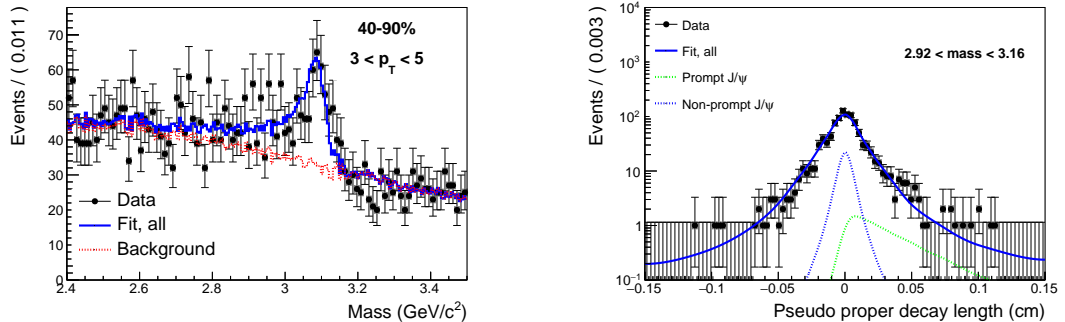


Figure 54: The invariant mass (left panel) and pseudo-proper decay length (right panel) distributions for e^+e^- pairs in the p_T bin $[3, 5]$ GeV/c in Pb-Pb collisions in the centrality class 40-90% at $\sqrt{s_{NN}} = 5.02$ TeV. The projections of the maximum likelihood fit used to extract f_B are superimposed to the data. The projections on the subsamples are shown in Appendix B in Fig. 74.

4.3.4. Acceptance and efficiency corrections

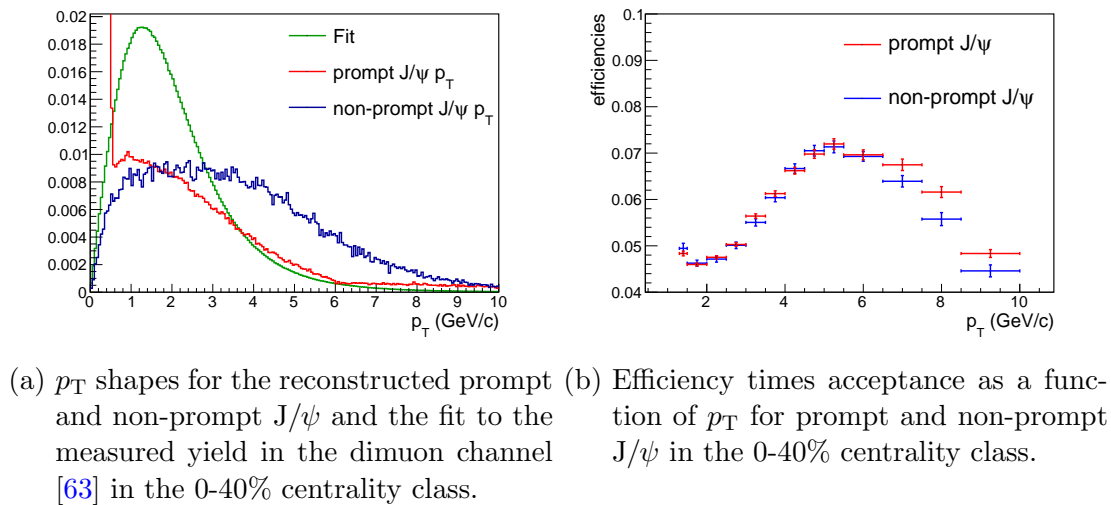
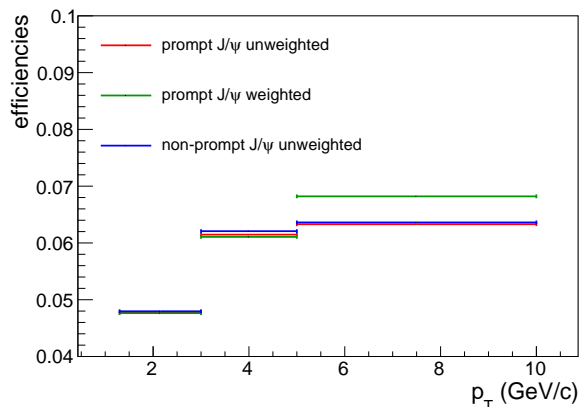


Figure 55

Figure 56: Reweighted efficiencies times acceptance for the prompt J/ψ component in the three p_T bins in comparison to the unweighted non-prompt J/ψ efficiency times acceptance in the 0-40% centrality class.

The correction factor $R = \frac{\langle A \times \mathcal{E} \rangle_B}{\langle A \times \mathcal{E} \rangle_{prompt}}$ defined in equation 34 depends solely on the acceptance times efficiencies for the prompt and non-prompt J/ψ in the respective p_T bin and centrality class. The acceptance times efficiency of both components depends on the p_T of the J/ψ . As described in chapter 4.1, the input p_T distribution of the MC simulation is unnatural, since artificial p_T spectra were generated for high and low p_T in the MC simulation (Fig. 25). The p_T shapes for the reconstructed MC prompt J/ψ and non-prompt J/ψ are shown in Fig. 55a. Due to the unnatural shapes, a reweighting needs to be applied. In the inclusive J/ψ analysis the acceptance times efficiency is reweighted to the measured yield in the dimuon channel by ALICE at forward rapidity [63]. The cross sections for different

centralities are fitted with the phenomenological function:

$$f(p_T) = C \times \frac{p_T}{(1 + (\frac{p_T}{p_0})^2)^n} \quad (37)$$

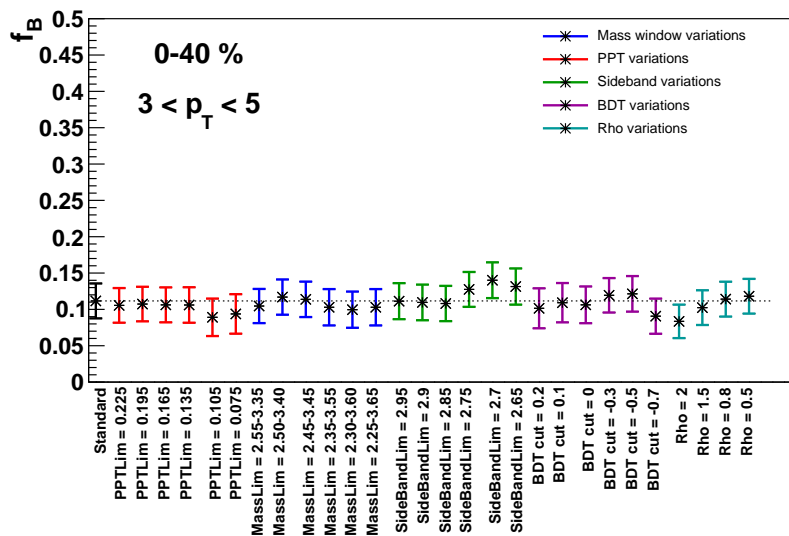
The fit for the 0-40% centrality class is shown in Fig. 55a. The unweighted total efficiencies in small p_T bins are shown in Fig. 55b. The shape of the distributions is mainly due to the PID selections. An attempt was made to reweight the efficiencies in the 0-40% centrality class for the prompt J/ψ component, while leaving the non-prompt J/ψ component unweighted. The formula used for the reweighting is defined as [61]:

$$\langle \mathcal{A} \times \mathcal{E} \rangle = \frac{\int_{p_T^{min}}^{p_T^{max}} (\frac{dN}{dp_T})_{InclusiveJ/\psi}^{\mu+\mu-} \times \Delta(p_T^{J/\psi}) \times eff(p_T^{J/\psi})}{\int_{p_T^{min}}^{p_T^{max}} (\frac{dN}{dp_T})_{InclusiveJ/\psi}^{\mu+\mu-} \times \Delta(p_T^{J/\psi})} \quad (38)$$

where $\Delta(p_T^{J/\psi})$ is the width of the considered p_T bin in Fig. 55b, $(\frac{dN}{dp_T})_{InclusiveJ/\psi}^{\mu+\mu-}$ is the muon p_T spectra and $eff(p_T^{J/\psi})$ the unweighted efficiency in the respective bin.

The result can be seen in Fig. 56. As expected the reweighted efficiencies in the first two p_T bins are similar leading to a small correction factor. However for the [5, 10] GeV/c p_T bin, where the artificial high p_T component is relevant, there is a significant difference in the efficiencies for the prompt and non-prompt J/ψ. This might be caused by the input shapes of the p_T spectra in the MC production that was produced for the purpose of the inclusive J/ψ analysis or the reweighting procedure. Since this large deviation is a contradiction to the results of previous ALICE analysis for the non-prompt J/ψ [77, 78], and the effect of this large difference in the efficiencies for prompt and non-prompt J/ψ cannot be explained, the correction for the acceptance times efficiency is not applied in the scope of this thesis. Sophisticated checks are needed to understand this correction and estimate the systematic uncertainties connected with it. Nevertheless, since in the previous analysis it was found that with proper MC productions and correct reweighting procedures this correction is very small, it is assumed that neglecting this correction will not have a large impact on the final results and it is still justified to calculate the nuclear modification factor of the non-prompt J/ψ with the measured, uncorrected f_B value.

4.3.5. Systematic uncertainties

Figure 57: Variations of the fit parameters for the $[3, 5]$ GeV/ c p_T in the 0-40 % centrality class.

To get a first estimation of the systematic uncertainties, the parameters and limits used in the fit are varied. The parameters are varied in the limits shown in Table 8 for the $[1.3, 3]$ GeV/ c p_T bin and in the limits shown in Table 9 for the $[3, 5]$ GeV/ c and $[5, 10]$ GeV/ c p_T bins. The lower side-band limit is varied to investigate possible effects of including a part of the tail of the J/ψ invariant mass signal in the background template for the pseudo-proper decay length. The fit is then repeated with the varied parameters.

Table 8: Variations for the $[1.3, 3]$ GeV/ c p_T bin.

Type	Std. value	Variations min	Variations max
Mass window (GeV/ c^2)	2.55 - 3.35	2.70 - 3.2	2.4 - 3.5
Side-band limits low (GeV/ c^2)	2.55 - 2.9	2.70 - 2.85	2.4 - 3.05
Decay length range (cm)	0.6	0.72	1.2
Bandwidth h	1.	0.5	2
BDT classifier	> 0.3	> -0.3	> 0.6

Table 9: Variations for the $[3, 5]$ GeV/ c and $[5, 10]$ GeV/ c p_T bin

Type	Std. value	Variations min	Variations max
Mass window	2.4 - 3.5	2.55 - 3.35	2.25 - 3.65
Side-band limits low (GeV/ c^2)	2.4 - 2.8	2.55 - 2.65	2.25 - 2.95
Decay length range (cm)	0.15	0.075	0.225
Bandwidth h	1.	0.5	2
BDT classifier	> -0.1	> -0.7	> 0.2

In Fig. 57 an example for the obtained f_B values after varying the fit parameters in the $[3, 5]$ GeV/c p_T interval in the 0-40 % centrality class is shown. Each parameter variation is plotted in a different color. The acronym "PPT" stands for the pseudo-proper decay length and "rho" refers to the variation of the bandwidth parameter h . The final value for the systematic uncertainty estimation is then calculated by taking the RMS of the variations that pass the Barlow criteria [64]

$$BL = \frac{f_B^{Standard} - f_B^{Varied}}{\sqrt{|\sigma^2(f_B^{Standard}) - \sigma^2(f_B^{Varied})|}} \quad (39)$$

as explained in the inclusive analysis. In Figure 58 an example for the distribution of the f_B parameter variation that pass this criteria is shown. The RMS is then taken as the systematic uncertainty. The drawback of this approach is that sometimes only very few variations pass this criteria.

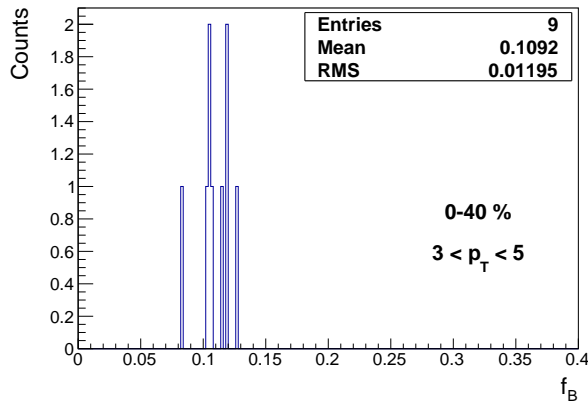


Figure 58: Estimation of the RMS of the parameter variations.

The variations for the other measured points are shown in Fig. 59 - Fig. 61. The conclusions for the variations will be shortly summarized:

1. In general it was seen that the two p_T bins $[3, 5]$ GeV/c and $[5, 10]$ GeV/c are stable. No significant dependence on the pseudo-proper decay length range or the mass window was seen. However, decreasing the lower side-band limit shows a trend to increase the measured f_B fraction.
2. The increase of the bandwidth parameter h shows a trend to decrease the measured f_B fraction, which is expected since it describes the tails of the non-prompt J/ ψ fraction in a smoother way, resulting in lifted tails. Thus the PDF tends to be scaled down in the likelihood fit compared to estimations with lower bandwidth and therefore lower values of f_B are obtained.
3. For the selection on the BDT classifier a strong dependence is seen for the $[5, 10]$ GeV/c p_T bin, while there is no clear trend seen for the $[3, 5]$ GeV/c p_T bin. Recalling that the BDT shows little improvement for the $[3, 5]$ GeV/c p_T bin, this suggests that there is a dependence on the S/B that is changed by harder selections on the BDT in the $[5, 10]$ GeV/c p_T bin. Further checks are required to clarify the origin of this effect.

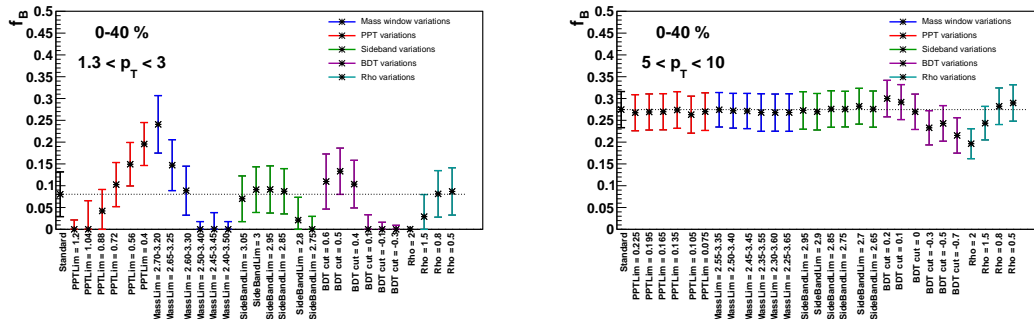


Figure 59: Left panel: variations of the fit parameters for the $[1.3, 3]$ GeV/ c p_T in the 0-40 % centrality class. Right panel: variations of the fit parameters for the $[5, 10]$ GeV/ c p_T in the 0-40 % centrality class.

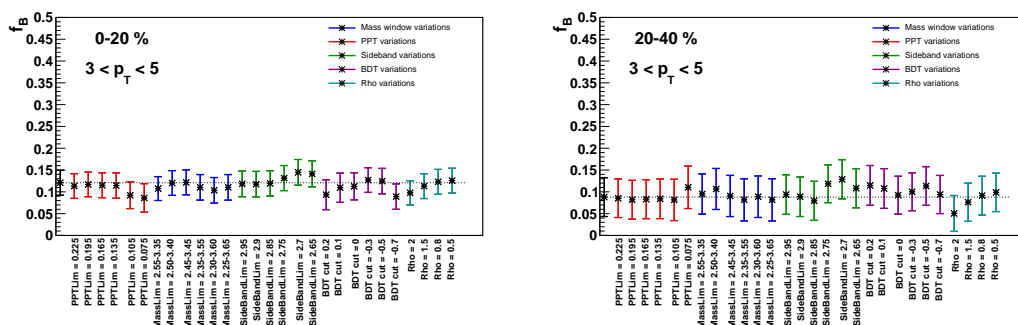


Figure 60: Left panel: variations of the fit parameters for the 0-20 % centrality in the $[3, 5]$ GeV/ c p_T bin. Right panel: variations of the fit parameters for the 20-40 % centrality class in the $[3, 5]$ GeV/ c p_T bin.

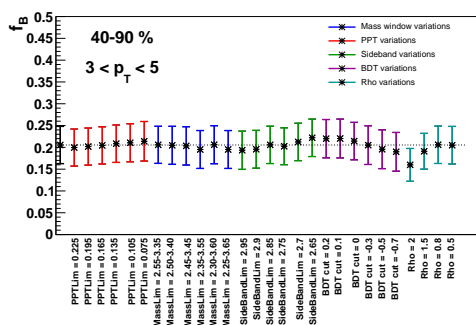


Figure 61: Variations of the fit parameters for the 40-90 % centrality class in the $[3, 5]$ GeV/ c p_T bin.

4. Furthermore it is seen that the lowest p_T bin shows a critical behavior, which is not surprising due to the low S/B ratio. It can be seen that the f_B values exhibit strong systematic trends on the range of the pseudo-proper decay length and the limits of the mass window. In general the fit shows a trend of giving a value close to zero. In particular reducing the selected BDT value gives results for f_B close to zero, again suggesting a dependence on the S/B. The problematic behavior of this bin reflects in large systematic uncertainties. Special care will be needed in order to decrease the systematic uncertainties of this bin.

For a more complete estimation of the systematic uncertainties the following tests should be considered:

- Combinations of variations of the fit parameters
- Reweighting of the efficiencies to different p_T spectra
- Variation of the invariant mass signal shape
- Variation of the background description of the invariant mass by taking the like-sign method for the background description

4.3.6. f_B reference fraction in pp at $\sqrt{s} = 5.02$ TeV

The procedure employed to determine the non-prompt J/ψ fractions in pp collisions is described in detail in [78]. It is not part of the work done in the scope of this thesis. A short overview over the procedure will be given in the following. The value of f_B in pp at $\sqrt{s} = 5.02$ TeV is determined by an interpolation procedure. For this, a fit is performed to the existing measurements of f_B as a function of p_T in mid-rapidity pp collisions at $\sqrt{s} = 7$ TeV to data of ALICE [79], ATLAS [75] and CMS [76]. The function to fit the data is defined as:

$$f_B^{model}(p_T) = \frac{d\sigma_{J/\psi \leftarrow B}^{FONLL}/dp_T}{d\sigma_{J/\psi}^{phenom}/dp_T} \quad (40)$$

which is the ratio of the differential cross section for non-prompt J/ψ obtained by an implementation of pQCD calculations at fixed order with next-to leading-log resummation (FONLL [33]) to that for inclusive J/ψ , parameterized by the phenomenological function defined as:

$$\frac{d^2\sigma}{dz_t d_y} = c \cdot \frac{z_t}{(1 + a^2 z_t^2)^n} \quad (41)$$

where $z_t = p_T/\langle p_T \rangle$ and $a = \Gamma(3/2)\Gamma(n - 3/2)/\Gamma(n - 1)$ and $c = 2(n1)a$, where n is the only free fit parameter. A similar fit is then performed to the CDF [68] results in $p\bar{p}$ collisions at $\sqrt{s} = 1.96$ TeV. The two fitted curves at $\sqrt{s} = 1.96$ TeV and $\sqrt{s} = 7$ TeV have been sampled in several points to perform an interpolation as a function of p_T at $\sqrt{s} = 5.02$ TeV. For each transverse momentum value, three different fits have been performed, assuming three different functional models (linear, exponential and power law) to describe the energy dependence of $f_B(\sqrt{s})$.

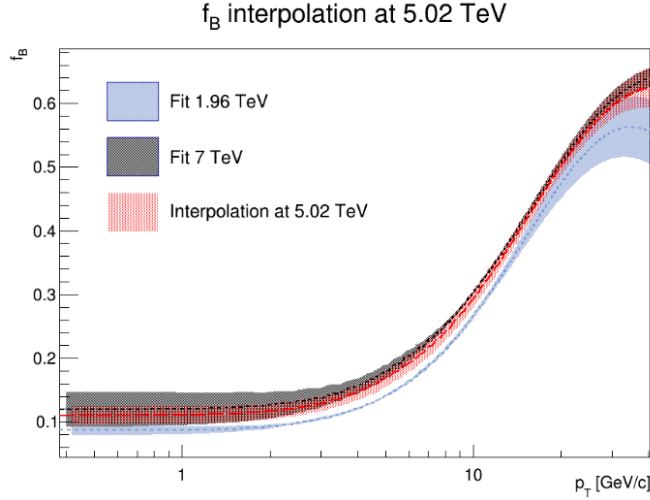


Figure 62: Energy interpolation at $\sqrt{s} = 5.02$ TeV, shown at $p_T = 2$ GeV/c. The bands represent the 1σ confidence intervals of the fits [78].

The average of the results obtained from the different functions was taken as the interpolated f_B value at $\sqrt{s} = 5.02$ TeV each p_T bin.

The final result of the procedure is shown in Fig. 62. It shows the interpolated f_B values at $\sqrt{s} = 5.02$ TeV, its uncertainty band and the fit results at $\sqrt{s} = 1.96$ TeV and $\sqrt{s} = 7$ TeV.

To compute the reference values of the fraction of non-prompt J/ψ within a given transverse momentum interval $[p_T^{min}, p_T^{max}]$, the interpolated differential curve of f_B as a function of p_T was finally integrated over the inclusive J/ψ p_T spectrum [78]:

$$\langle f_B \rangle = \frac{\int_{p_T^{min}}^{p_T^{max}} f_B \cdot \left(\frac{dN}{dp_T}\right)_{\text{Inclusive } J/\psi}^{\sqrt{s}=5.02\text{TeV}}}{\int_{p_T^{min}}^{p_T^{max}} \left(\frac{dN}{dp_T}\right)_{\text{Inclusive } J/\psi}^{\sqrt{s}=5.02\text{TeV}}} \quad (42)$$

The final values of the interpolation are shown in Table 10. The quoted uncertain-

Table 10: Reference measurement of f_B in pp collisions at $\sqrt{s} = 5.02$ TeV [78].

p_T (GeV/c)	f_B
1.3 - 3	0.118 ± 0.013
3 - 5	0.143 ± 0.012
5 - 10	0.202 ± 0.013

ties include a component from the fit procedure, which depends on the uncertainties of both data and FONLL predictions and the systematic uncertainty due to the energy interpolation, estimated by considering the different functional forms of the \sqrt{s} dependency.

4.3.7. Results for the R_{AA} of non-prompt J/ψ

Table 11: Inclusive J/ψ R_{AA} [61] and non-prompt J/ψ R_{AA} results in Pb–Pb collisions at $\sqrt{s_{NN}} = 5.02$ TeV. The first uncertainty is statistical, the second systematic.

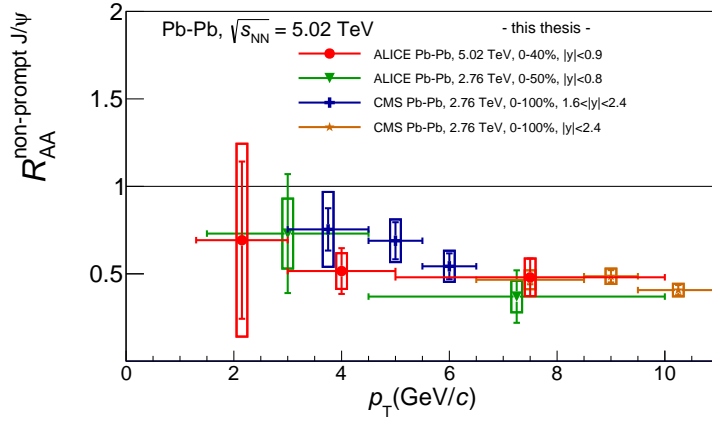
Centrality (%)	p_T (GeV/c)	inclusive J/ψ R_{AA}	non-prompt J/ψ R_{AA}
0-40	1.3 -3	$0.62 \pm 0.07 \pm 0.08$	$0.69 \pm 0.45 \pm 0.55$
0-40	3 - 5	$0.52 \pm 0.08 \pm 0.08$	$0.52 \pm 0.13 \pm 0.10$
0-40	5 - 10	$0.77 \pm 0.09 \pm 0.11$	$0.48 \pm 0.11 \pm 0.11$
0-20	3 - 5	$1.02 \pm 0.12 \pm 0.12$	$0.61 \pm 0.16 \pm 0.11$
20-40	3 - 5	$0.57 \pm 0.08 \pm 0.08$	$0.37 \pm 0.20 \pm 0.11$
40-90	3 - 5	$0.36 \pm 0.06 \pm 0.06$	$1.29 \pm 0.31 \pm 0.25$

In order to calculate the non-prompt J/ψ R_{AA} , it is necessary to combine f_B measurements with the inclusive J/ψ R_{AA} measurement using the following equation:

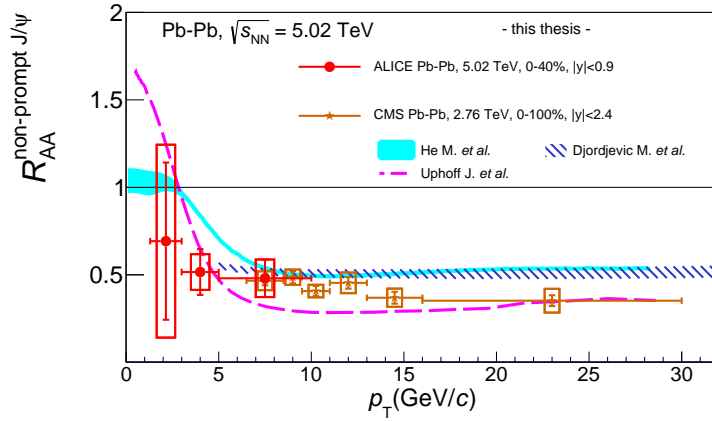
$$R_{AA}^{non-prompt} = \frac{f_B^{Pb-Pb}}{f_B^{pp}} R_{AA}^{inclusive} \quad (43)$$

The value of f_B in pp collisions at $\sqrt{s} = 5.02$ TeV, f_B^{pp} , is determined by the interpolation procedure described in section 4.3.6. The relevant measured inclusive J/ψ R_{AA} results in Pb–Pb [61], discussed in chapter 4.1, are summarized in Table 11, while the reference measurement of f_B in pp [78] are summarized in Table 10. In order to compute the statistical and systematic uncertainties on the non-prompt J/ψ R_{AA} , the relative uncertainties, both statistical and systematic, coming from the inclusive J/ψ R_{AA} and from f_B results, are separately added in quadrature. The uncertainty on the f_B reference in pp is considered as a systematic uncertainty only [78].

In Fig. 63a the nuclear modification factor for non-prompt J/ψ at $\sqrt{s_{NN}} = 5.02$ TeV for the three p_T bins [1.3, 3] GeV/c, [3, 5] GeV/c, [5, 10] GeV/c in the mid-rapidity range $|y| < 0.9$ is shown together with the measurement by ALICE in Pb–Pb collisions at $\sqrt{s_{NN}} = 2.76$ TeV in the p_T intervals [1.5, 4.5] GeV/c and [4.5, 10] GeV/c in the mid-rapidity range $|y| < 0.8$ in the centrality class 0-50 % [49]. The horizontal bars symbolize the width of the bin. The values of the non-prompt J/ψ R_{AA} are placed in the center of the bin. Also shown is the the result by CMS at $\sqrt{s_{NN}} = 2.76$ TeV in the p_T interval [3, 6.5] GeV/c in the forward-rapidity range $1.6 < |y| < 2.4$ in the centrality class 0-100 % and the result by CMS for the p_T interval of [6.5, 30] GeV/c in the mid-rapidity range $|y| < 2.4$, also at $\sqrt{s_{NN}} = 2.76$ TeV [52]. The current analysis at $\sqrt{s_{NN}} = 5.02$ TeV extends the measurement by CMS at $\sqrt{s_{NN}} = 2.76$ TeV in mid-rapidity to lower p_T . The shown measurements for the non-prompt J/ψ R_{AA} at the different energies, centrality classes and rapidity intervals are compatible within uncertainties. A suppression of the non-prompt J/ψ R_{AA} is seen with increasing transverse momentum. Although a dependence of the non-prompt J/ψ R_{AA} on the rapidity is expected, as measured by CMS for higher p_T [52], the precision of the measurements is not yet sufficient to resolve this.



(a) Non-prompt J/ψ R_{AA} at $\sqrt{s_{NN}} = 5.02$ TeV as a function of p_T compared to measurements by CMS at $\sqrt{s_{NN}} = 2.76$ TeV [52] and ALICE at $\sqrt{s_{NN}} = 2.76$ TeV [49]. See text for details.



(b) Non-prompt J/ψ R_{AA} at $\sqrt{s_{NN}} = 5.02$ TeV as a function of p_T compared to measurements by CMS at $\sqrt{s_{NN}} = 2.76$ TeV [52] and the models by Djordjevic et. al [41], Uphoff et. al (BAMPS) [42] and He et. al (TAMU) [43].

Figure 63

In Fig. 63b the theoretical model predictions, that were discussed in chapter 2.1.5, computed for $\sqrt{s_{NN}} = 2.76$ TeV in the centrality class 0 – 50%, are overlaid. Since the models do not predict a strong dependence of the R_{AA} on the collision energy, it is justified to compare the measured non-prompt J/ψ R_{AA} at $\sqrt{s_{NN}} = 5.02$ TeV with the model predictions at $\sqrt{s_{NN}} = 2.76$ TeV. The BAMPS model by Uphoff et al. [42] is based on the Boltzmann equation and does not include radiative processes for heavy quarks. The model TAMU of He et al. [43] is a non-perturbative T-matrix approach in a fluid-dynamic model. The model of Djordjevic [41] is a pQCD energy loss model in a static fireball and includes both collisional energy loss and radiative energy loss. The models show qualitatively the same trends as the measurements, showing a strong suppression with increasing transverse mo-

mentum. However more precise data are needed to put strong constraints on the models, in particular at low transverse momentum.

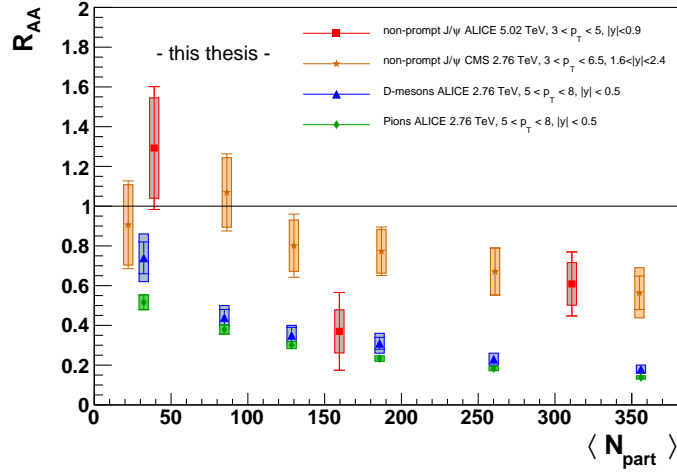


Figure 64: Non-prompt J/ψ R_{AA} as function of the centrality at $\sqrt{s_{NN}} = 5.02$ TeV compared with a measurement of the non-prompt J/ψ by CMS at $\sqrt{s_{NN}} = 2.76$ TeV [52] and of the R_{AA} of D-mesons [46] and pions [80] by ALICE at $\sqrt{s_{NN}} = 2.76$. See text for details.

In Fig. 64 the non-prompt J/ψ R_{AA} at $\sqrt{s_{NN}} = 5.02$ TeV is shown as a function of centrality, where centrality is expressed as $\langle N_{part} \rangle$, in the p_T interval [3, 5] GeV/c in the rapidity range $|y| < 0.9$. Also shown are the results by CMS for the non-prompt J/ψ R_{AA} at $\sqrt{s_{NN}} = 2.76$ TeV integrated in p_T in the interval [3, 6.5] GeV/c in the forward-rapidity range $1.6 < |y| < 2.4$ as a function of centrality [52]. Within uncertainties the measurements are in agreement. It is particularly interesting to compare the measurements for the non-prompt J/ψ R_{AA} as a function of centrality to the R_{AA} of D-mesons and charged hadrons to test the expected hierarchy in the parton energy loss $\Delta E_g > \Delta E_u, d, s > \Delta E_c > \Delta E_b$. On average the p_T of the beauty hadron, that the non-prompt J/ψ originates from, is higher than the p_T of the non-prompt J/ψ . Thus it is important to ensure that the p_T intervals of the D-mesons and charged hadrons overlap with the p_T interval of the parent beauty hadrons. As a first attempt, measurements of the R_{AA} of D-mesons [46] and pions [80] by ALICE at $\sqrt{s_{NN}} = 2.76$ integrated in p_T in the interval [5, 8] GeV/c are used for a comparison, assuming that there is some overlap of the p_T distributions. To improve the comparison, the intervals have to be chosen such, that the mean p_T of the charm and beauty hadrons are similar. The measured values together with the result by CMS give a hint that the beauty hadrons are less suppressed than D-mesons and pions. To conclude that this observation is due to the mass dependence of quark-medium interactions, comparisons with model predictions are needed, since effects, as e.g. different p_T distributions of the initially produced charm and beauty quarks could contribute to differences in the R_{AA} .

5. Topological vertexing approach at low transverse momentum in Pb–Pb

In the scope of this thesis a topological vertexing approach was developed to reconstruct beauty hadrons in Pb–Pb collisions at low transverse momentum. In the following the results are briefly summarised.

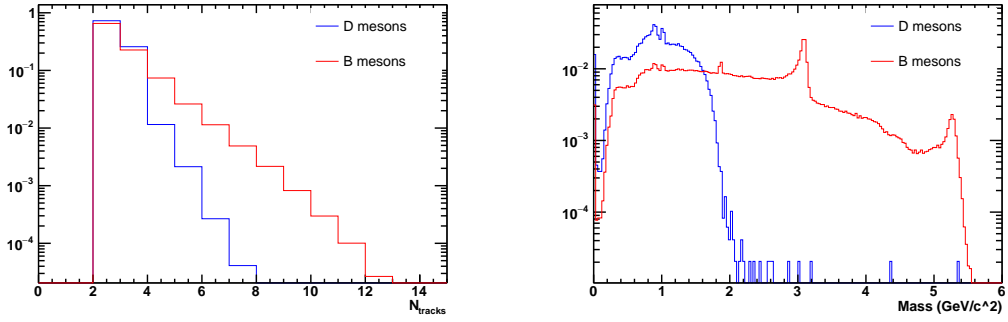
5.1. Basic idea

The main idea of this analysis is to exploit the fact that beauty hadrons decay on average into more daughters than charm hadrons and that their masses are significantly higher. A promising study was carried out in pp collisions in [81]. In Fig. 65a, the number of measurable tracks of the particles in the decay cascade for charm hadrons (D^0 , D^\pm , D_s^+ , Λ_s^+) and beauty hadrons (B^0 , B^\pm , B_s^0 , B_c^+ , Λ_b^0) in a MC simulation is shown, where the tracks were required to fulfill the selection criteria described in the following section. Therefore the particle selection was driven by the MC knowledge of the heavy-flavour decay chain. Calculating the invariant mass of the shown tracks results in the distribution shown in Fig. 65b. The mass spectra are continuous, since not all particles in the decay chain are measurable. The idea to be tested was whether it is possible to select a pure sample of beauty hadrons by searching for secondary vertices that contain a high number of tracks and subsequently applying a selection on this number and setting a threshold for the invariant mass. Due to the very high multiplicity of hadron tracks, the attempt was made to use electron tracks as a starting point for the search of secondary vertices. Electrons are rarer and among them there are the decay products of semi-leptonic decays of heavy-flavour hadrons: those electrons are characterized by a large impact parameter with respect to the primary vertex of the event. The main challenge is to find an algorithm to obtain a vertex starting from the track of the electron, without having information about which of the remaining tracks in the event truly belong to the decay of the beauty hadron. All the selected tracks in the event have to be considered as possibly belonging to a beauty hadron decay. An approach with multitrack displaced vertices was used by ATLAS in pp collisions for the search for massive, long-lived particles [82].

5.2. Data sample and algorithm

The feasibility study is done based on a Monte-Carlo simulation. The used period is LHC12a17e_fix, which is anchored to the Pb–Pb data period LHC11h. It makes use of the generator HIJING and contains injected HF signals. It contains Pb–Pb collisions for the 10-50% centrality class. The events were selected by requiring the reconstructed primary vertex to have at least one contributing track and a z -coordinate lying within $[-10, 10]$ cm from the nominal center of the experiment. To be considered further for the vertexing algorithm, a refit in the TPC and ITS was required, as well as a minimum of 70 clusters in the TPC and 4 clusters in the ITS.

An algorithm was tested that forms clusters of tracks along the track of the electron. It is described briefly in the following. The algorithm is based on [69].



(a) Number of measurable tracks in Monte- (b) Invariant mass spectra for the tracks in Carlo for beauty and charm hadrons. a).

Figure 65

1. Selection of a displaced electron with impact parameter in the plane transversal to the beam direction divided by the uncertainty fulfilling:

$$\frac{DCA_{xy}}{\sigma(DCA_{xy})} > 3 \quad (44)$$

2. Calculate all two-track vertices with the remaining tracks in the event and keep the ones that have a $\chi^2/\text{NDF} < 3$. This is done making use of the KFParticle vertexing package [69].
3. Subsequently merge the two-track vertices into larger vertices containing multiple tracks (thus forming track clusters), requiring the fit of the new vertices to have a $\chi^2/\text{NDF} < 3$.
4. Stop when it is not possible to further merge the vertices without fulfilling the criterion $\chi^2/\text{NDF} < 3$.
5. Calculate the invariant mass and the decay length L_{xy} in the transverse plane of the found vertices.

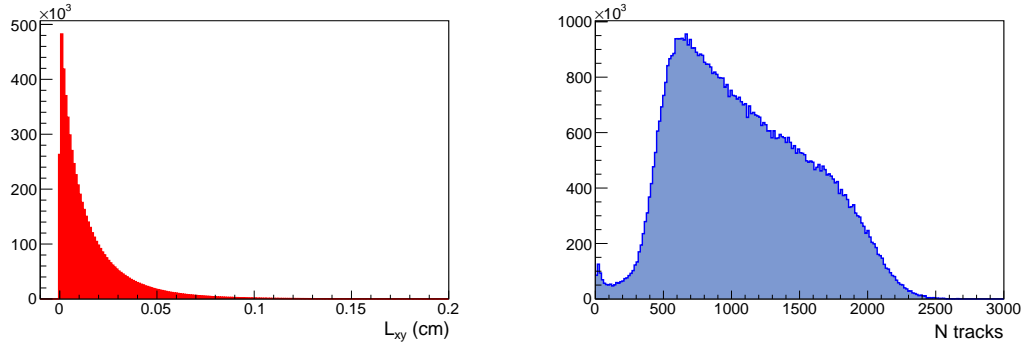
Finally a vertex with an associated track cluster is considered as a candidate for a beauty hadron decay vertex, when the distance between its center and the true MC decay vertex of the hadron in the transverse plane, divided by the uncertainty on this distance, is smaller than 3 deviations.

5.3. Results and conclusions

The decay length in the laboratory frame for a particle of mass M and momentum p can be calculated as:

$$L = \frac{p}{M} ct^{proper} \quad (45)$$

where t^{proper} is the proper decay time in the rest frame of the particle. For low p_T this implies that the beauty hadrons decay very close to the primary vertex due to their high mass. In Fig. 66a the distance between the MC primary vertex



(a) Decay length in the transverse plane L_{xy} for beauty hadrons with $p_T < 3$. (b) Total number of tracks passing the selection criteria in the selected events.

Figure 66

and the MC decay vertex of the beauty hadrons in the transverse plane L_{xy} is shown for beauty hadrons with $p_T < 3$ GeV/c. It can be seen that up to a distance of 1mm most of the initial beauty hadrons are decayed. In Fig. 66b the total number of tracks in the Pb-Pb events that pass the selection criteria is shown. As expected in heavy-ion collisions, the multiplicity is very high reaching up to a few thousand tracks. Both plots together illustrate the great challenge of the topological approach: since the low p_T beauty hadrons decay close to the interaction vertex, it is impossible to avoid including tracks in the vertex fit that do not belong to the decay of the beauty hadron. It also is impossible to make hard selections on the decay length (of a vertex found by the algorithm) without losing most of the statistics.

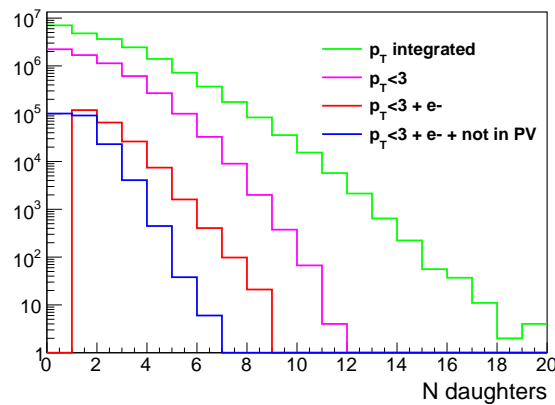


Figure 67: Number of true measurable daughters in the decay cascade of beauty hadrons after applying subsequently stronger selection criteria. Details are in the text.

In Fig. 67 the total number of tracks in the decay chain of the beauty hadrons, that fulfill the track selection criteria, are shown. In particular shown are the total number of true measurable daughters without selections on the transverse momentum (green), the total number of true measurable daughters after making a selection on the transverse momentum of the beauty hadron $p_T < 3$ GeV/c (magenta), the total number of true measurable daughters after additionally requiring

a displaced electron (red) and finally the total number of true measurable daughters after additionally requiring the daughter tracks of the beauty hadron not to be included in the primary vertex fit. It was investigated whether selections on the tracks in the event make it possible to keep mainly daughters of the beauty hadrons, e.g. by only considering tracks that are not included in the primary vertex fit. However, it was found that by applying harder selections on the tracks in the events also daughters of the beauty hadron are rejected and the number of the remaining daughters to form a vertex including a large number of (true beauty hadron daughter) tracks was too small. Moreover still many tracks were picked up in the candidate clusters that did not belong to the beauty decay. Therefore within the scope of this thesis it was not possible to find criteria to identify a cluster as a vertex of a beauty hadron without making use of the true MC information. In particular the ideal invariant mass distribution shown in Fig. 65b was strongly smeared out due to the tracks not belonging to the beauty hadron. Therefore it was concluded that at low transverse momentum this approach is not suitable in Pb–Pb collisions.

6. Conclusions and outlook

In this work the first measurement of beauty production at low transverse momentum in central Pb–Pb collisions at $\sqrt{s_{NN}} = 5.02$ TeV at mid-rapidity is presented. The measurement was done via J/ψ coming from beauty hadron decays by decomposing the inclusive J/ψ yield into its prompt and non-prompt components. This was achieved via a 2-dimensional log-likelihood fit to the invariant mass and the pseudo-proper decay length distribution. The framework of the fit was implemented in RooFit within the scope of this thesis. A first study was carried out evaluating the possibilities of using multivariate methods to improve the challenging signal to background conditions found in the inclusive J/ψ production analysis. It was found that the usage of multivariate methods is applicable and has potential for improvement of the signal to background and the significance. Moreover a topological vertexing approach to measure beauty production at low transverse momentum was attempted. It had to be concluded that this approach is not applicable at low transverse momentum due to the high multiplicities in Pb–Pb collisions.

The results for the measured nuclear modification factor for non-prompt J/ψ was presented as a function of transverse momentum and centrality. It was found to be in agreement with previous measurements at lower energies. The R_{AA} was obtained by combining the measured fraction of non-prompt J/ψ in Pb–Pb with the interpolated fraction of non-prompt J/ψ in pp collisions at $\sqrt{s} = 5.02$ TeV and the inclusive J/ψ R_{AA} measured in Pb–Pb collisions at $\sqrt{s_{NN}} = 5.02$ TeV via:

$$R_{AA}^{non-prompt} = \frac{f_B^{Pb-Pb}}{f_B^{pp}} R_{AA}^{inclusive}$$

The dominating uncertainty of the measured non-prompt J/ψ R_{AA} is the uncertainty of the f_B measurement in Pb–Pb. A clear suppression was seen with increasing momentum. A hint for less suppression of beauty hadrons than for charm hadrons and pions was seen as a function of centrality. Compared to the previous measurement by ALICE at $\sqrt{s_{NN}} = 2.76$ TeV it was possible to present the non-prompt J/ψ R_{AA} in an additional p_T bin.

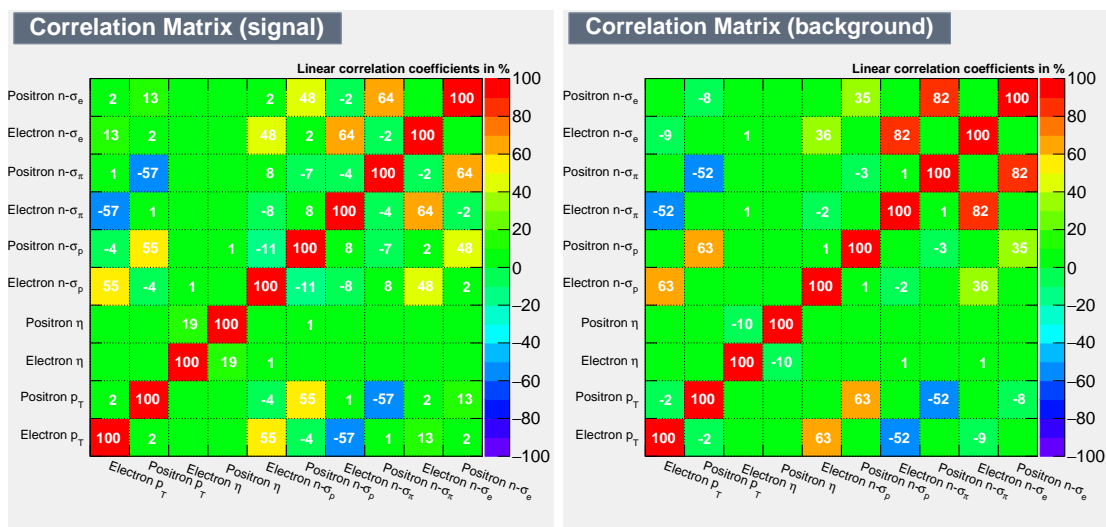
To bring the measurement of the non-prompt J/ψ R_{AA} of this thesis towards a publication, several studies have to be carried out. Due to the challenging signal to background conditions in all bins, toy Monte-Carlo studies have to be carried out to validate the fit and get an estimate for the goodness of the fit. Moreover by mixing electron-positron pairs from data that contain as few J/ψ as possible with MC electron-positron pairs from true J/ψ decays, it is possible to control the input of the fit and by fitting this distribution get a better understanding of the uncertainties of the fit connected with the ratio of signal to background. The systematic uncertainty estimation has to be refined. In particular at low transverse momentum extensive studies are needed, due to the problematic behavior of the fit. The density estimation approach to obtain the PDFs has to be compared to the results of the fit obtained with the parametrization employed by CDF that is used in the previous non-prompt J/ψ analysis. The acceptance times efficiency of the prompt and non-prompt J/ψ components has to be reweighted properly to natural p_T distributions and a systematic uncertainty has to be estimated. The

variations of the parameters of the fit should be combined randomly for the systematic uncertainty estimation. Moreover the correlation between the transverse momentum of the J/ψ and the parent beauty hadron has to be quantified.

On the short term, in view of the upcoming 2018 Pb–Pb run, the studies of multivariate methods will become of high importance. For the uncertainties of the log-likelihood fit, it was seen that the signal to background plays a crucial role. In particular at low transverse momentum it is considered to be the limiting factor. An important source of the background are photon conversions. However, the amount of photon conversions will not change without upgrading the detector by reducing the material. The main potential to improve the S/B, before an upgrade of the detector is improving the selection of J/ψ candidates. For this the use of multivariate methods will be the key to improve the measurements of both the inclusive J/ψ production and the non-prompt J/ψ production analysis. For a further improvement with the multivariate methods, it will be important to get a better understanding of the input for the training of the methods, both in Monte-Carlo and data. The development of a dedicated fast simulation would be of great benefit. It also should be considered to exploit additional information for the separation of the prompt and non-prompt component supplemental to the pseudo-proper decay length, such as the impact parameter of the tracks or the pointing angle of the J/ψ candidate. The existing measurements indicate that the dependence of the non-prompt J/ψ R_{AA} on the collision energy is small. Therefore, together with the new 2018 Pb–Pb data, a combined fit in energy to the $\sqrt{s_{NN}} = 2.76$ TeV and the $\sqrt{s_{NN}} = 5.02$ TeV data can be considered to have higher statistics and obtain a more precise result of the non-prompt J/ψ fraction in Pb–Pb collisions.

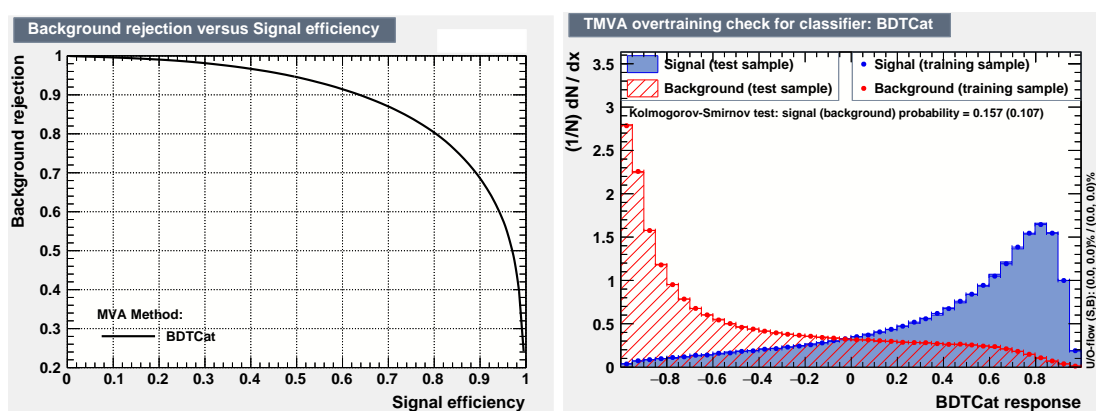
On the long term, the unique contribution of ALICE to the HF program at the LHC will be measurements at low transverse momentum at mid-rapidity, since ALICE is the only experiment that can access this region. The upgrade for run 3 will be crucial to decrease the uncertainties at low transverse momentum to provide stronger constraints on the nuclear modification factor and the elliptic flow of beauty quarks for model calculations. This will make the next step towards a characterization of the properties of the QGP, in particular the extraction of the HF transport coefficients with the final goal of connecting the phenomenological analysis with first principle QCD calculations.

A. Additional figures for the TMVA studies



(a) Linear correlation matrix for the signal for all p_T bins. (b) Linear correlation matrix for the background for all p_T bins.

Figure 68



(a) ROC-curve integrated in all p_T bins. (b) Test of overtraining integrated in all p_T bins.

Figure 69

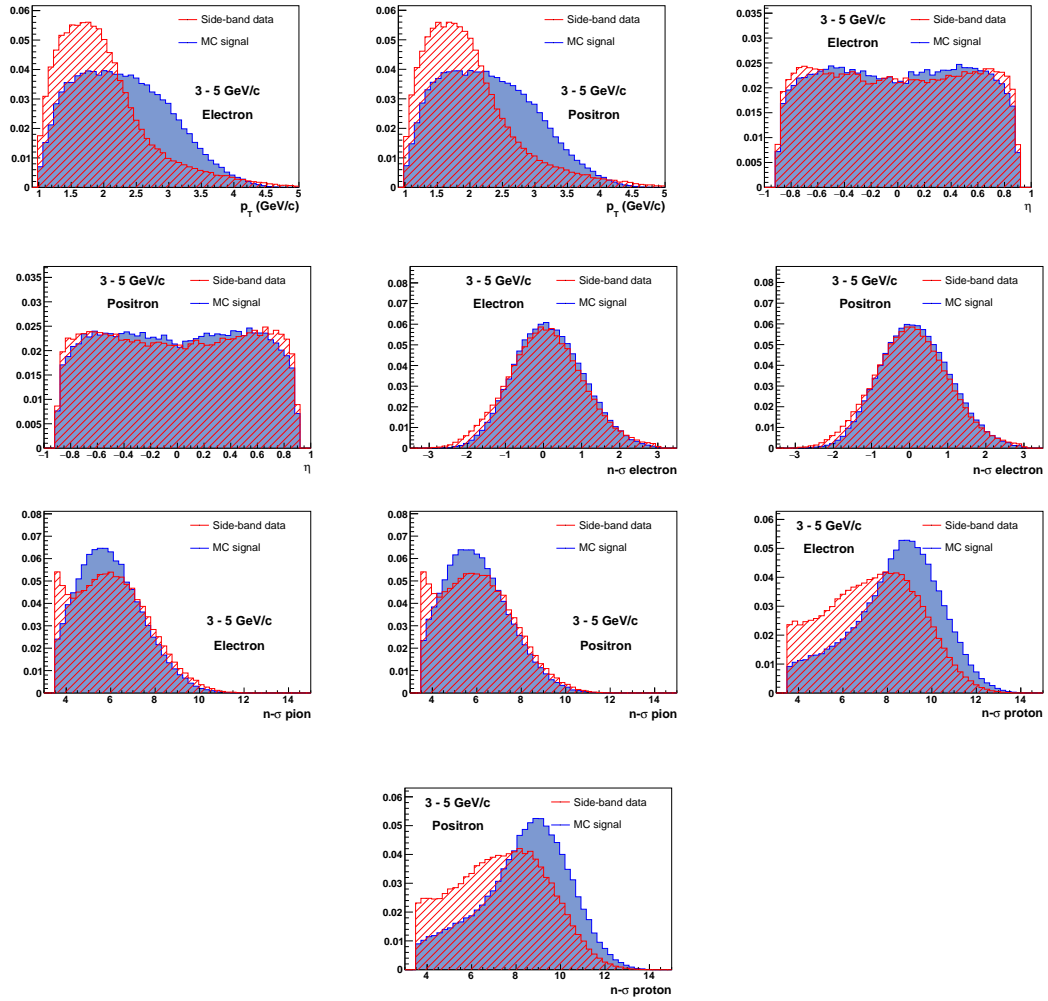
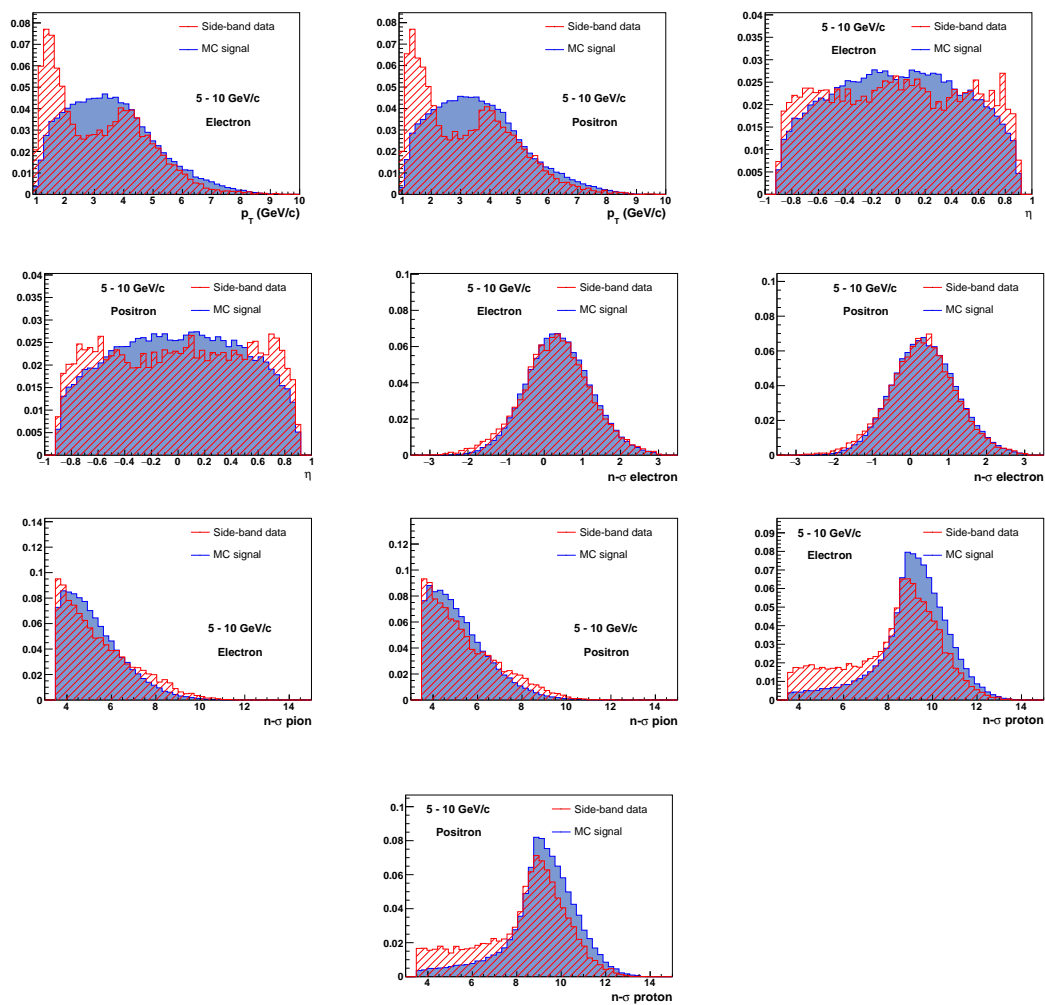


Figure 70: Input variables for the [3, 5] GeV/c bin.

Figure 71: Input variables for the $[5, 10]$ GeV/c bin.

B. Additional figures for the simultaneous log-likelihood fit

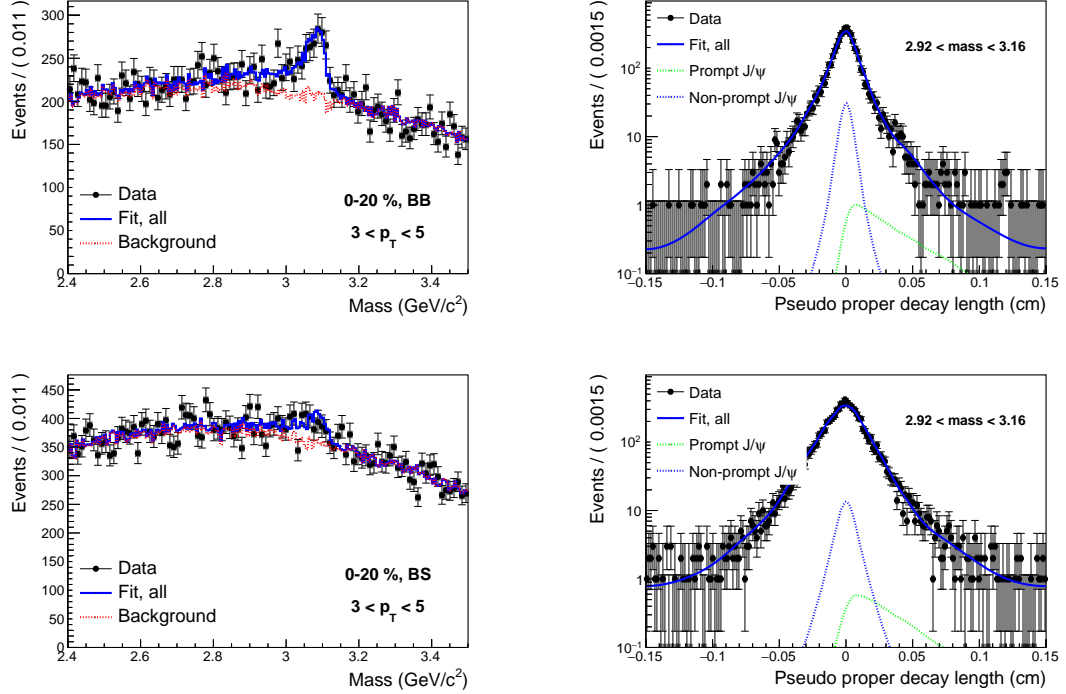


Figure 72: The invariant mass (left panel) and pseudo-proper decay length (right panel) distributions for e^+e^- pairs in the p_T bin $[3, 5]$ GeV/c in Pb-Pb collisions in the centrality interval 0-20% at $\sqrt{s_{NN}} = 5.02$ TeV. The projections of the maximum likelihood fit for the categories BB and BS are shown in this order from top to bottom.

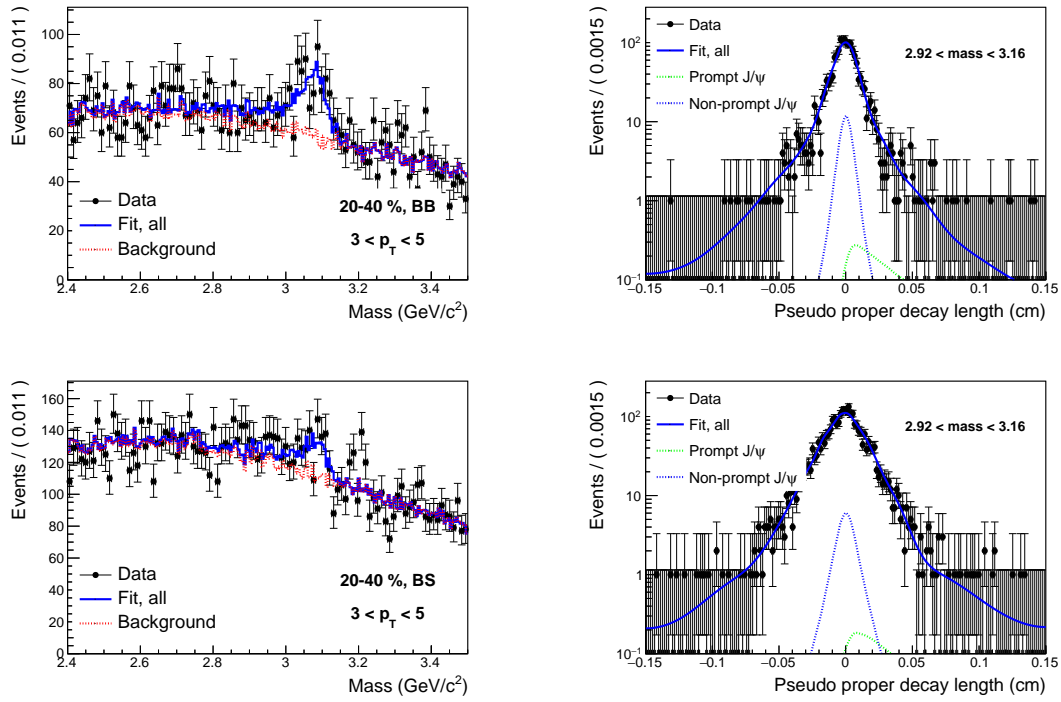


Figure 73: The invariant mass (left panel) and pseudo-proper decay length (right panel) distributions for e^+e^- pairs in the p_T bin $[3, 5]$ GeV/c in Pb-Pb collisions in the centrality interval 20-40% at $\sqrt{s_{NN}} = 5.02$ TeV. The projections of the maximum likelihood fit for the categories BB and BS are shown in this order from top to bottom.

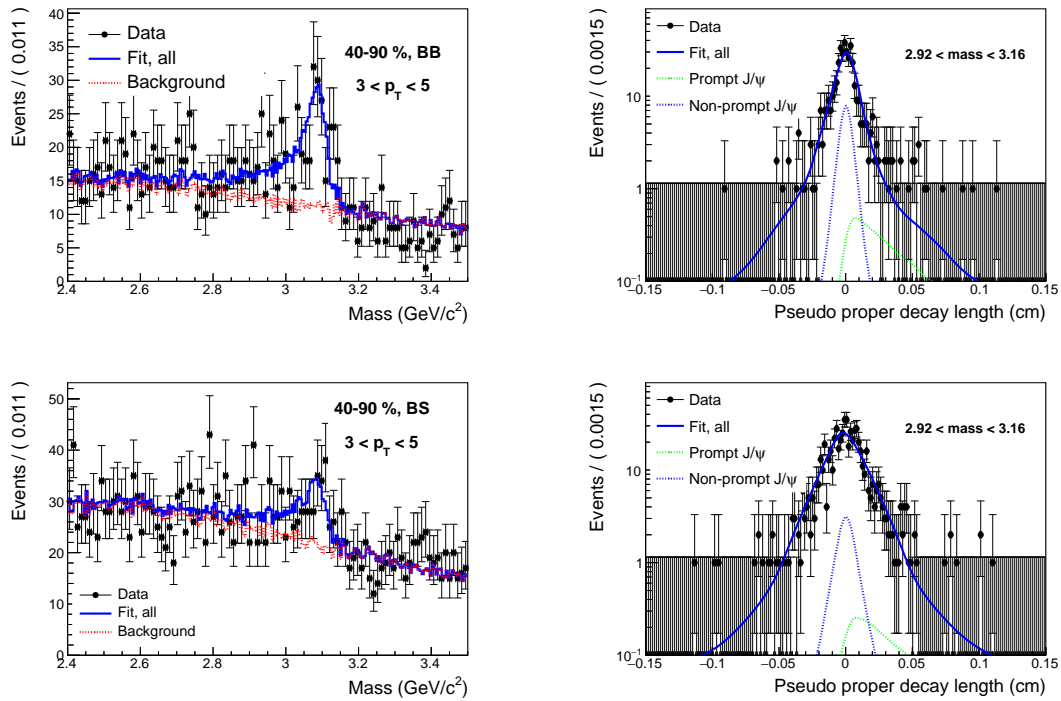


Figure 74: The invariant mass (left panel) and pseudo-proper decay length (right panel) distributions for e^+e^- pairs in the p_T bin $[3, 5]$ GeV/c in Pb-Pb collisions in the centrality interval 40-90% at $\sqrt{s_{NN}} = 5.02$ TeV. The projections of the maximum likelihood fit for the categories BB and BS are shown in this order from top to bottom.

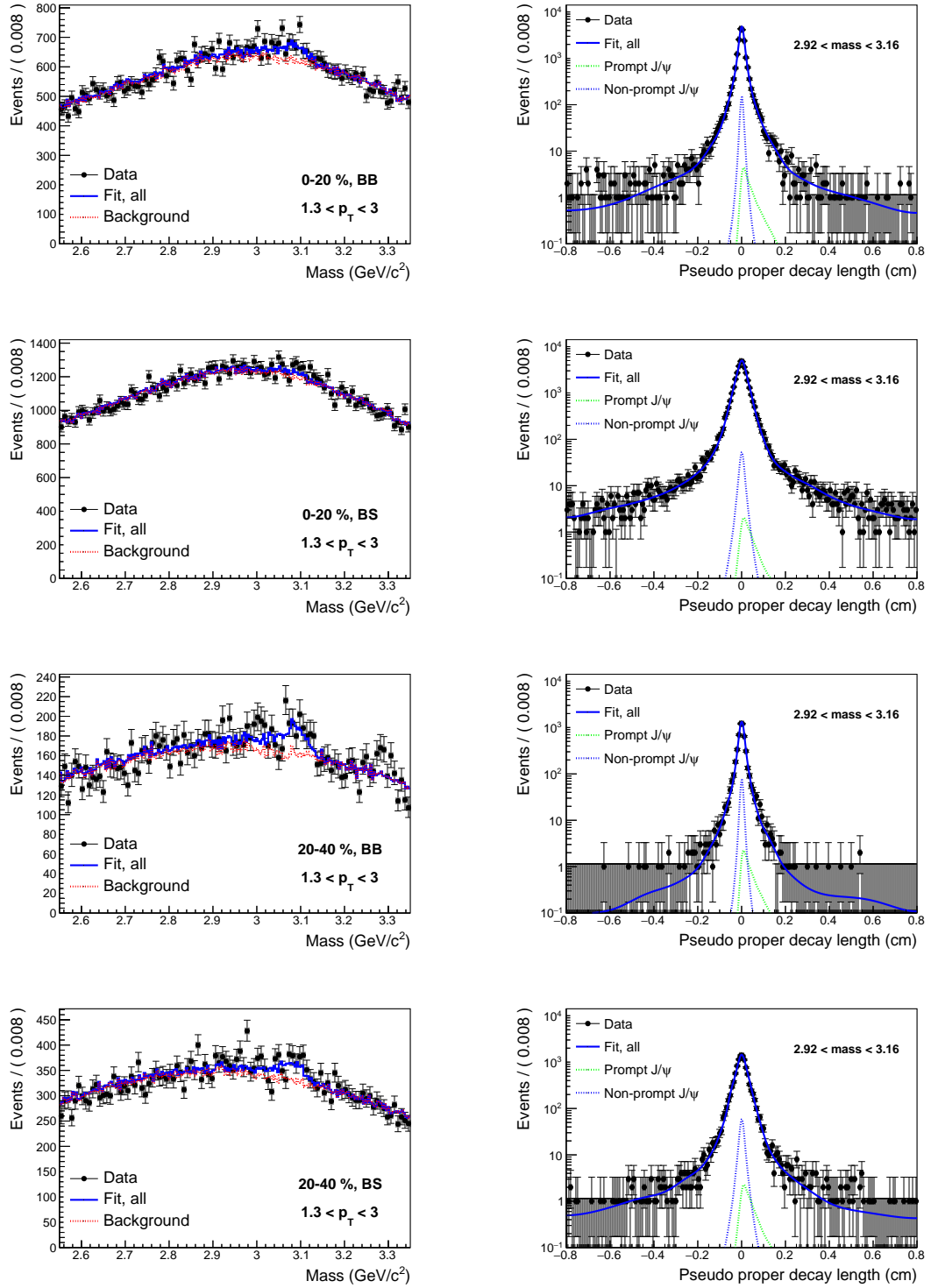


Figure 75: The invariant mass (left panel) and pseudo-proper decay length (right panel) distributions for e^+e^- pairs in the p_T bin $[1.3, 3]$ GeV/c in Pb-Pb collisions in the centrality interval 0-40% at $\sqrt{s_{NN}} = 5.02$ TeV. The projections of the maximum likelihood fit for the category BB 0-20%, BS 0-20%, BB 20-40%, BS 20-40% are shown in this order from top to bottom.

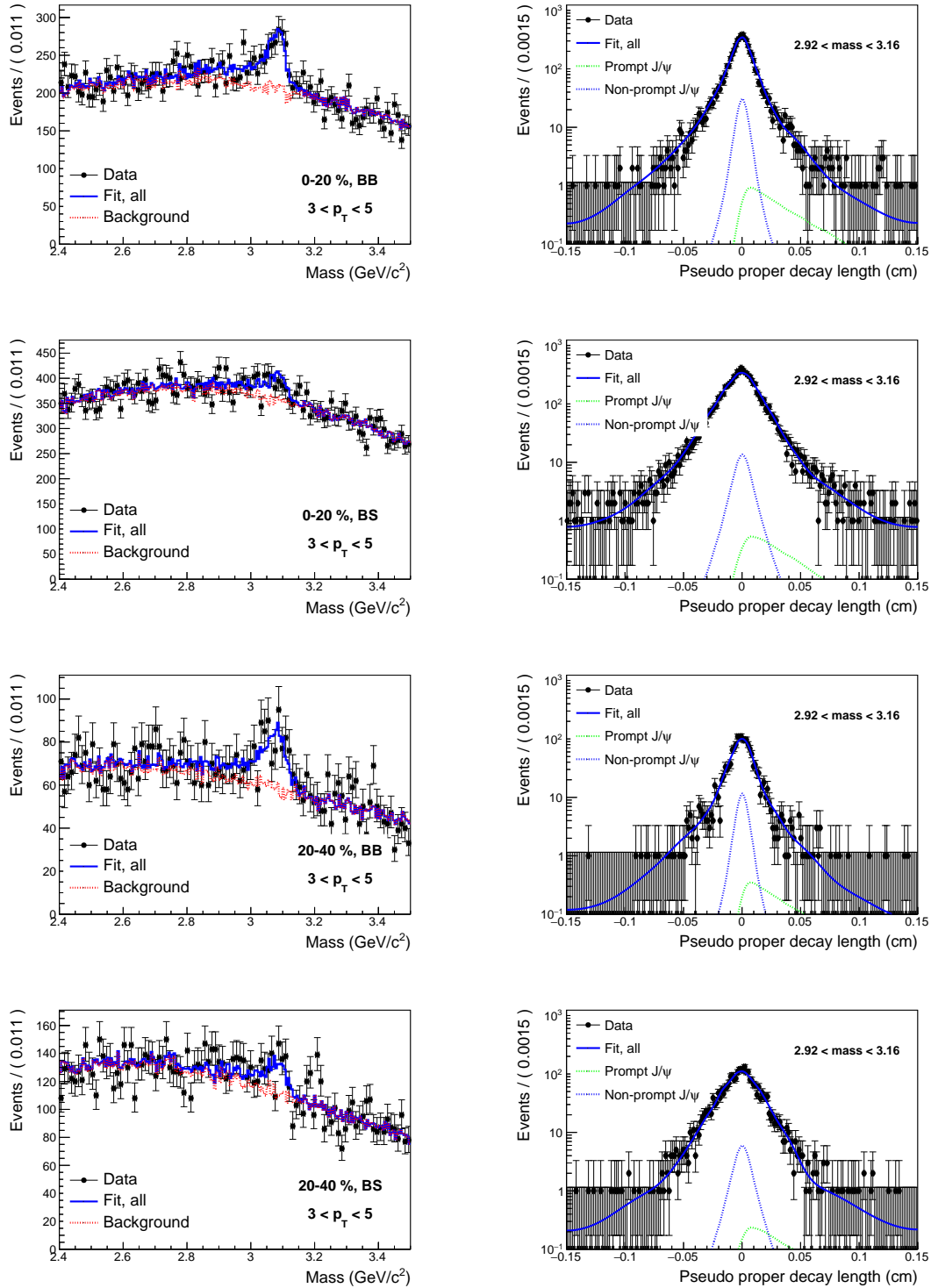


Figure 76: The invariant mass (left panel) and pseudo-proper decay length (right panel) distributions for e^+e^- pairs in the p_T bin $[3, 5]$ GeV/c in Pb-Pb collisions in the centrality interval 0-40% at $\sqrt{s_{NN}} = 5.02$ TeV. The projections of the maximum likelihood fit for the category BB in 0-20%, BS 0-20%, BB 20-40%, BS 20-40% are shown in this order from top to bottom.

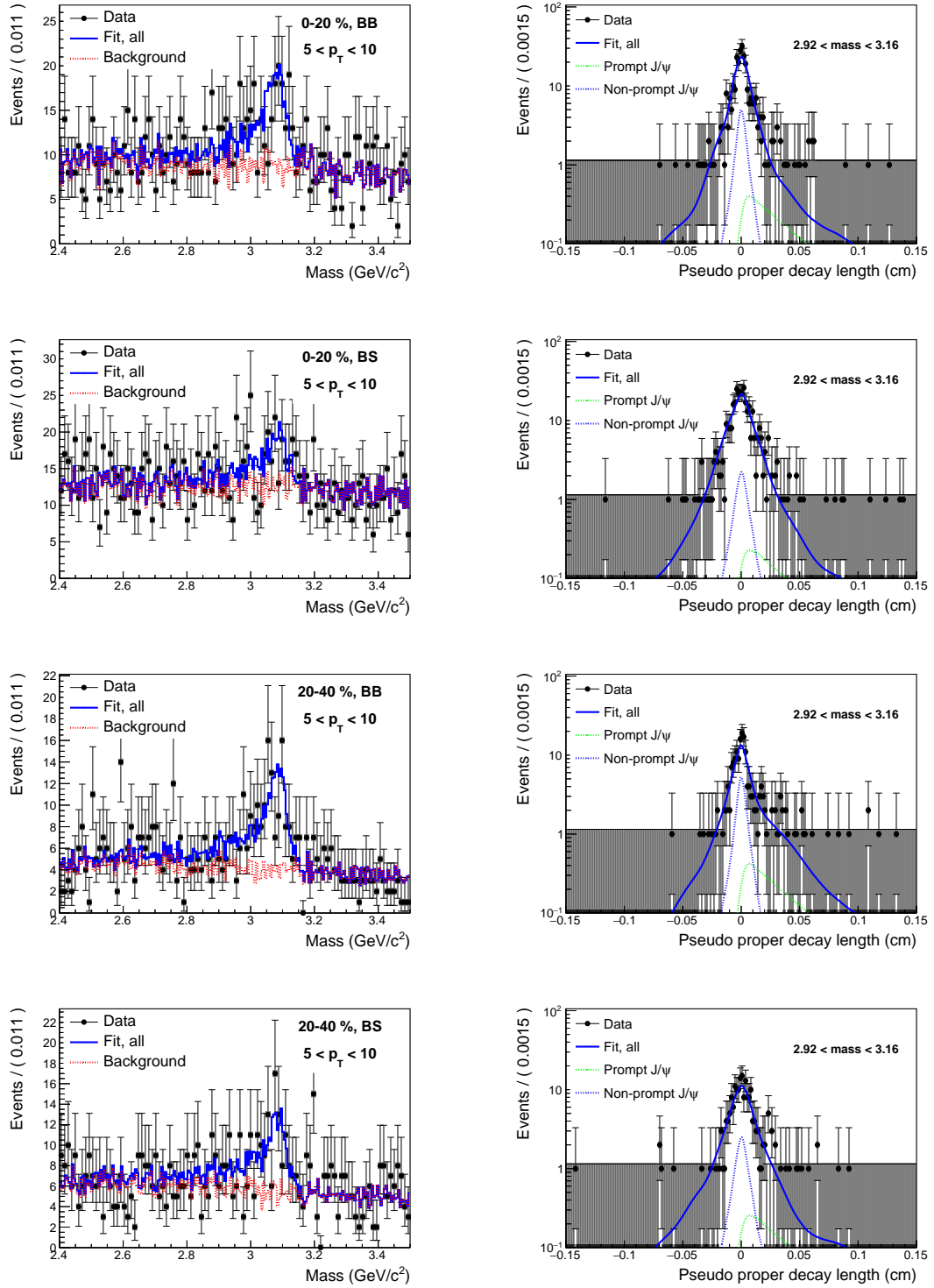


Figure 77: The invariant mass (left panel) and pseudo-proper decay length (right panel) distributions for e^+e^- pairs in the p_T bin $[5, 10]$ GeV/c in Pb-Pb collisions in the centrality interval 0-40% at $\sqrt{s_{NN}} = 5.02$ TeV. The projections of the maximum likelihood fit for the category BB in 0-20%, BS 0-20%, BB 20-40%, BS 20-40% are shown in this order from top to bottom.

References

- [1] A. Zee. *Quantum Field Theory in a Nutshell*. Princeton University Press, 2010.
- [2] K. A. Olive et al. “Review of Particle Physics”. In: *Chin. Phys.* C38 (2014). Particle Data Group, p. 090001. DOI: [10.1088/1674-1137/38/9/090001](https://doi.org/10.1088/1674-1137/38/9/090001).
- [3] Mark Thomson. *Modern particle physics*. New York: Cambridge University Press, 2013. ISBN: 9781107034266. URL: <http://www-spires.fnal.gov/spires/find/books/www?cl=QC793.2.T46::2013>.
- [4] Mark Srednicki. *Quantum Field Theory*. Cambridge: Cambridge Univ. Press, 2007. URL: <https://cds.cern.ch/record/1019751>.
- [5] David J. Gross and Frank Wilczek. “Ultraviolet Behavior of Nonabelian Gauge Theories”. In: *Phys. Rev. Lett.* 30 (1973), pp. 1343–1346. DOI: [10.1103/PhysRevLett.30.1343](https://doi.org/10.1103/PhysRevLett.30.1343).
- [6] H. David Politzer. “Reliable Perturbative Results for Strong Interactions?” In: *Phys. Rev. Lett.* 30 (1973), pp. 1346–1349. DOI: [10.1103/PhysRevLett.30.1346](https://doi.org/10.1103/PhysRevLett.30.1346).
- [7] Kenneth G. Wilson. “Confinement of quarks”. In: *Phys. Rev. D* 10 (8 1974), pp. 2445–2459. DOI: [10.1103/PhysRevD.10.2445](https://doi.org/10.1103/PhysRevD.10.2445). URL: <https://link.aps.org/doi/10.1103/PhysRevD.10.2445>.
- [8] Helmut Satz. “The Thermodynamics of Quarks and Gluons”. In: *The Physics of the Quark-Gluon Plasma: Introductory Lectures*. Ed. by Sourav Sarkar, Helmut Satz, and Bikash Sinha. Berlin, Heidelberg: Springer Berlin Heidelberg, 2010, pp. 1–21. ISBN: 978-3-642-02286-9. DOI: [10.1007/978-3-642-02286-9_1](https://doi.org/10.1007/978-3-642-02286-9_1). URL: https://doi.org/10.1007/978-3-642-02286-9_1.
- [9] Helmut Satz. “The Quark-Gluon Plasma: A Short Introduction”. In: *Nucl. Phys. A* 862-863 (2011), pp. 4–12. DOI: [10.1016/j.nuclphysa.2011.05.014](https://doi.org/10.1016/j.nuclphysa.2011.05.014). arXiv: [1101.3937 \[hep-ph\]](https://arxiv.org/abs/1101.3937).
- [10] R. Hagedorn. “Statistical thermodynamics of strong interactions at high-energies”. In: *Nuovo Cim. Suppl.* 3 (1965), pp. 147–186.
- [11] E.V. Shuryak. “Theory of hadron plasma”. In: *Sov. Phys. - JETP (Engl. Transl.); (United States)* 47:2 (1978).
- [12] Heng-Tong Ding, Frithjof Karsch, and Swagato Mukherjee. “Thermodynamics of strong-interaction matter from Lattice QCD”. In: *Int. J. Mod. Phys. E* 24.10 (2015), p. 1530007. DOI: [10.1142/S0218301315300076](https://doi.org/10.1142/S0218301315300076). arXiv: [1504.05274 \[hep-lat\]](https://arxiv.org/abs/1504.05274).
- [13] F. Karsch. “Deconfinement and chiral symmetry restoration in QCD with fundamental and adjoint fermions”. In: (1998). [PoScorfu98,008(1998)].
- [14] A. Bazavov et al. “Chiral and deconfinement aspects of the QCD transition”. In: *Physical review D: Particles and fields* 85.5 (Mar. 2012). ISSN: 0556-2821. DOI: [10.1103/PhysRevD.85.054503](https://doi.org/10.1103/PhysRevD.85.054503).

- [15] Y. Aoki et al. “The QCD transition temperature: results with physical masses in the continuum limit II.” In: *JHEP* 06 (2009), p. 088. DOI: [10.1088/1126-6708/2009/06/088](https://doi.org/10.1088/1126-6708/2009/06/088). arXiv: [0903.4155](https://arxiv.org/abs/0903.4155) [hep-lat].
- [16] A. Bazavov et al. “Equation of state in (2 + 1)-flavor QCD”. In: *Phys. Rev. D* 90 (9 2014), p. 094503. DOI: [10.1103/PhysRevD.90.094503](https://doi.org/10.1103/PhysRevD.90.094503). URL: <https://link.aps.org/doi/10.1103/PhysRevD.90.094503>.
- [17] Debasish Banerjee, Jajati K. Nayak, and Raju Venugopalan. “Two Introductory Lectures on High-Energy QCD and Heavy-Ion Collisions”. In: *The Physics of the Quark-Gluon Plasma: Introductory Lectures*. Ed. by Sourav Sarkar, Helmut Satz, and Bikash Sinha. Berlin, Heidelberg: Springer Berlin Heidelberg, 2010, pp. 105–137. ISBN: 978-3-642-02286-9. DOI: [10.1007/978-3-642-02286-9_3](https://doi.org/10.1007/978-3-642-02286-9_3). URL: https://doi.org/10.1007/978-3-642-02286-9_3.
- [18] Stachel, Reygers. *Lectures on QGP*. URL: http://www.physi.uni-heidelberg.de/~reygers/lectures/2011/qgp/qgp_lecture_ss2011.html.
- [19] Edmond Iancu. “QCD in heavy ion collisions”. In: *Proceedings, 2011 European School of High-Energy Physics (ESHEP 2011): Cheile Gradistei, Romania, September 7-20, 2011*. 2014, pp. 197–266. DOI: [10.5170/CERN-2014-003.197](https://doi.org/10.5170/CERN-2014-003.197). arXiv: [1205.0579](https://arxiv.org/abs/1205.0579) [hep-ph]. URL: <https://inspirehep.net/record/1113441/files/arXiv:1205.0579.pdf>.
- [20] Michael Kliemant et al. “Global Properties of Nucleus–Nucleus Collisions”. In: *The Physics of the Quark-Gluon Plasma: Introductory Lectures*. Ed. by Sourav Sarkar, Helmut Satz, and Bikash Sinha. Berlin, Heidelberg: Springer Berlin Heidelberg, 2010, pp. 23–103. ISBN: 978-3-642-02286-9. DOI: [10.1007/978-3-642-02286-9_2](https://doi.org/10.1007/978-3-642-02286-9_2). URL: https://doi.org/10.1007/978-3-642-02286-9_2.
- [21] Michael L. Miller et al. “Glauber modeling in high energy nuclear collisions”. In: *Ann. Rev. Nucl. Part. Sci.* 57 (2007), pp. 205–243. DOI: [10.1146/annurev.nucl.57.090506.123020](https://doi.org/10.1146/annurev.nucl.57.090506.123020). arXiv: [nuc1-ex/0701025](https://arxiv.org/abs/nuc1-ex/0701025) [nucl-ex].
- [22] Tetsufumi Hirano, Naomi van der Kolk, and Ante Bilandzic. “Hydrodynamics and Flow”. In: *The Physics of the Quark-Gluon Plasma: Introductory Lectures*. Ed. by Sourav Sarkar, Helmut Satz, and Bikash Sinha. Berlin, Heidelberg: Springer Berlin Heidelberg, 2010, pp. 139–178. ISBN: 978-3-642-02286-9. DOI: [10.1007/978-3-642-02286-9_4](https://doi.org/10.1007/978-3-642-02286-9_4). URL: https://doi.org/10.1007/978-3-642-02286-9_4.
- [23] Arthur M. Poskanzer and S. A. Voloshin. “Methods for analyzing anisotropic flow in relativistic nuclear collisions”. In: *Phys. Rev.* (1998), pp. 1671–1678. DOI: [10.1103/PhysRevC.58.1671](https://doi.org/10.1103/PhysRevC.58.1671). arXiv: [nuc1-ex/9805001](https://arxiv.org/abs/nuc1-ex/9805001) [nucl-ex].
- [24] K. Aamodt et al. “Higher harmonic anisotropic flow measurements of charged particles in Pb-Pb collisions at $\sqrt{s_{NN}}=2.76$ TeV”. In: *Phys. Rev. Lett.* 107 (2011). ALICE, p. 032301. DOI: [10.1103/PhysRevLett.107.032301](https://doi.org/10.1103/PhysRevLett.107.032301). arXiv: [1105.3865](https://arxiv.org/abs/1105.3865) [nucl-ex].

- [25] Jaroslav Adam et al. “Anisotropic flow of charged particles in Pb-Pb collisions at $\sqrt{s_{\text{NN}}} = 5.02$ TeV”. In: *Phys. Rev. Lett.* 116.13 (2016). ALICE, p. 132302. DOI: [10.1103/PhysRevLett.116.132302](https://doi.org/10.1103/PhysRevLett.116.132302). arXiv: [1602.01119](https://arxiv.org/abs/1602.01119) [nucl-ex].
- [26] Scott McDonald et al. “Hydrodynamic predictions for Pb+Pb collisions at 5.02 TeV”. In: *Phys. Rev.* C95.6 (2017), p. 064913. DOI: [10.1103/PhysRevC.95.064913](https://doi.org/10.1103/PhysRevC.95.064913). arXiv: [1609.02958](https://arxiv.org/abs/1609.02958) [hep-ph].
- [27] Peter Braun-Munzinger, Krzysztof Redlich, and Johanna Stachel. “Particle production in heavy ion collisions”. In: (2003). DOI: [10.1142/9789812795533_0008](https://doi.org/10.1142/9789812795533_0008). arXiv: [nuc1-th/0304013](https://arxiv.org/abs/nuc1-th/0304013) [nucl-th].
- [28] J Stachel et al. “Confronting LHC data with the statistical hadronization model”. In: *Journal of Physics: Conference Series* 509.1 (2014), p. 012019. URL: <http://stacks.iop.org/1742-6596/509/i=1/a=012019>.
- [29] A. Andronic et al. “Heavy-flavour and quarkonium production in the LHC era: from protonproton to heavy-ion collisions”. In: *Eur. Phys. J.* C76.3 (2016), p. 107. DOI: [10.1140/epjc/s10052-015-3819-5](https://doi.org/10.1140/epjc/s10052-015-3819-5). arXiv: [1506.03981](https://arxiv.org/abs/1506.03981) [nucl-ex].
- [30] Hendrik van Hees, Vincenzo Greco, and Ralf Rapp. “Heavy-quark probes of the quark-gluon plasma and interpretation of recent data taken at the BNL Relativistic Heavy Ion Collider”. In: *Phys. Rev. C* 73 (3 2006), p. 034913. DOI: [10.1103/PhysRevC.73.034913](https://doi.org/10.1103/PhysRevC.73.034913). URL: <https://link.aps.org/doi/10.1103/PhysRevC.73.034913>.
- [31] Francesco Prino and Ralf Rapp. “Open Heavy Flavor in QCD Matter and in Nuclear Collisions”. In: *J. Phys.* G43.9 (2016), p. 093002. DOI: [10.1088/0954-3899/43/9/093002](https://doi.org/10.1088/0954-3899/43/9/093002). arXiv: [1603.00529](https://arxiv.org/abs/1603.00529) [nucl-ex].
- [32] G. Aarts et al. “Heavy-flavor production and medium properties in high-energy nuclear collisions - What next?” In: *Eur. Phys. J.* A53.5 (2017), p. 93. DOI: [10.1140/epja/i2017-12282-9](https://doi.org/10.1140/epja/i2017-12282-9). arXiv: [1612.08032](https://arxiv.org/abs/1612.08032) [nucl-th].
- [33] Yuri L. Dokshitzer and D. E. Kharzeev. “Heavy quark colorimetry of QCD matter”. In: *Phys. Lett.* B519 (2001), pp. 199–206. DOI: [10.1016/S0370-2693\(01\)01130-3](https://doi.org/10.1016/S0370-2693(01)01130-3). arXiv: [hep-ph/0106202](https://arxiv.org/abs/hep-ph/0106202) [hep-ph].
- [34] A. Francis et al. “Nonperturbative estimate of the heavy quark momentum diffusion coefficient”. In: *Phys. Rev.* D92.11 (2015), p. 116003. DOI: [10.1103/PhysRevD.92.116003](https://doi.org/10.1103/PhysRevD.92.116003). arXiv: [1508.04543](https://arxiv.org/abs/1508.04543) [hep-lat].
- [35] Shreyasi Acharya et al. “Measurement of D-meson production at mid-rapidity in pp collisions at $\sqrt{s} = 7$ TeV”. In: *Eur. Phys. J.* C77.8 (2017). ALICE, p. 550. DOI: [10.1140/epjc/s10052-017-5090-4](https://doi.org/10.1140/epjc/s10052-017-5090-4). arXiv: [1702.00766](https://arxiv.org/abs/1702.00766) [hep-ex].
- [36] D^0 meson nuclear modification factor in PbPb collisions at $\sqrt{s_{\text{NN}}} = 5.02$ TeV. Tech. rep. CMS-PAS-HIN-16-001. CMS Collaboration. Geneva: CERN, 2016. URL: <https://cds.cern.ch/record/2157844>.
- [37] Matteo Cacciari, Mario Greco, and Paolo Nason. “The P(T) spectrum in heavy flavor hadroproduction”. In: *JHEP* 05 (1998), p. 007. DOI: [10.1088/1126-6708/1998/05/007](https://doi.org/10.1088/1126-6708/1998/05/007). arXiv: [hep-ph/9803400](https://arxiv.org/abs/hep-ph/9803400) [hep-ph].

- [38] K. J. Eskola, H. Paukkunen, and C. A. Salgado. “EPS09: A New Generation of NLO and LO Nuclear Parton Distribution Functions”. In: *JHEP* 04 (2009), p. 065. DOI: [10.1088/1126-6708/2009/04/065](https://doi.org/10.1088/1126-6708/2009/04/065). arXiv: [0902.4154](https://arxiv.org/abs/0902.4154) [hep-ph].
- [39] C. Peterson et al. “Scaling violations in inclusive e^+e^- annihilation spectra”. In: *Phys. Rev. D* 27 (1 1983), pp. 105–111. DOI: [10.1103/PhysRevD.27.105](https://doi.org/10.1103/PhysRevD.27.105). URL: <https://link.aps.org/doi/10.1103/PhysRevD.27.105>.
- [40] Min He, Rainer J. Fries, and Ralf Rapp. “ D_s ”. In: *Phys. Rev. Lett.* 110 (11 2013), p. 112301. DOI: [10.1103/PhysRevLett.110.112301](https://doi.org/10.1103/PhysRevLett.110.112301). URL: <https://link.aps.org/doi/10.1103/PhysRevLett.110.112301>.
- [41] Magdalena Djordjevic and Marko Djordjevic. “LHC jet suppression of light and heavy flavor observables”. In: *Phys. Lett.* B734 (2014), pp. 286–289. DOI: [10.1016/j.physletb.2014.05.053](https://doi.org/10.1016/j.physletb.2014.05.053). arXiv: [1307.4098](https://arxiv.org/abs/1307.4098) [hep-ph].
- [42] Jan Uphoff et al. “Open Heavy Flavor in Pb+Pb Collisions at $\sqrt{s} = 2.76$ TeV within a Transport Model”. In: *Phys. Lett.* B717 (2012), pp. 430–435. DOI: [10.1016/j.physletb.2012.09.069](https://doi.org/10.1016/j.physletb.2012.09.069). arXiv: [1205.4945](https://arxiv.org/abs/1205.4945) [hep-ph].
- [43] Min He, Rainer J. Fries, and Ralf Rapp. “Heavy Flavor at the Large Hadron Collider in a Strong Coupling Approach”. In: *Phys. Lett.* B735 (2014), pp. 445–450. DOI: [10.1016/j.physletb.2014.05.050](https://doi.org/10.1016/j.physletb.2014.05.050). arXiv: [1401.3817](https://arxiv.org/abs/1401.3817) [nucl-th].
- [44] Gian Michele Innocenti. “Open heavy flavour at RHIC and LHC, 7th International Conference on Strangeness in Quark Matter”. URL: <https://indico.cern.ch/event/576735/contributions/2566907/attachments/1491275/2318158/TalkSQM.pdf>.
- [45] Serguei Chatrchyan et al. “Suppression of non-prompt J/ψ , prompt J/ψ , and $Y(1S)$ in PbPb collisions at $\sqrt{s_{NN}} = 2.76$ TeV”. In: *JHEP* 05 (2012). CMS, p. 063. DOI: [10.1007/JHEP05\(2012\)063](https://doi.org/10.1007/JHEP05(2012)063). arXiv: [1201.5069](https://arxiv.org/abs/1201.5069) [nucl-ex].
- [46] Jaroslav Adam et al. “Centrality dependence of high- p_T D meson suppression in Pb-Pb collisions at $\sqrt{s_{NN}} = 2.76$ TeV”. In: *JHEP* 11 (2015). ALICE, p. 205. DOI: [10.1007/JHEP11\(2015\)205](https://doi.org/10.1007/JHEP11(2015)205), [10.1007/JHEP06\(2017\)032](https://doi.org/10.1007/JHEP06(2017)032). arXiv: [1506.06604](https://arxiv.org/abs/1506.06604) [nucl-ex].
- [47] Jaroslav Adam et al. “Measurement of electrons from beauty-hadron decays in p-Pb collisions at $\sqrt{s_{NN}} = 5.02$ TeV and Pb-Pb collisions at $\sqrt{s_{NN}} = 2.76$ TeV”. In: *JHEP* 07 (2017). ALICE, p. 052. DOI: [10.1007/JHEP07\(2017\)052](https://doi.org/10.1007/JHEP07(2017)052). arXiv: [1609.03898](https://arxiv.org/abs/1609.03898) [nucl-ex].
- [48] Jaroslav Adam et al. “Measurement of the production of high- p_T electrons from heavy-flavour hadron decays in Pb-Pb collisions at $\sqrt{s_{NN}} = 2.76$ TeV”. In: *Phys. Lett.* B771 (2017). ALICE, pp. 467–481. DOI: [10.1016/j.physletb.2017.05.060](https://doi.org/10.1016/j.physletb.2017.05.060). arXiv: [1609.07104](https://arxiv.org/abs/1609.07104) [nucl-ex].
- [49] Jaroslav Adam et al. “Inclusive, prompt and non-prompt J/ψ production at mid-rapidity in Pb-Pb collisions at $\sqrt{s_{NN}} = 2.76$ TeV”. In: *JHEP* 07 (2015). ALICE, p. 051. DOI: [10.1007/JHEP07\(2015\)051](https://doi.org/10.1007/JHEP07(2015)051). arXiv: [1504.07151](https://arxiv.org/abs/1504.07151) [nucl-ex].

- [50] Vardan Khachatryan et al. “Charged-particle nuclear modification factors in PbPb and pPb collisions at $\sqrt{s_{NN}} = 5.02$ TeV”. In: *JHEP* 04 (2017). CMS, p. 039. DOI: [10.1007/JHEP04\(2017\)039](https://doi.org/10.1007/JHEP04(2017)039). arXiv: [1611.01664](https://arxiv.org/abs/1611.01664) [nucl-ex].
- [51] Albert M Sirunyan et al. “Measurement of the B^\pm Meson Nuclear Modification Factor in Pb-Pb Collisions at $\sqrt{s_{NN}} = 5.02$ TeV”. In: *Phys. Rev. Lett.* 119.15 (2017). CMS, p. 152301. DOI: [10.1103/PhysRevLett.119.152301](https://doi.org/10.1103/PhysRevLett.119.152301). arXiv: [1705.04727](https://arxiv.org/abs/1705.04727) [hep-ex].
- [52] Vardan Khachatryan et al. “Suppression and azimuthal anisotropy of prompt and nonprompt J/ψ production in PbPb collisions at $\sqrt{s_{NN}} = 2.76$ TeV”. In: *Eur. Phys. J. C* 77.4 (2017). CMS, p. 252. DOI: [10.1140/epjc/s10052-017-4781-1](https://doi.org/10.1140/epjc/s10052-017-4781-1). arXiv: [1610.00613](https://arxiv.org/abs/1610.00613) [nucl-ex].
- [53] Albert M Sirunyan et al. “Nuclear modification factor of D^0 mesons in PbPb collisions at $\sqrt{s_{NN}} = 5.02$ TeV”. In: (2017). arXiv: [1708.04962](https://arxiv.org/abs/1708.04962) [nucl-ex].
- [54] Shreyasi Acharya et al. “D-meson azimuthal anisotropy in mid-central Pb-Pb collisions at $\sqrt{s_{NN}} = 5.02$ TeV”. In: (2017). ALICE. arXiv: [1707.01005](https://arxiv.org/abs/1707.01005) [nucl-ex].
- [55] D^0 meson v_n harmonics in PbPb collisions at 5.02 TeV. Tech. rep. CMS-PAS-HIN-16-007. CMS Collaboration. Geneva: CERN, 2016. URL: <https://cds.cern.ch/record/2216569>.
- [56] Shreyasi Acharya et al. “ J/ψ elliptic flow in Pb-Pb collisions at $\sqrt{s_{NN}} = 5.02$ TeV”. In: (2017). ALICE. arXiv: [1709.05260](https://arxiv.org/abs/1709.05260) [nucl-ex].
- [57] Michael Winn, p.h.d. thesis. “Inclusive J/ψ production at mid-rapidity in p-Pb collisions at $\sqrt{s} = 5.02$ TeV”. URL: https://www.physi.uni-heidelberg.de/Publications/pPb_jpsitoe_master_doctorthesis.pdf.
- [58] Betty Bezverkhny Abelev et al. “Performance of the ALICE experiment at the CERN LHC”. ALICE Collaboration. In: *International Journal of Modern Physics A* 29.24 (2014), p. 1430044. DOI: [10.1142/S0217751X14300440](https://doi.org/10.1142/S0217751X14300440).
- [59] K. Aamodt et al. “The ALICE experiment at the CERN LHC”. ALICE Collaboration. In: *JINST* 3 (2008), S08002. DOI: [10.1088/1748-0221/3/08/S08002](https://doi.org/10.1088/1748-0221/3/08/S08002).
- [60] F. Carminati et al. “ALICE: physics performance report, volume I”. ALICE Collaboration. In: *Journal of Physics G: Nuclear and Particle Physics* 30.11 (2004), p. 1517.
- [61] Ionut Arsene, Raul Tonatiuh Bustamante, Pascal Dillenseger, Markus K. Koehler, Dennis Weiser. “Nuclear modification factor of inclusive J/Ψ production at mid-rapidity in PbPb collisions at $\sqrt{s} = 5.02$ TeV”. 2017. URL: <https://aliceinfo.cern.ch/Notes/node/592>.

- [62] Raul Tonatiuh Jimenez Bustamante. “ALICE measurement of the J/ψ nuclear modification factor at mid-rapidity in PbPb collisions at $\sqrt{s_{NN}}=5.02$ TeV”. In: *Nuclear Physics A* 967.Supplement C (2017). The 26th International Conference on Ultra-relativistic Nucleus-Nucleus Collisions: Quark Matter 2017, pp. 576–579. ISSN: 0375-9474. DOI: <https://doi.org/10.1016/j.nuclphysa.2017.06.026>. URL: <http://www.sciencedirect.com/science/article/pii/S0375947417302877>.
- [63] B. Audurier, B. Paul, M. Tarhini. “Multi-differential studies of the J/ψ production in PbPb collisions at $\sqrt{s} = 5.02$ TeV”. 2017. URL: <https://aliceinfo.cern.ch/Notes/node/581>.
- [64] Roger Barlow. “Systematic errors: Facts and fictions”. In: *Advanced Statistical Techniques in Particle Physics. Proceedings, Conference, Durham, UK, March 18-22, 2002*. 2002, pp. 134–144. arXiv: [hep-ex/0207026](https://arxiv.org/abs/hep-ex/0207026) [[hep-ex](#)].
- [65] F. Bossu et al. “Phenomenological interpolation of the inclusive J/ψ cross section to proton-proton collisions at 2.76 TeV and 5.5 TeV”. In: (2011). arXiv: [1103.2394](https://arxiv.org/abs/1103.2394) [[nucl-ex](#)].
- [66] Christian Boeser, Simon Fink, Steffen Roecker Institut fuer Experimentelle Kernphysik, KIT. “Introduction to Boosted Decision Trees”. URL: <https://indico.scc.kit.edu/indico/event/48/session/4/contribution/35/material/slides/0.pdf>.
- [67] A. Hoecker et al. “TMVA - Toolkit for Multivariate Data Analysis”. In: *ArXiv Physics e-prints* (Mar. 2007). eprint: [physics/0703039](https://arxiv.org/abs/physics/0703039).
- [68] D. Acosta et al. “Measurement of the J/ψ meson and b -hadron production cross sections in $p\bar{p}$ collisions at $\sqrt{s} = 1960$ GeV”. In: *Phys. Rev. D* 71 (2005). CDF, p. 032001. DOI: [10.1103/PhysRevD.71.032001](https://doi.org/10.1103/PhysRevD.71.032001). arXiv: [hep-ex/0412071](https://arxiv.org/abs/hep-ex/0412071) [[hep-ex](#)].
- [69] S. Gorbunov and I. Kisel. “Reconstruction of decayed particles based on the Kalman filter”. CBM. In: (2007). CBM-SOFT-note-2007-003.
- [70] Wouter Verkerke, NIKHEF. “RooFit”. URL: <http://cicpi.ustc.edu.cn/indico/getFile.py/access?sessionId=2&resId=1&materialId=0&confId=678>.
- [71] W. Verkerke and D. Kirkby. “The RooFit toolkit for data modeling”. In: *ArXiv Physics e-prints* (June 2003). eprint: [physics/0306116](https://arxiv.org/abs/physics/0306116).
- [72] Wikipedia, the free encyclopedia. *Comparison of a histogram and a kernel density estimate*. [28 September 2010]. 2010. URL: https://commons.wikimedia.org/wiki/File:Comparison_of_1D_histogram_and_KDE.png.
- [73] F. Pedregosa et al. “Scikit-learn: Machine Learning in Python”. In: *Journal of Machine Learning Research* 12 (2011), pp. 2825–2830.
- [74] Kyle S. Cranmer. “Kernel estimation in high-energy physics”. In: *Comput. Phys. Commun.* 136 (2001), pp. 198–207. DOI: [10.1016/S0010-4655\(00\)00243-5](https://doi.org/10.1016/S0010-4655(00)00243-5). arXiv: [hep-ex/0011057](https://arxiv.org/abs/hep-ex/0011057) [[hep-ex](#)].

- [75] Georges Aad et al. “Measurement of the differential cross-sections of inclusive, prompt and non-prompt J/ψ production in proton-proton collisions at $\sqrt{s} = 7$ TeV”. In: *Nucl. Phys.* B850 (2011). ATLAS, pp. 387–444. DOI: [10.1016/j.nuclphysb.2011.05.015](https://doi.org/10.1016/j.nuclphysb.2011.05.015). arXiv: [1104.3038](https://arxiv.org/abs/1104.3038) [hep-ex].
- [76] Vardan Khachatryan et al. “Prompt and non-prompt J/ψ production in pp collisions at $\sqrt{s} = 7$ TeV”. In: *Eur. Phys. J.* C71 (2011). CMS, p. 1575. DOI: [10.1140/epjc/s10052-011-1575-8](https://doi.org/10.1140/epjc/s10052-011-1575-8). arXiv: [1011.4193](https://arxiv.org/abs/1011.4193) [hep-ex].
- [77] Fiorella Fionda. “Measurement of fraction of J/ψ from beauty hadrons in PbPb collisions at $\sqrt{s_{NN}} = 2.76$ TeV”. 2017. URL: <https://aliceinfo.cern.ch/Notes/node/311>.
- [78] Giuseppe Trombetta. “Measurement of the non-prompt J/ψ fraction at central rapidity in p–Pb collisions at $\sqrt{s} = 5.02$ TeV”. 2017. URL: <https://aliceinfo.cern.ch/Notes/node/585>.
- [79] Betty Abelev et al. “Measurement of prompt J/ψ and beauty hadron production cross sections at mid-rapidity in pp collisions at $\sqrt{s} = 7$ TeV”. In: *JHEP* 11 (2012). ALICE, p. 065. DOI: [10.1007/JHEP11\(2012\)065](https://doi.org/10.1007/JHEP11(2012)065). arXiv: [1205.5880](https://arxiv.org/abs/1205.5880) [hep-ex].
- [80] Betty Bezverkhny Abelev et al. “Production of charged pions, kaons and protons at large transverse momenta in pp and PbPb collisions at $\sqrt{s_{NN}} = 2.76$ TeV”. In: *Phys. Lett.* B736 (2014). ALICE, pp. 196–207. DOI: [10.1016/j.physletb.2014.07.011](https://doi.org/10.1016/j.physletb.2014.07.011). arXiv: [1401.1250](https://arxiv.org/abs/1401.1250) [nucl-ex].
- [81] Sebastian Hornung, bachelor thesis. “New criteria for distinguishing hadrons containing beauty from hadrons with charm in proton-proton collisions with $\sqrt{s} = 7$ TeV at ALICE”. URL: https://www.physi.uni-heidelberg.de/Publications/SHornung_bachelor.pdf.
- [82] Georges Aad et al. “Search for massive, long-lived particles using multitrack displaced vertices or displaced lepton pairs in pp collisions at $\sqrt{s} = 8$ TeV with the ATLAS detector”. In: *Phys. Rev.* D92.7 (2015). ATLAS, p. 072004. DOI: [10.1103/PhysRevD.92.072004](https://doi.org/10.1103/PhysRevD.92.072004). arXiv: [1504.05162](https://arxiv.org/abs/1504.05162) [hep-ex].

Erklärung:

Ich versichere, dass ich diese Arbeit selbstständig verfasst habe und keine anderen als die angegebenen Quellen und Hilfsmittel benutzt habe.

Heidelberg, den (Datum)